2024

Analysis of Ultra-wideband Voltage Pulse Propagation on Dispersive Absorptive Transmission Lines

Katherine Aho
University of Vermont

Analysis of Ultra-wideband Voltage Pulse Propagation on Dispersive Absorptive Transmission Lines

A Dissertation Presented

by

Katherine Aho

to

The Faculty of the Graduate College

of

The University of Vermont

In Partial Fulfillment of the Requirements
for the Degree of Doctor of Philosophy
Specializing in Electrical Engineering

August, 2024

Defense Date: July 11, 2024
Dissertation Examination Committee:

Kurt E. Oughstun, Ph.D., Advisor
Donna M. Rizzo, Ph.D., Chairperson
Tian Xia, Ph.D.
Sam Chevalier, Ph.D.
Holger Hoock, DPhil, Dean of the Graduate College

Abstract

Electromagnetic transient waves are pulsed events that occur when there is an abrupt change in the typical steady-state conditions on a transmission line. Digital pulses on integrated circuits and a lightning strike on overhead power lines are some examples of transient voltage pulses. Although transients occur within a very short time duration, they can propagate over long distances; much farther than a slowly-varying envelope signal can propagate. Lingering effects of transients can be damaging to electrical equipment if they are not properly mitigated.

Despite the negative effects of transients, certain designed transient pulses may be used to an advantage in remote sensing applications, such as that found in Time Domain Reflectometry (TDR). TDR analysis is a method that makes use of pulse propagation on transmission lines in order to identify and locate any abrupt changes to the line characteristics. Applications include identifying moisture content in soil and detecting damage on printed circuit boards. Accurate identification of damage and other material changes is complicated by transmission line losses, such as attenuation, dispersion, and frequency-dependent circuit parameters. Dispersion and frequency-dependent losses result in different frequency components of the wave propagating at different velocities, which introduces a spreading effect on the wave as it propagates down the line. The effective dielectric constant of the transmission line and surrounding media influences the losses that create the distortion. Material properties and line geometry determine the value of the effective dielectric constant, and they may be identified through a detailed analysis of the reflected pulse.

A detailed study of the behavior of pulse propagation on dispersive attenuative transmission lines is presented in this dissertation. Models of three different types of transmission lines are extended in order to compare the effects of material properties and line geometry on transmission properties. These include the coaxial cable, single microstrip, and coupled microstrip models. A numerical model is developed in order to calculate the effects of voltage propagation on a particular transmission line that contains impedance changes. A trapezoidal envelope pulse is considered because of its typical use in digital applications. TDR techniques are then performed with the trapezoidal envelope pulse in order to identify the locations of a change in medium properties. Historically, the group velocity of the pulse is used to perform TDR analysis, but it does not accurately account for the distortion of the pulse in a dispersive and attenuative media. The energy centrovelocity is used here as an alternative to the group velocity. The accuracy of the use of energy centrovelocity in TDR is analyzed.

Acknowledgements

As I sit down to write these acknowledgements, I find myself nearly at a lost for words since I never expected to reach this point. The process of performing this research and writing this dissertation has been arduous and burdensome. The trials and tribulations faced since beginning of my doctoral journey in 2014 may have slowed progress, but it did not stop it. This work is a culmination of several years of academic, professional, and personal growth. None of which would have been possible without the support and encouragement of those in my life.

First and foremost, I am extremely grateful for the patience and perseverance of my advisor, Dr. Kurt Oughstun. So much of this work is attributed to his experience and invaluable feedback. I would not have completed this dissertation without his endless dedication. I would also like to thank Dr. Charles Thompson and Dr. Kavitha Chandra for exposing me to research as an undergraduate student, encouraging me to apply for doctoral programs, and ultimately changing the entire trajectory of my career.

To all of my friends and family who heard my struggles and complaints about this process over the years. I am particularly thankful to my parents and their weekly phone calls. And to my fellow cohort member turned best friend Dr. Kelsey Linnell, who gave me snacks at all of the right times.

Most importantly, I extend my gratitude to my husband, Brian for keeping up with the house chores while I locked myself in my office nearly every evening to focus on this research. To my pup, Brewski, for his never-ending cuddles and moral support. And finally, I would like to thank J.R.R Tolkien for his writings that provided the much needed inspiration to carry on. I plan to enjoy all seven Hobbit meals in celebration.

Table of Contents

List of Figures

List of Tables

Chapter 1

Background

1.1 Introduction

Transmission of telecommunication signals and electrical power is vital to the function and operation of modern society. The power grid, the internet, computers, and cell phones are all common examples of systems that depend on signal performance and effective power transmission. Some more uncommon, but still widely used examples are found in underground power lines and time domain reflectometry (TDR) probes. Transmission line grids have grown significantly since the mid-1800s, beginning with the developments of the telegraph and electrical power grid [1]. Over time, telecommunications equipment has developed beyond hard-wired telephone lines and moved towards cellular and wireless devices. It is clear that our world would not be as connected without the used of the transmission of signals and power, either on a wire or wirelessly.

Electrical signals travel along transmission lines to deliver information or power from a source to a receiver. The transmitters and receivers for cellular and wireless

devices are comprised of integrated circuits (ICs). Transmission lines are built into integrated circuits as a means of delivering voltage and current throughout the circuit [2]. The ability to communicate and deliver power efficiently is highly dependent on the integrity of the signal being transmitted. Maintaining signal integrity within a transmission network or an integrated circuit is crucial for safety and quality of the signals. If a signal is corrupted and does not maintain integrity, it could lead to faulty data transmission or, even worse, an equipment failure that may lead to a blackout. Poor signal integrity is often a result of damaged or degraded transmission lines be caused by, for example, an event such as switching, a lightning strike on a power line, or a disruption of power in an IC [2, 3]. In some instances, an electromagnetic transient wave can be produced at the location or event that caused the degradation of the signal integrity.

Electromagnetic transient waves are ultra-wideband (UWB) pulses that occur when there is an abrupt change in the typical steady-state conditions on a transmission line [4], caused for example, by switching, a lightning strike on a power line, or a disruption of power in an integrated circuit [2, 3]. The American National Standards Institute (ANSI) defines a transient as, "a single electromagnetic event, or single-shot voltage, current, electric, or magnetic field impulse or pulse, such as generated by lighting, electromagnetic pulse (EMP), or switching action... pertaining to or designating a phenomenon or a quantity that varies between two consecutive steady states during a time interval that is short when compared to the time-scale of interest" [5]. At a fixed position along a transmission line, a transient wave may only last for a short period of time. However, it may only propagate long distances in a dispersive absorptive medium due to its unique properties. Accurate modeling and simulation of

transient behavior is then necessary in order to identify either potential line damage so that protection schemes can be appropriately designed for the system [6] or any changes in the medium of the material surrounding the transmission line.

Time domain reflectometry (TDR) is one of the methods used in identifying either line damage or media changes. This is accomplished by remotely determining the location of an impedance mismatch along the transmission line, if possible. Because this is an inverse problem, the uniqueness of the solution is not always guaranteed [7–11]. The TDR method relies upon the intentional propagation of a specifically designed transient pulse along a transmission line whose reflection can then be used to determine the location of any changes in the material properties of or surrounding the cable. This is accomplished by calculating the time difference between the start time of the initial transient and the return time of the reflected transient.

Transient signals can occur on any type of transmission line geometry, including, but not limited to, coaxial cables, single microstrips, coupled microstrips, and TE-planar mode waveguides. Typical Time Domain Reflectometry (TDR) applications make use of either a coaxial cable or a simple strip line comprised of two parallel wires separated by a fixed distance. The geometry and length of a coaxial transmission line allows for an initial pulse with low frequency. The choice of this type of pulse and line is best for underground power line applications or the identification of soil composition. Microstrip lines, either single or coupled, work best with a high frequency initial pulse. They are most commonly used in microwave circuits and the TDR response can serve to identify any potential causes of signal distortion. In this regard, line geometry and material dispersion are important parameters to consider in any analysis of these systems, as they may impact the propagation effects of a

given transient signal. The influence of the transmission line geometry and material dispersion together with its potential application to TDR analysis are central topics that are discussed in this dissertation.

The work presented in this dissertation departs from the typical literature through the complexity of the transmission line models considered here in material, attenuation and dispersion, as well as frequency-dependent circuit parameters, which are often either simplified or completely ignored. This dissertation aims to include all line characteristics in order to improve the accuracy of the ensuing model. These results are then applied to the inverse problem of detecting material changes along the transmission line through its estimated dispersive properties.

1.2 Motivation

Electromagnetic transients are rapidly changing waveforms in time that may propagate over long distances in space with material attenuation. A transient event may result in a voltage signal where its frequency spectrum changes rapidly, resulting in a transient wave that may propagate near the speed of light in vacuum along the transmission line [12]. As a consequence, lingering effects of theses transients can be damaging to electrical equipment and electronic devices if they are not properly mitigated. That is, transients can produce extremely high voltage and current values that can easily damage the electrical equipment and device [6].

Depending on the type of transmission line, the causes and impact of transient wave damage can differ. For example, in the power grid, transients are often described as singular fault events that could potentially lead to widespread blackouts.

This is particularly concerning as power gird infrastructure in the United States is aging and large scale renewable generation is being incorporated into the grid. On microwave or IC circuits, such as a computer motherboard, transients are typically caused by either signal switching or power surges. High frequency transient effects can lead to electromagnetic interference within ICs, resulting in poor signal integrity and potential safety concerns to the user of the device.

In the case of the power grid, transients have been a concern with the increase of renewable energy power generation. Because wind turbines and solar panels have a much smaller capacity for power generation than traditional fossil fuels, more renewable generators must be connected and distributed throughout the grid in order to meet consumer demand. As a consequence, more conductors are required to connect the variety of renewables to the rest of the grid. These conductors are designed to have a lower impedance in order to reduce the power loss [13]. However, this low impedance serves to enable the propagation of high frequency signals, such as transients, throughout the transmission network. It is not uncommon for solar panels, for example, to be connected directly to the location of power consumption. In that situation, a home could now be directly susceptible to damage produced by a transient [13]. Because of this, it is essential to monitor the behavior of any such transient fields as they propagate through the grid and more accurately identify the locations of any potential failures or media changes that could increase the impact of the damage caused by a transient field.

Another example where transients can be problematic are within integrated circuits (ICs), such as those found in electronic devices including filters, couplers, [14] and communications devices [15], which are typically designed with a microstrip as the

main type of transmission line [2]. Because switching can often result in a transient field on such a microstrip line, it is essential to properly understand the dispersive properties of the microstrip transmission line in order to design the circuit in such at way that a given transient is minimally damaging to the device. Microstrip lines are unique in comparison to other types of transmission line systems in that there are two different dielectric materials surrounding the line, typically the substrate and air [16]. Signal interaction with the substrate and air layers results in dispersive frequency effects, which can distort both voltage and current pulses that are propagating along the transmission line [2].

In any one of these applications discussed, physical changes along a transmission line, such as a change in the substrate material or damage within the line itself, can amplify the undesirable effects that can be caused by a transient field. An accurate determination of the location of the line failure allows for its repair or, in an extreme case, a redesign of the transmission line itself in order to prevent the transient behavior from even occurring. This dissertation aims to investigate the inverse problem in order to identify problematic areas that may occur on a given transmission line.

Inverse problems have long been studied in physics as a means of using the results of observations to make conclusions regarding the parameters or characteristics of the system of interest. Several applications of inverse problems have been reported, such as determining the moisture content in soil [8, 10], measuring the length of an acoustic horn, [17,18], identifying damages within a wiring network [11,19], as well as determining the location of any physical cracks on a printed circuit board (PCB) [20]. The inverse problem of interest here is that of time-domain reflectometry (TDR). TDR is a measurement technique with a wide range of applications from measuring

moisture content in soil [8, 21] to detecting faults in complex wiring networks such as that found in aircraft and nuclear power plants [11, 22] to tracking chemical spills and oil leaks [23]. Acoustic pulses have also been utilized in a similar manner in order to determine the area and length of an acoustic waveguide, as in, for example, the human vocal tract [17, 18].

Time domain reflectometry (TDR) is based on principles that are similar to those found in RADAR [11] where one detects and identified an unknown object from its reflected pulsed electromagnetic field [21]. In TDR, an electromagnetic pulse that is sent down a uniform transmission line will reflect off any type of impedance discontinuity that occurs on the line [11], such as that from a fault in the line itself or a change in the material properties surrounding the line. The location of the impedance discontinuity may then be determined from either the time delay or phase shift between the incident and reflected signals [11, 22]. The use of transient pulses is ideal for this purpose because the method relies on the response due to real time measurements, rather than the steady-state response. Since transient pulses can occur in a very short time duration, the real time measurements allow for increased accuracy when identifying the location of the interface. If there are multiple discrete changes along the line, each at a different distance from the input, then multiple pulse reflections will occur resulting in a complicated return signal that must then be properly unraveled in order to determine the location of each discontinuity.

1.3 Objective

The objective of this dissertation is two-fold. The forward problem is considered first in which the propagation of a transient signal on a general transmission line model is considered. The model analyzed here considers three different types of transmission lines: a coaxial cable, a single microstrip, and a coupled microstrip line. In particular, the microstrip lines will be comprised of a Debye-type dielectric substrate. This choice of the Debye-type substrate allows for a frequency dependent dispersion relation that results in a unique spreading effect of the voltage pulse. Pulse dispersion is a naturally occurring phenomenon that can distort the shape of the pulse, making it difficult to accurately measure the exact temporal width of the propagated pulse and consequently its propagation velocity.

The propagation of a transient pulse is modeled here based upon traditional transmission line models. Beginning with a single transmission line and a single interconnect, the transmission and reflection of an ultra-wideband pulse is computed. Each transmission line model includes all appropriate attenuative, dispersive, and frequency-dependent material properties, with special attention given to the inherent frequency dispersion of the dielectric permittivity and its effect on the propagation factor for the specific transmission line. This analysis is then extended to a transmission line model that includes multiple layered material changes. In that situation, pulse dispersion is further exaggerated through each successive transmission and reflection at a given interface between each material layer. The ultimate goal is to be able to determine the location along the transmission line where the surrounding material properties have changed in a discrete manner.

The sceonf part of this research involves the inverse problem of determining the dispersive properties of the surrounding material itself, and hence the identification of the material, is considered by using time-domain reflectometry (TDR) techniques. Observation of the changes in structure of the return signal from a pulsed input signal are used to determine any change in the dielectric properties of the material surrounding the transmission line. Changes in the transmission line characteristics can also be caused by damages along the transmission line. Following traditional TDR techniques, the time difference between the initial pulse and the reflected pulse may be used to identify the location of either damages along the line, or a significant change of the line material or its surrounding media. These changes are modeled here for the case of a layered dielectric when there are several discrete changes in the surrounding media. As an example, material changes could represent the changes in moisture content in the adjacent soil layers. In the situation where there are more than one discrete dielectric interfaces, multiple pulse reflections will be returned to the point of pulse insertion. Each successive reflected pulse will then have to be unraveled in time in order to identify the location of each media change. Notice that dispersion of the pulse makes it difficult to measure either the start of the rise or the end of the fall of a given pulse, which then will reduce the accuracy of the TDR method. The research presented in this dissertation aims to utilize a detection method, such as that based upon the pulse centroid that does not rely upon either the rise or fall time of the input pulse envelope.

The research focus of this dissertation departs from that featured in the published literature by incorporating all loss characteristics into the transmission line model including dispersive attenuation, pulse velocity dispersion, and frequency-dependent

circuit parameters. Additionally, the shape of the initial pulse in this model will differ from that used in the literature by utilizing a single-cycle sine wave of fixed frequency with a trapezoidal envelope. Much of the previous work considers the behavior of either a square pulse with a carrier entirely within the rise and and fall times or a Gaussian pulse envelope without an underlying carrier wave. The trapezoidal envelope pulse considered here is much more representative of the types of pulses that are typically used in digital circuitry. The centroid of the input and return voltage pulses is determined in order to accurately measure the time at which the return pulse arrives back to the source. From there, TDR is applied to determine the location of the change in media that results in pulse reflection and transmission.

1.4 Review of the Published Literature

An historical review of transient voltage propagation problems is now considered. Some landmark studies, in the areas of transients due to lightning on electric power lines [6, 24, 25], microstrip transmission line models [2, 14, 26], and soil measurements using TDR [7, 8, 10, 27] are discussed in detail throughout this section. An emphasis is placed upon inverse problems associated with both transmission lines and TDR applications.

1.4.1 Computational Methods

The computation of transient voltage pulse propagation on transmission lines dates back to the late 1920s. Graphical methods were used in early attemptsn in order to visualize wave propagation along a transmission line [24, 25]. A common motivator

at the time was to model the effect of lighting strikes on a given transmission line. Cathode-ray oscillographs, (more commonly known as oscilloscopes) were invented in the 1920s [28, 29] and were designed to empirically measure wave propagation on the transmission line. Bewley's development of Lattice Diagrams in 1931 allowed for a simple and algorithmic approach to pulse propagation over an interface [25]. Lattice Diagrams were introduced and used to capture the reflection and transmission coefficients of the pulse as it propagated through consecutive interfaces along the transmission line. In these early attempts, linear attenuation and dispersion are represented visually and can then be computed analytically through the summation of the attenuation and dispersion coefficients, assuming that they are known.

Another widely-used graphical method are so-called Bergeron diagrams, which were a visual representation of the classic differential equation solution method called the method of characteristics. Bergeron diagrams were initially developed in 1928 to plot the behavior of a water hammer in hydraulic systems [30,31]. In 1967, Branin [24] first applied Bergeron Diagrams and the method of characteristics to the analysis of overhead power transmission lines as a means of graphically determining the relationship between the voltage and current along the line. The method of characteristics is a classical mathematical technique that maps a partial differential equation (PDE) to one or more ordinary differential equation (ODE) in order to obtain an exact solution [32]. It can be applied to the lumped element transmission line equations in order to determine the voltage and current at each end of the transmission line [24]. The ordinary differential equation describing the relationship between the voltage and the reactive elements can then easily be solved numerically with the trapezoidal rule [31] or a similar method of integration. At the time of it's conception, the method of

characteristics appeared to only be viable for ideal lossless lines [24] as the resulting ODEs could not be integrated directly. One advantage of a Bergeron diagram is that the reflection and transmission coefficients need not be known. However, it can only provide an accurate solution for lossless and distortionless lines [6]. Recent work [33,34] still makes use of the method of characteristics successfully included the loss terms as well as the frequency-dependence of the circuit parameters.

With the advent of analog computers in the late 1930s, numerical simulations of transient wave propagation in electrical power networks were made possible [6,35,36]. One such analog computer specifically designed for this purpose was known as a Transient Network Analyzer, an analog instrument which provided insight into the expected shape of the transient waveform at various points within a power network. In such a case, an initial pulse is applied and the general shape of the succeeding transient pulses are observed as a traveling wave combined with effects of the transient responses of the circuit parameters comprising the transmission line. Similar to some graphical methods, limitations in the computational resources of Transient Network Analyzers prevented the influence of loss and distortion on the pulse from being determined. Although Transient Network Analyzers could model transients in real-time and were numerically stable, they were extremely expensive to operate and could only simulate a small number of power system busses. Despite these limitations, Transient Network Analyzers continued to be used on occasion into the early 1980s [37].

By the 1970s, Transient Network Analyzers were almost entirely replaced by digital computers [4, 38]. Not only were digital computers more economically feasible, they were also superior in speed, flexibility, and could be used to solve other types of physics and mathematics problems beyond transient analysis. Digital comput-

ers allowed for the development of discretized numerical simulations to the transient problem. In particular, the Fast Fourier Transform (FFT) algorithm [39] provided an efficiency in computation by reducing the number of calculations required to perform Fourier analysis [40] on the voltage or current waveform.

In 1974, Dommel and Meyer [6] first identified the potential use of the FFT to calculate the response of a transmission line system. The FFT was noted to be particularly effective for use in transmission lines modeled with distributed circuit parameters, where Bergeron's diagrams were not considered an effective solution method. The FFT algorithm allowed one to efficiently transform the second-order partial differential equations that arise from the time-varying voltage and current relationship into first-order ordinary differential equations in the frequency domain. In doing so, the analysis of the transmission line is simplified significantly and the required computation time is dramatically reduced. Because of this, the FFT is still used widely today and continues to improve in efficiency as processing capabilities of computers improve. As a recent example, in 2004, Grivet-Talocia et. al. [33] used the method of characteristics to analyze a lossy transmission line that included the frequency-dependence of the circuit parameters. The FFT was employed there in order to develop a frequency-domain solution so as to capture the physics of the frequency-dependence.

1.4.2 Transmission Line Models

The most common method of modeling transmission lines is through the use of a distributed circuit model. The electric and magnetic properties of the transmission line are described through the resistance, inductance, conductance, and capacitance

per unit length along the transmission line. Circuit models conventionally relate the voltage, current, and impedance of the transmission line and can easily be solved in the frequency domain. The use of circuit models for transmission line analysis was initially developed by Lord Kelvin in 1855 and later completed by Oliver Heaviside in 1885 [41].

Perhaps one of the oldest and simplest types of transmission line models with a corresponding circuit model is the coaxial cable, which was patented by Oliver Heaviside in 1880 with the stated intention of eliminating coupling between two parallel wires [42]. Heaviside placed an insulating material in between the two wires, which then allowed the wires to act independently of each other. Coaxial cables continue to be one of the most commonly used transmission lines to this day due to their ease of construction and ability to carry high frequency signals over very long distances with minimal loss [41]. Specific details on coaxial cable models are provided in Chapter 3.

As the technological needs of our society advanced, so did the types of transmission lines being used. Telephone transmission lines typically include twisted pair and star quad cables. Aluminium conductor steel reinforced cables were designed to support high electrical power transmission over long distances. Since the invention of the transistor [43], printed circuit boards (PCBs) soon became the primary technology for computing and telecommunication purposes. Microstrip and coupled microstrip transmission lines then became the primary types of transmission lines that one may find on a PCB [2,14]. The microstrip line differs significantly from the aforementioned cables because it is considered an open-air structure [2], whereas cables, such as those used in telephone and power systems, are fully enclosed [41]. The combination of the air and substrate of the PCB results in dispersive effects on the voltage signal of

a microstrip transmission line. This dispersive behavior is of fundamental research interest.

Analytic solutions have been developed for arrays of multiple conductors [3] and coupled transmission lines [14], as well as single microstrip lines [16] throughout the 1970s. Garg and Bahl's [14] coupled microstrip line analysis introduced the effects of dispersion influenced by coupling between the lines. Getsinger's [16] single microstrip transmission line model subsequently provided a closed form solution for the dispersion relation.

In 1986, Veghte and Balanis's [2] seminal paper sought to accurately characterize the effects of distortion on transient pulses propagating along lossless microstrip lines in integrated circuits (ICs). Transients often arise in ICs during high-frequency switching operations. The microstrip waveguide is bounded above in air and below a dielectric substrate, and consequently it is highly dispersive. Because of this, the wave can never be in a pure TEM-mode and field theory methods can be difficult to employ. A closed-form solution was developed for the voltage pulse influenced by dispersion on a lossless strip line using the Fourier Transform approach. Special attention was also paid to the dielectric constant as it varied with frequency and its relationship to the propagation factor of the pulse. The results indicated how dispersion influenced and distorted the shape of the input waveform. Dispersion was observed in the transient pulses that were considered, and it was found that the dispersive effects were most prominent in the square DC pulse due to its high spectral content.

1.4.3 Applications of Time Domain Reflectometry

Time Domain Reflectometry (TDR) has been used in such diverse fields as electrical power, electronics, and geotechnical sensing. Some specific applications within these fields include the phenomena of partial discharges, and the determination of moisture content measurements in soil. The following subsections focus on these aforementioned applications and the role that TDR plays in each case.

Partial Discharges

One common problem in the area of power systems is the identification of partial discharges (PDs) in underground cables. PDs are a characteristic of the early stages of deterioration of the dielectric insulator in power cables [44]. The outer dielectric material has been found to degrade over time when it has been exposed to such environmental factors, as moisture, mechanical vibration, or pressure changes. These environmental factors can eventually lead to the failure of the cable [45]. In turn, this degradation of the cable can cause a discharge of fast, high-frequency current pulses or transients [46]. One method of finding the location of PDs is through TDR measurements, which has been investigated with varying degrees of success [44–47]. A TDR measurement is very accurate at identifying the location of of a given PD in certain cases, but fails in a other scenarios, particularly when the PD occurs at a large distance away along the transmission line from the TDR detector. If the transmission line is long and the PD pulse needs to propagate a long distance to reach the TDR detector, there is a high likelihood that the transmission line attenuation effects will

significantly reduce the amplitude of the PD pulse, making it difficult to be identified by the TDR detector. In 2020, Papadopoulus et al [48] included the influence of the dispersion, dielectric constant, and frequency-dependence of the soil surrounding the underground cable. Their work was able to improve the accuracy of modeling the transient response of a cable.

Other recent work has aimed to improve the limitations of TDR to identify PDs on transmission lines. In 2013, Wild et al [49] placed two TDR detectors on the transmission line, with one TDR detector placed at each end of the line. This was done in an effort to reduce the effects of attenuation when the PD pulse propagates down the line and reflects back to the detector. With two TDR detectors, waiting for the response due to the reflected PD pulse need not be necessary. As a result, any attenuation or dispersion caused by the PD pulse reflection is reduced. However, placing a TDR detector at both ends, particularly at the end of the line, is not always possible.

In 2016, Rodgrigo Mor et al [50] sought to improve the accuracy of PD pulse localization in the situation where the PD starts at the end opposite to the TDR detector. A resonance circuit at the end of the transmission line that matches the resonant impedance of the line is introduced. In doing so, the reflected pulse is not fully reflected and is partially absorbed by the resonance circuit at the resonant frequency. The advantage of this method is that the TDR measurement is not dependent upon any attenuation effects of the transmission line or the amplitude of the PD pulse.

Moisture content in soil

A further use of a transient field considers the identification of materials, such as the moisture content in soil. TDR is helpful in agricultural and environmental applications such as irrigation, soil cover for landfills [23], or detecting water condensation on buildings that could lead to premature deterioration of the building material [51].

Since the late 1970s, TDR has been used in hydrogeological applications in order to determine the water content and electrical conductivity in soil. It has been demonstrated that small changes in moisture content can easily be captured by TDR [23]. Davis and Annan [7] were among the first to use electromagnetic waves in this capacity, determining that an empirical relationship exists between the complex dielectric permittivity of the soil and its moisture content, this being due to the relationship between the speed of propagation of the electromagnetic wave and the dielectric permittivity through which it is propagating. Davis and Annan's [7] work instigated several landmark studies of TDR soil moisture measurements throughout the 1980s. Topp et al [8,52], Heimovaara [10], Dalton et al [53], and Zegelin [54] carried out TDR experiments in various types of soils in order to more accurately develop empirical equations for the dielectric permittivity, the electric conductivity of the soil, and the water content of the soil.

More recent estimations of soil water content using TDR focused on the simulation and modeling of the TDR probe and the associated pulse propagation. Skierucha [55] sought to reduce the sources of error when measuring volumetric water content of the soil by taking into account bulk soil density when calibrating the TDR device. In 2006, Greco [27] developed a more accurate model of TDR pulse propagation and treated the determination of soil moisture content from a voltage pulse as an

inverse problem. The direct problem was evaluated by modeling a three-wire TDR probe as a waveguide, solving the Telegrapher's equations along the waveguide using boundary conditions that are determined from the hydraulic properties of the soil. The variability in solutions that can arise from the inverse problem were reduced by applying a set of physical constraints to the solution.

In order to improve the accuracy of TDR modeling in soil, it was found that the polar mechanics and dielectric relaxation of the soil needed be considered [56]. Neveux and Chambrel [57] treated the soil as a Debye-type dielectric. In 2016, Loewer, et al [58] took into account the dielectric relaxation of the soil by treating the soil as both a Debye and a Cole-Cole type with a constant DC conductivity.

1.5 Proposed Research

Much of the published research on the subject of transmission line analysis that exists in the open literature includes the detection and identification of the substrate material or material surrounding the line, however several key elements still remain to be investigated. The first considers the use of the measured pulse velocity of the return signal to determine the composition of the substrate material, as well as the location of any interface where the material properties change. Prior research relies upon the use of the group velocity of the initial and reflected pulses. However, the peak amplitude point of the pulse that moves with group velocity is not easily measured or numerically determined. In this research, the pulse centrovelocity is investigated, as it has physical meaning and is directly measurable.

Transmitted pulse properties that are used to determine the substrate material

composition, such as water content in soil, are also investigated. The measured pulse centrovelocity is essential in this determination. The pulse amplitude attenuation coefficient and the pulse energy attenuation coefficient are of interest here, as well as the relationship between them as the input pulse width decreases.

The propagated pulse characteristics change fundamentally, as the input pulse width decreases into the ultrashort/ultra-wideband limit, resulting in a transient waveform that is more indicative of the transmission line properties and its substrate material, rather than initial shape of the input pulse. Historically, this transient field is often referred to as a precursor. Its asymptotic form and propagation velocity depends upon the temporal dispersion properties and reveals much about the transmission line and substrate material properties. Such behavior will also be presented in this dissertation.

Chapter 2

Dispersive Attenuative Transmission Line Analysis

2.1 Introduction

An overview of voltage pulse propagation on a dispersive attenuative transmission line is essential for understanding the transmission and reflection properties of a transmission line in the presence of a layered medium. Such a study can be used to design new transmission line structures or to observe the behavior of a pulse as it propagates through a series of discontinuous media changes. Some examples of external media changes include changes in motherboard PCB layering, weather events around a power line, changes in soil moisture content, or a line that is partially underground and partially above ground. External media changes result in changing impedance values along the line. Because this impedance directly impacts the propagation behavior of the signal on the transmission line, the observed signal changes along a transmission line are dependent on the surrounding media properties as well as upon

the circuit parameters of the line. Modeling the propagation of a voltage pulse signal on a transmission line with a frequency-dependent complex impedance may provide insight into the resultant signal integrity, a property that is essential to maintaining the system performance or the measurement accuracy of a transmission line.

It is of particular interest to study dispersion effects on transmission line signal flow. Most transmission line studies have been simplified by neglecting loss. However, these inherent losses can have a significant impact on the propagation of a voltage and its related current pulse. Dispersive effects can result in distortion of the shape of the pulse over long distances. In the power grid, for example, dispersion may be a contributing factor in the instigation of a blackout. In the case of soil moisture measurements using Time Domain Reflectometry (TDR), the dispersive properties of the surrounding soil may be used to more accurately measure that moisture content.

In this chapter, the elements of transmission line analysis are reviewed. Because of its importance to this research as well as its applicability in practice, a trapezoidal envelope pulse is considered in detail along with its frequency spectrum. The low frequency behavior of the pulse is of particular importance here when the carrier frequency is considered as low. The pulse is first described analytically in both the time and frequency domains, which is then compared against a numerical Fast Fourier Transform (FFT) calculation of the pulse spectrum. With that in hand and its assured numerical accuracy, the propagation of a single-cycle trapezoidal envelope voltage pulse along a lossy dispersive transmission line may be compared with the propagation characteristics of an identical initial voltage pulse along a lossless transmission line. This is done in order to study the effects of dispersion along a more realistic model of a transmission line. These computations are performed using MATLAB software

with adequate time and frequency sampling.

2.2 Distributed Circuit Model

It is of central interest to observe the propagation behavior of an input voltage pulse along the various transmission line models that are discussed throughout this dissertation, including the coaxial cable, the single and coupled microstrip lines, and in particular, microstrip lines with a Debye-type dielectric substrate. Special emphasis is placed upon the effects of dispersion and the observed pulse evolution.

In order to calculate the propagation of a voltage pulse along a given transmission line, the traditional distributed circuit model [41, 59, 60] is used. The distributed circuit method of analysis provides an advantage over electromagnetic field methods in that it makes use of typical circuit analysis quantities of voltage, current, and impedance that would be familiar with practitioners in this field. In addition, using such a method allows for ease of handling each of the frequency-dependent circuit terms. The equivalent circuit model of a transmission line presented in Figure 2.1 is used to develop the distributed circuit analysis. Here R is the total series resistance of the line per unit length, L is the total series inductance of the line per unit length, C is the shunt capacitance of the line per unit length, and G is the shunt conductance of the line per unit length. The coaxial cable, single microstrip, and coupled microstrip, all make use of the same circuit model presented in Figure 2.1, but expressions and values for each circuit parameter differ based upon the particular transmission line type. With application of Kirchhoff's Circuit Laws to the circuit model depicted in Figure 2.1, the coupled Telegrapher's equations that describe the propagation of the

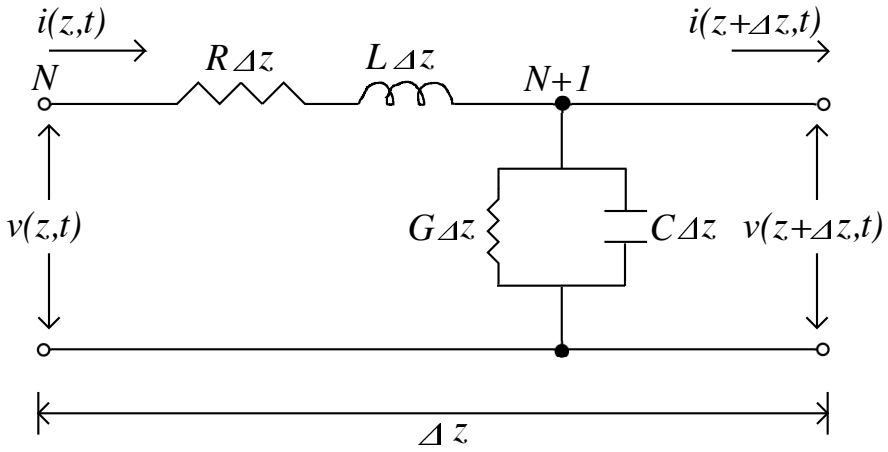

Figure 2.1: Distributed Circuit Model of an incremental section of a Transmission Line. Here, R is the total series resistance of the line per unit length, L is the total series inductance of the line per unit length, C is the shunt capacitance of the line per unit length, and G is the shunt conductance of the line per unit length.

voltage and current pulses are readily obtained.

2.2.1 The Uniform Transmission Line Equations

Kirchhoff's Voltage Law (KVL) is applied to the incremential section of a transmission line depicted in Figure 2.1 to yield the following expression relating the instantaneous voltage along an infinitesimal segment of transmission line,

$$v(z,t) - R\Delta z i(z,t) - L\Delta z \frac{\partial i(z,t)}{\partial t} - v(z+\Delta z,t) = 0, \tag{2.1}$$

while application of Kirchhoff's Current Law (KCL) for the instantaneous current along the same segment of transmission line gives

$$i(z,t) - G\Delta z v(z+\Delta z,t) - C\Delta z \frac{\partial v(z+\Delta z,t)}{\partial t} - i(z+\Delta z,t) = 0, \tag{2.2}$$

where $v(z,t)$ and $i(z,t)$ are the instantaneous voltages and current at the space-time point (z,t) respectively, where Δz is the incremental length of the line segment considered. With the definition of the derivative in mind, this pair of equations may be rewritten in the form

$$-\left(\frac{v(z+\Delta z,t)-v(z,t)}{\Delta z}\right) = Ri(z,t) + L\frac{\partial i(z,t)}{\partial t}, \tag{2.3a}$$

$$-\left(\frac{i(z+\Delta z)-i(z,t)}{\Delta z}\right) = Gv(z+\Delta z,t) + C\frac{\partial v(z+\Delta z,t)}{\partial t}. \tag{2.3b}$$

Upon taking the limit as Δz approaches zero these two equations become

$$-\frac{\partial v(z,t)}{\partial z} = Ri(z,t) + L\frac{\partial i(z,t)}{\partial t} \tag{2.4a}$$

$$-\frac{\partial i(z,t)}{\partial z} = Gv(z,t) + C\frac{\partial v(z,t)}{\partial t}. \tag{2.4b}$$

The pair of relations appearing in Equations (2.4a) and (2.4b) form a set of coupled partial differential equations known as either the Telegrapher's Equations or the Transmission Line Equations. The solutions of these equations provide expressions for the voltage and current behavior along the transmission line.

In order to begin the analysis, Equations (2.4a) and (2.4b) are first expressed in the frequency domain through the introduction of a complex valued phasor representation of both the voltage and current functions, where

$$v(z,t) = \Re\{\tilde{V}e^{j\omega t}\}, \tag{2.5a}$$

$$i(z,t) = \Re\{\tilde{I}e^{j\omega t}\}. \tag{2.5b}$$

Upon transforming the Telegrapher's equations into the phasor domain by substituting the phasor representations given in Equations (2.5a) and (2.5b) gives

$$-\frac{d\tilde{V}(z)}{dz} = (R + j\omega L)\tilde{I}(z) \tag{2.6a}$$

$$-\frac{d\tilde{I}(z)}{dz} = (G + j\omega C)\tilde{V}(z). \tag{2.6b}$$

In order to decouple these two equations, each is differentiated with respect to the propagated distance z. The expression in Eq. (2.6b) is then substituted into the resulting $\frac{d\tilde{I}(z)}{dz}$ term in Eq. (2.6a). A similar substitution for the first derivative term $\frac{d\tilde{V}(z)}{dz}$ in Eq. (2.6b) is also performed. This then results in two second-order differential equations for the phasor voltage and current, respectively, that are fully decoupled, given by

$$\frac{d^2\tilde{V}(z)}{dz^2} = (G + j\omega C)(R + j\omega L)\tilde{V}(z), \tag{2.7a}$$

$$\frac{d^2\tilde{I}(z)}{dz^2} = (G + j\omega C)(R + j\omega L)\tilde{I}(z). \tag{2.7b}$$

Nevertheless, the phasor voltage and the current along the line are related through the line impedance.

With the definition that $\gamma^2(\omega) = (G + j\omega C)(R + j\omega L)$, Eqs. (2.7a) and (2.7b) can be rewritten in the form of the Helmholtz equations as

$$\frac{d^2\tilde{V}(z)}{dz^2} - \gamma^2(\omega)\tilde{V}(z) = 0, \tag{2.8a}$$

$$\frac{d^2\tilde{I}(z)}{dz^2} - \gamma^2(\omega)\tilde{I}(z) = 0. \tag{2.8b}$$

Here, $\gamma(\omega)$ is the complex propagation factor of the wave and and may be expressed

in terms of its real and imaginary parts as

$$\gamma(\omega) = \alpha(\omega) + j\beta(\omega), \tag{2.9}$$

with

$$\alpha(\omega) = \Re\{\gamma(\omega)\}, \tag{2.10a}$$

$$\beta(\omega) = \Im\{\gamma(\omega)\}. \tag{2.10b}$$

As expressed in these equations, the real part of $\gamma(\omega)$ defines the attenuation or loss factor of the wave. The effect of this attenuation factor $\alpha(\omega)$ on the wave results in an exponential decay of the wave amplitude with increasing propagation distance z. The imaginary part $\beta(\omega)$ of $\gamma(\omega)$ is the phasal propagation factor. It defines the phase change of the wave as it propagates along the transmission line. Notice that The effects of material dispersion are embedded within the expression for the complex propagation factor.

The general solutions to the Helmholtz equations can be described in terms of two parts: (1) a forward traveling wave which propagates in the positive $(+)z$-direction toward the receiving end of the transmission line or an interface along the line and (2) a backward traveling wave which propagates in the negative $(-)z$-direction back toward the input voltage or current source. The voltage and the current, are then given by

$$\tilde{V}(z) = V_0^+ e^{-\gamma(\omega)z} + V_0^- e^{\gamma(\omega)z}, \tag{2.11a}$$

$$\tilde{I}(z) = I_0^+ e^{-\gamma(\omega)z} + I_0^- e^{\gamma(\omega)z}, \tag{2.11b}$$

where V_0^+ and I_0^+ are the amplitudes of the voltage and current, respectively, for

the forward traveling wave that is moving away from the voltage or current source. Similarly, V_0^- and I_0^- are the amplitudes of the voltage and current for the backward traveling wave, propagating back towards the voltage or current source.

Substitution of Eq. (2.11a) into Eq. (2.6a) gives

$$\begin{aligned}\tilde{I}(z) &= \frac{\gamma(\omega)}{R+j\omega L}\left(V_0^+ e^{-\gamma(\omega)z} - V_0^- e^{+\gamma(\omega)z}\right) \\ &= \frac{1}{Z_0(\omega)}\left(V_0^+ e^{-\gamma(\omega)z} - V_0^- e^{+\gamma(\omega)z}\right),\end{aligned}$$

such that $V_0^+/I_0^+ = -V_0^-/I_0^- = Z_0$, where

$$Z_0(\omega) = \frac{R+j\omega L}{\gamma(\omega)} = \sqrt{\frac{R+j\omega L}{G+j\omega C}} \tag{2.12}$$

is the characteristic impedance of the transmission line. With this identification, the general solution of Equations (2.11a) and (2.11b) becomes

$$\tilde{V}(z) = V_0^+ e^{-\gamma(\omega)z} + V_0^- e^{+\gamma(\omega)z}, \tag{2.13a}$$

$$\tilde{I}(z) = \frac{1}{Z_0(\omega)}\left(V_0^+ e^{-\gamma(\omega)z} + V_0^- e^{+\gamma(\omega)z}\right), \tag{2.13b}$$

for the voltage and the current, respectively. For simplification of the resulting analysis, let $z = 0$ represent the sending (source) end of the transmission line, where the initial voltage or current pulse is inserted. Notice the departure from a typical transmission line analysis where $z = 0$ is chosen at the receiving end and the source then becomes located at $z = -z_d$ In this case,

$$\tilde{V}(0) = V_0^+ + V_0^-, \tag{2.14a}$$

$$\tilde{I}(z) = \frac{1}{Z_0(\omega)} \left(V_0^+ + V_0^- \right). \tag{2.14b}$$

With this choice of the $z = 0$ point, any change in the line impedance will be taken to occur at $z = z_{mn}$, where Z_m is the incident line impedance and Z_n is the transmitted line impedance. The relation between V_0^+ and V_0^- is then determined by the reflection coefficient at each coordinate value $z = z_{mn}$ where the line impedance changes.

In order to gain further insight into the propagation of an elementary time-harmonic wave on a transmission line, consider the exponential term $e^{-\gamma(\omega)z}$ in conjunction with its assumed $e^{j\omega t}$ time-dependence (which is not explicitly displayed). Substitution of the decomposition of $\gamma(\omega)$ yields $e^{-\gamma(\omega)z}e^{j\omega t} = e^{-\alpha(\omega)z}e^{j(\omega t - \beta z)}$. The phase velocity of the wave in the forward direction is then given by the derivative the phase term $\omega t - \beta(\omega)$ with respect to time and space, which is constant on a wavefront, so that $v_p = \frac{\omega}{\beta(\omega)}$ m/s in the reverse direction. Upon application of the exact same analysis to the exponential term for the backward propagating piece $e^{\gamma(\omega)z}$ gives a phase velocity that is $v_p = -\frac{\omega}{\beta(\omega)}$ m/s. Notice that the phase velocity is dependent on the frequency-dependence of the propagation factor which contains any material or system dispersion.

2.2.2 Segmented Transmission Line Analysis

Consider now a longitudinally segmented transmission line where each homogeneous section extends from z_j to z_{j+1} with $j = 0, 1, 2, \ldots, N$, with there being $N+1$ sections. The first section ($j = 0$), extends from z_0, the location of the voltage source, to z_1, where the first interface is encountered. Within the jth segment, the line has characteristic resistance R_j, conductance G_j, inductance L_j, and capacitance C_j.

Each section of uniform section of transmission line is characterized by its own intrinsic impedance that is given by $Z_j = V_j^+/I_j^+ = V_j^-/I_j^-$, as required by Ohm's Law. Upon using Equations (2.7a) and (2.7b) and the general solutions to the Helmholtz equation, the characteristic impedance of each line segment is found to be

$$Z_j = \sqrt{\frac{R_j + j\omega L_j}{G_j + j\omega C_j}} \quad \text{for } j = 0, 1, 2, \ldots, N \tag{2.15}$$

Along such a longitudinally segmented transmission line, an interface occurs between each homogeneous segment, as depicted in Figure 2.2, where the characteristic impedance differs on either side of the interface. A transmission and reflection of any incident wave will then occur at that interface along with a phase change. The amount of transmission and reflection in both amplitude and phase at the interface is determined by the transmission and reflection coefficients at that point, which are functions of the impedance values on each side of the interface.

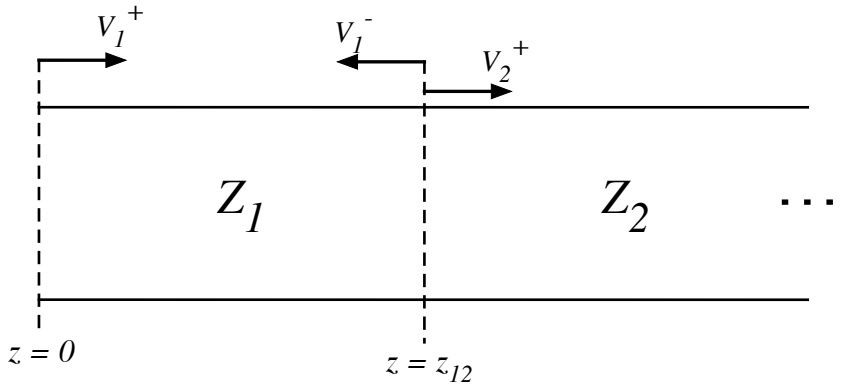

Figure 2.2: Model of a transmission line with an interface at a location $z = z_{12}$, which separates different media described by different characteristic impedance values, Z_1 and Z_2.

(a) A Single Interface

From Equations (2.11a) and (2.11b), the phasor voltage and current along the first segment of the line, where $0 \leq z \leq z_{12}$, are given by

$$\tilde{V}_1(z) = V_1^+(0)e^{-\gamma_1(\omega)z} + V_1^-(z_{12})e^{\gamma_1(\omega)(z-z_{12})}, \tag{2.16a}$$

$$\tilde{I}_1(z) = \frac{1}{Z_1}\left(V_1^+(0)e^{-\gamma_1(\omega)z} + V_1^-(z_{12})e^{\gamma_1(\omega)(z-z_{12})}\right), \tag{2.16b}$$

respectively. Here, $V_1^+(0)$ is the input value of the voltage at the source (the input port), where as $V_1^-(z_{12})$ is the value of the voltage reflected at the interface $z = z_{12}$ and its value incident back on the input port being given by

$$V_1^-(0) = V_1^-(z_{12})e^{-\gamma(\omega)z_{12}}. \tag{2.17}$$

At $z = 0$ the voltage and current are then given respectively by

$$\begin{aligned}\tilde{V}_1(0) &= V_1^+(0) + V_1^-(z_{12})e^{-\gamma_1(\omega)z_{12}} \\ &= V_1^+(0) + V_1^-(0),\end{aligned} \tag{2.18a}$$

$$\tilde{I}_1(0) = \frac{1}{Z_1}\left(V_1^+(0) - V_1^-(z_{12})e^{-\gamma_1(\omega)z_{12}}\right), \tag{2.18b}$$

and at the interface at $z = z_{12}$ separating the first segment of the transmission line (with complex impedance Z_1) from the second segment of the transmission line (with complex impedance Z_2), the voltage and current on the transmission line are given

by

$$\begin{aligned}\tilde{V}_1(z_{12}) &= V_1^+(0)e^{-\gamma_1(\omega)z_{12}} + V_1^-(z_{12}) \\ &= V_1^+(0)e^{-\gamma_1(\omega)z_{12}} + V_1^-(0)e^{\gamma_1(\omega)z_{12}}\end{aligned} \tag{2.19a}$$

$$\tilde{I}_1(z_{12}) = \frac{1}{Z_1}\left(V_1^+(0)e^{-\gamma_1(\omega)z_{12}} + V_1^-(z_{12})\right), \tag{2.19b}$$

respectively. Notice that the second forms of Eqs. (2.18a) and (2.19a) express the backward propagating phasor voltage in terms of its limiting value at the input port, that is

$$V_1^-(0) = \lim_{z\to 0^+}\left(V_1^-(z_{12})e^{\gamma(\omega)(z-z_2)}\right) \tag{2.20}$$

Along the second transmission line segment, $z \geq z_{12}$, the phasor voltage and current are

$$\tilde{V}_2(z) = V_2^+(z_{12})e^{-\gamma_2(\omega)(z-z_{12})} \tag{2.21a}$$

$$\tilde{I}_2(z) = \frac{1}{Z_2}\left(V_2^+(z_{12})e^{-\gamma_2(\omega)(z-z_{12})}\right), \tag{2.21b}$$

respectively, where $V_2^+(z_{12})$ is the forward traveling voltage transmitted across the interface at $z = z_{12}$.

At the interface, $z = z_{12}$, where the characteristic impedance changes discontinuously from Z_1 to Z_2, continuity of the total voltage and current are demonstrated as, $\tilde{V}_1(z_{12}) = \tilde{V}_2(z_{12})$ and $\tilde{I}_1(z_{12}) = \tilde{I}_2(z_{12})$, respectively. Upon substitution from Eqs. (2.19) and (2.21) into these two relations, one obtains

$$V_1^+(0)e^{-\gamma_1(\omega)z_{12}} + V_1^-(z_{12}) = V_2^+(z_{12}), \tag{2.22a}$$

$$\frac{1}{Z_1}\left(V_1^+(0)e^{-\gamma_1(\omega)z_{12}} + V_1^-(z_{12})\right) = \frac{1}{Z_2}V_2^+(z_{12}). \tag{2.22b}$$

Further substitution of Eq. (2.22a) into Eq. (2.22b) gives

$$\frac{1}{Z_1}\left(V_1^+(0)e^{-\gamma_1(\omega)z_{12}} - V_1^-(z_{12})\right) = \frac{1}{Z_2}\left(V_1^+(0)e^{-\gamma_1(\omega)z_{12}} + V_1^-(z_{12})\right),$$

which then reduces to

$$(Z_2 - Z_1)\, V_1^+(0)e^{-\gamma_1(\omega)z_{12}} = (Z_1 + Z_2)\, V_1^-(z_{12}). \tag{2.23}$$

Taking note that

$$V_1^+(z_{12}) = V_1^+(0)e^{-\gamma_1(\omega)z_{12}} \tag{2.24}$$

is the value of the forward propagating voltage incident upon the interface, Eq. (2.23) may also be written as

$$\left(Z_2 - Z_1 V_1^+(z_{12})\right) = (Z_1 + Z_2)\, V_1^-(z_{12}). \tag{2.25}$$

There are two ways in which voltage reflection coefficient may be described, the first using Eq. (2.23), and the second starting with Eq. (2.25).Consider first the second approach in which the voltage reflection coefficient is defined as

$$\Gamma_{12} = \frac{V_1^-(z_{12})}{V_1^+(z_{12})} = \frac{Z_2 - Z_1}{Z_1 + Z_2}. \tag{2.26}$$

With this result, the expression in Eq. (2.18) for the phasor line voltage along the

first segment of the transmission line, $0 \leq z \leq z_{12}$, becomes

$$\tilde{V}_1(z) = V_1^+(0)e^{-\gamma_1(\omega)z} + \Gamma_{12}V_1^+(z_{12})e^{\gamma_1(\omega)(z-z_{12})}. \tag{2.27}$$

Because $V_1^+(z_{12}) = V_1^+(0)e^{-\gamma_1(\omega)z_{12}}$, this expression may be written as

$$\begin{aligned}\tilde{V}_1(z) &= V_1^+(z_{12})\left(e^{\gamma_1(\omega)(z_{12}-z)} + \Gamma_{12}e^{-\gamma_1(\omega)(z-z_{12})}\right) \\ &= V_1^+(0)\left(e^{-\gamma_1(\omega)z} + \Gamma_{12}e^{\gamma_1(\omega)(z-2z_{12})}\right).\end{aligned} \tag{2.28}$$

In a similar manner, the voltage transmission coefficient is defined as

$$\tau_{12} = \frac{V_2^+(z_{12})}{V_1^+(z_{12})}, \tag{2.29}$$

so that, from Eqs. (2.22a) and (2.24).

$$\tau_{12} = 1 + \Gamma_{12} = \frac{2Z_2}{Z_1 + Z_2}, \tag{2.30}$$

which are just the usual expressions [41,59,60] for the voltage reflection and transmission coefficients at a single interface. They are most appropriate to use in addressing the multiple interface problem.

Consider now the first choice for the reflection coefficient in Eq. (2.26), included here for comparison with both the above results as well as that found in the open literature [61]. With Eq. (2.23), a modified voltage reflection coeffieicent is defined as

$$\Gamma'_{12} = \frac{V_1^-(z_{12})}{V_1 + (0)} = \frac{Z_2 - Z_1}{Z_1 + Z_2}e^{-\gamma_1(\omega)z_{12}}, \tag{2.31}$$

in which case,

$$\Gamma_{12}^{'} = \Gamma_{12} e^{-\gamma_1(\omega) z_{12}}. \tag{2.32}$$

With this identification, the expression for the line voltage at $z = z_{12}$ given in Eq. (2.19a) becomes

$$\tilde{V}(z_{12}) = V_1^+(0) e^{-\gamma_1(\omega) z_{12}} + \Gamma_{12}^{'} V_1^+(0). \tag{2.33}$$

Similarly, the modified voltage transmission coefficient is defined as

$$\tau_{12}^{'} = \frac{V_2^+(z_{12})}{V_1^+(0)} = e^{-\gamma_1(\omega) z_{12}} + \Gamma_{12}^{'} \tag{2.34}$$

following substitution from Eq. (2.22a). From this result, it is immediately found that

$$\tau_{12}^{'} e^{-\gamma_1(\omega) z_{12}} - \Gamma_{12}^{'} e^{\gamma_1(\omega) z_{12}} = 1. \tag{2.35}$$

In addition, Eq. (2.34) yields, after substitution from Eq. (2.31), the result

$$\tau_{12}^{'} = \frac{2Z_2}{Z_1 + Z_2} e^{-\gamma_1(\omega) z_{12}} = \tau_{12} e^{-\gamma_1(\omega) z_{12}} \tag{2.36}$$

(b) Two Interfaces

In keeping with Fig. 2.2, let interface 1, separating medium 1 (with impedance Z_1) from medium 2 (with impedance Z_2) be at distance $z = z_{12}$ from the input port at $z = 0$, and let interface 2, separating medium 2 (with impedance Z_2) from medium 3 (with impedance Z_3) be at the distance $z = z_{23}$ from the input port so that it is at the distance $z_2 = z_{23} - z_{12}$ from interface 1, as illustrated in Fig. 2.3.

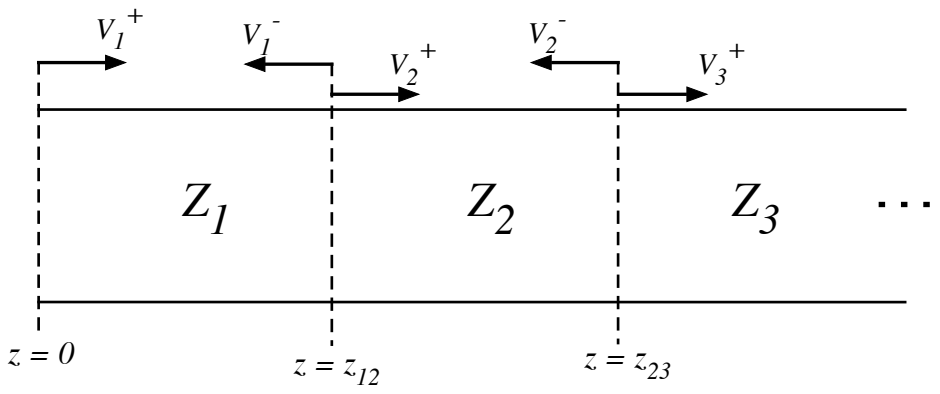

Figure 2.3: Model of a transmission line with an two interfaces location $z = z_{12}$ and $z = z_{23}$, which separates different media described by different characteristic impedance values, Z_1, Z_2, Z_3.

Recall the single interface reflection and transmission coefficients at interface 1 found in Eqs. (2.26) and (2.30)

$$\Gamma_{12} = \frac{Z_2 - Z_1}{Z_1 + Z_2}, \tag{2.37a}$$

$$\tau_{12} = 1 + \Gamma_{12} = \frac{2Z_2}{Z_1 + Z_2}, \tag{2.37b}$$

and subsequently, the single interface reflection and transmission coefficients at interface 2 when the incident field on interface 2 is taken to originate from interface 1 are

$$\Gamma_{23} = \frac{Z_3 - Z_2}{Z_2 + Z_3}, \tag{2.38a}$$

$$\tau_{23} = 1 + \Gamma_{23} = \frac{2Z_3}{Z_2 + Z_3}. \tag{2.38b}$$

Let the voltage traveling in the positive (+) direction incident upon interface 1 be $V_{1i}^{+} = V^{+}(0)e^{\gamma_1(\omega)z_1}$, where $V^{+}(0)$ is the input voltage at the source port. A portion

of this incident voltage V_{1i}^{+} is reflected back into medium 1

$$V_{1r}^{-} = \Gamma_{12} V_{1i}^{+}, \tag{2.39a}$$

and the remaining portion is transmitted into medium 2, where

$$V_{2t1}^{+} = \tau_{12} V_{1i}^{+}. \tag{2.39b}$$

This transmitted field V_{2t}^{+} propagates to the second interface, yielding the incident voltage

$$V_{2i1}^{+} = V_{2t1}^{+} e^{\gamma_2(\omega) z_2} = \tau_{12} e^{\gamma_2(\omega) z_2} V_{1i}^{+}, \tag{2.39c}$$

which produces the reflected voltage

$$V_{2r1}^{-} = \Gamma_{23} V_{2i1}^{+} = \tau_{12} \Gamma_{23} e^{\gamma_2(\omega) z_2} V_{1i}^{+} \tag{2.39d}$$

in medium 2, and the transmitted voltage

$$V_{3t1} = \tau_{23} V_{2i1}^{+} = \tau_{12} \tau_{23} e^{\gamma_2(\omega) z_2} V_{1i}^{+} \tag{2.39e}$$

entering into medium 3. The reflected voltage incident back on interface 1 is given by

$$\begin{aligned} V_{2r1i}^{-} &= V_{2r1}^{-} e^{\gamma_2(\omega) z_2} \\ &= \tau_{12} \Gamma_{23} e^{2\gamma_2(\omega) z_2} V_{1i}^{+} \end{aligned} \tag{2.39f}$$

which, in turn, gives rise to the reverse travelling transmitted voltage in medium 1, given by

$$V^-_{2r1t} = \tau_{21} V^-_{2r1i} = \tau_{12}\tau_{21}\Gamma_{23} e^{2\gamma_2 z_2} V^+_{1i}, \tag{2.39g}$$

where

$$\tau_{21} = \frac{2Z_1}{Z_1 + Z_2},$$

which does not equal τ_{12} unless $Z_1 = Z_2$ (in which case interface 1 vanishes). The reverse propagating voltage V^-_{2r1i} in medium 2 also produces a reflected voltage

$$V^+_{2r1r} = \Gamma_{21} V^-_{2r1i} = -\tau_{12}\Gamma_{12}\Gamma_{23} e^{2\gamma_2 z_2} V^+_{1i} \tag{2.39h}$$

because

$$\Gamma_{21} = \frac{Z_1 - Z_2}{Z_1 + Z_2} = -\Gamma_{12}.$$

Notice that, as a consequence of this relation, $\tau_{21} = 2 - \tau_{12}$, that is, $(\tau_{12} + \tau_{21})/2 = 1$. The forward propagating voltage V^+_{2r1r} reflected at interface 1 in medium 2 results in the voltage

$$V^+_{2r1ri} = V^+_{2r1r} e^{\gamma_2 z_2} = -\tau_{12}\Gamma_{12}\Gamma_{23} e^{3\gamma_2 z_2} V^+_{1i} \tag{2.39i}$$

incident upon interface 2. This incident forward propagating voltage in medium 2

produces a reflected voltage

$$V_{2r1rr}^{-} = \Gamma_{23} V_{2r1ri}^{+} = -\tau_{12}\Gamma_{12}\Gamma_{23}^{2} e^{3\gamma_2 z_2} V_{1i}^{+} \tag{2.39j}$$

propagating the in the reverse direction in medium 2, and a transmitted voltage

$$V_{3t2}^{+} = \tau_{23} V_{2r1ri}^{+} = -\tau_{12}\tau_{23}\Gamma_{12}\Gamma_{23} e^{3\gamma_2 z_2} V_{1i}^{+} \tag{2.39k}$$

propagating in the positive direction in medium 3. The reflected voltage back on interface 1 in medium 2 is given by

$$V_{2r1rri}^{-} = V_{2r1rr}^{-} e^{\gamma_2 z_2} = -\tau_{12}\Gamma_{12}\Gamma_{23}^{2} e^{4\gamma_2 z_2} V_{1i}^{+} \tag{2.39l}$$

which then results in a transmitted voltage across interface 1 and into medium 1, given by

$$V_{2r1rrt}^{-} = \tau_{21} V_{2r1rri}^{-} = -\tau_{12}\tau_{21}\Gamma_{12}\Gamma_{23}^{2} e^{4\gamma_2 z_2} V_{1i}^{+}, \tag{2.39m}$$

and so on.

The total reflected voltage at the first interface in medium 1 travelling in the negative direction back towards the input port is then given by the summation.

$$\begin{aligned} V_r^{-} &= V_{1r}^{-} + V_{2r1t}^{-} + V_{2r1rrt}^{1} + \dots \\ &= \left[\Gamma_{12} + \tau_{12}\tau_{21}\Gamma_{23} e^{2\gamma_2 z_2}\left(1 - \Gamma_{12}\Gamma_{23} e^{2\gamma_2 z_2} + \Gamma_{12}^{2}\Gamma_{23}^{2} e^{4\gamma_2 z_2} - \dots\right)\right] V_{1i}^{+} \\ &= \left(\Gamma_{12} + \frac{\tau_{12}\tau_{21} e^{2\gamma_2 z_2}}{1 + \Gamma_{12}\Gamma_{23} e^{2\gamma_2 z_2}}\right) V_{1i}^{+}, \end{aligned} \tag{2.40}$$

and the total transmitted voltage at the second interface in medium 3 travelling in

the positive direction towards an infinitely distant end of the transmission line given by the summation

$$\begin{aligned} V_t^+ &= V_{3t1}^+ + V_{3t2}^+ + \dots \\ &= \tau_{12}\tau_{23}e^{\gamma_2 z_2}\left(1 - \Gamma_{12}\Gamma_{23}e^{2\gamma_2 z_2} + \dots\right) V_{1i}^+ \\ &= \frac{\tau_{12}\tau_{23}e^{\gamma_2 z_2}}{1 + \Gamma_{12}\Gamma_{23}e^{2\gamma_2\gamma_3}} V_{1i}^+. \end{aligned} \tag{2.41}$$

Therefore, the overall or net reflection coefficient though the entire two interface system is

$$\Gamma = \frac{V_r^-}{V_{1i}^+} = \Gamma_{12} + \frac{\tau_{12}\tau_{21}\Gamma_{23}e^{2\gamma_2 z_2}}{1 + \Gamma_{12}\Gamma_{23}e^{2\gamma_2 z_2}}, \tag{2.42}$$

and the overall transmission coefficient through the two interface system is

$$\tau = \frac{V_t^+}{V_{1i}^+} = \frac{\tau_{12}\tau_{23}e^{\gamma_2 z_2}}{1 + \Gamma_{12}\Gamma_{23}e^{2\gamma_2 z_2}}. \tag{2.43}$$

Notice that

$$\Gamma + \tau = \Gamma_{12} + \tau_{12}e^{\gamma_2 z_2}\frac{\tau_{21}\tau_{23}e^{\gamma_2 z_2} + \tau_{23}}{1 + \Gamma_{12}\Gamma_{23}e^{2\gamma_2 z_2}}. \tag{2.44}$$

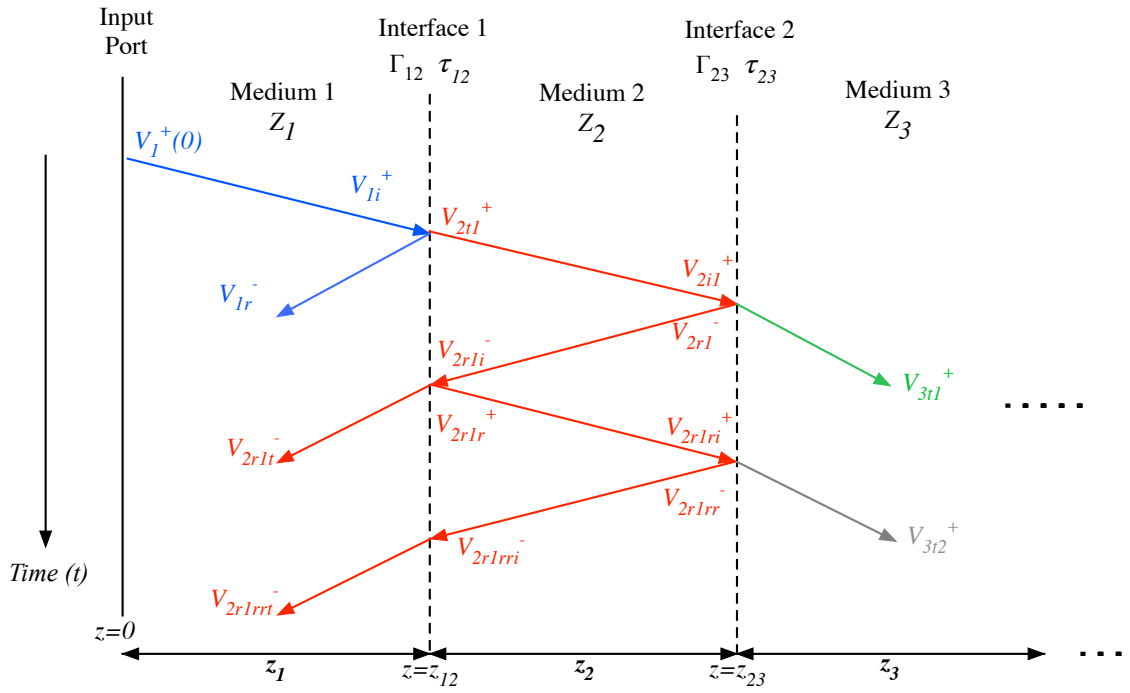

Figure 2.4: Lattice diagram of the voltage reflection and transmission for two interfaces.

2.3 Voltage Pulse Velocity

Several methods exist to calculate and measure the velocity of an electromagnetic pulse propagating along a transmission line. The most commonly used velocity representations are the phase velocity and the group velocity. However, it has been found that there are many shortcomings regarding the accuracy of the such velocity calculations in dispersive and attenuative media [62–64]. In such a case, the wave becomes distorted as it propagates through the medium, making it difficult to measure or even define a physically meaningful velocity using traditional time of flight methods. Although the phase and group velocity may be physically meaningful in non-dispersive

media, they can yield vastly different results when material dispersion and absorption are present [62, 63]. Therefore, it is important to define a measurable pulse velocity that remains meaningful when dispersion and absorption are present [64–66].

A different description of the pulse velocity was introduced by Smith in 1970 [62]. This velocity, known as the centrovelocity, makes use of the centroid of the electromagnetic pulse energy. The centrovelocity overcomes many of the previous shortcomings as it can be measured using time of flight methods, is not dependent on the frequency response of the detector, and the pulse itself is not required to be quasimonochromatic.

2.3.1 The Phase Velocity

The phase velocity is often described as the propagation speed and direction of the carrier wavefront. Brillouin defines the phase velocity as "the phase difference between the vibrations observed at two different points in a free plane wave" [67].

For the time-harmonic voltage pulse, the space-time behavior is given by

$$V(z,t) = V_0^+ e^{-\gamma z} e^{j\omega t} = V_0^+ e^{-\alpha z} e^{j(\omega t - \beta z)}, \tag{2.45a}$$

$$I(z,t) = I_0^+ e^{-\gamma z} e^{j\omega t} = \frac{V_0^+}{Z_0} e^{-\alpha z} e^{j(\omega t - \beta z)}. \tag{2.45b}$$

The phase front of the wave is given by $(\omega t - \beta z) = k$, where k is a constant. Upon differentiating this expression, one obtains $\omega dt - \beta dz = 0$, giving the phase velocity

$$v_p = \frac{dz}{dt} = \frac{\omega}{\beta(\omega)}. \tag{2.46}$$

However, because the phase velocity represents the of the velocity phase front of the carrier wave, this may not be the velocity at which the voltage pulse itself propagates. As a result, the phase velocity of any wave cannot be directly measured, only indirectly inferred.

2.3.2 The Group Velocity

The difference between the group velocity and the phase velocity was first described by Lord Rayleigh in 1877 [68]. If the medium is homogeneous and is non-dispersive, then the phase velocity is found to be equal to the group velocity. This, however, is not the case for dispersive, absorptive media.

In order to derive an expression for the group velocity, consider the spectral representation of a temporal pulse on a dispersive attenuative transmission line. Let the input voltage pulse at $z = 0$ be given by

$$V(t) = V_0^+ f(t) \tag{2.47}$$

where V_0^+ is the magnitude of the input pulse voltage and $f(t)$ represents an expression for a periodic wave pulse. The temporal frequency spectrum of the input pulse voltage is then given by

$$\tilde{V}(\omega) = V_0^+ \tilde{f}(\omega) \tag{2.48}$$

where

$$\tilde{f}(\omega) = \int_{-\infty}^{\infty} f(t) e^{-j\omega t} dt, \tag{2.49}$$

with its inverse Fourier Transform

$$f(t) = \frac{1}{2\pi} \int_{-\infty}^{\infty} \tilde{f}(\omega) e^{j\omega t} d\omega. \tag{2.50}$$

For an envelope modulated sine wave pulse with fixed angular carrier frequency $\omega_c = 2\pi f_c$,

$$f(t) = u(t) \sin(\omega_c t) \tag{2.51}$$

with envelope spectrum

$$\tilde{u}(\omega) = \int_{-\infty}^{\infty} u(t) e^{-j\omega t} dt, \tag{2.52}$$

the temporal frequency spectrum of the input pulse function $f(t)$ is given by [61]

$$\begin{aligned} \tilde{f}(\omega) &= \int_{-\infty}^{\infty} u(t) \sin(\omega_c t) e^{j\omega t} d\omega \\ &= \frac{1}{2j} \left[\tilde{u}(\omega - \omega_c) - \tilde{u}(\omega + \omega_c) \right]. \end{aligned} \tag{2.53}$$

If $u(t)$ is real-valued then $\tilde{u}^*(\omega) = \int_{-\infty}^{\infty} u(t) e^{-j\omega t} dt = \tilde{u}(-\omega)$; that is, the complex conjugate of the envelope spectrum for a real-valued function is equal to the spectrum at negative frequencies [61].

Consider substituting $-\omega$ for ω in the expression for $\tilde{u}(\omega + \omega_c)$. Then,

$$\tilde{u}(\omega + \omega_c) \rightarrow \tilde{u}(-\omega + \omega_c) = \tilde{u}^*(\omega - \omega_c)$$

and Eq. (2.53) becomes

$$\begin{aligned}\tilde{f}(\omega) &= \frac{1}{2j}\left[\tilde{u}(\omega-\omega_c) - \tilde{u}^*(\omega-\omega_c)\right] \\ &= \Im\{\tilde{u}(\omega-\omega_c)\}. \end{aligned} \tag{2.54}$$

The propagated pulse in the forward direction is given by

$$V^+(z,t) = \frac{1}{2\pi}V_0^+ \int_{-\infty}^{\infty} \tilde{f}(\omega) e^{j(\omega t - \beta(\omega)z)} d\omega. \tag{2.55}$$

With $\tilde{f}(\omega) = \Im\{\tilde{u}(\omega-\omega_c)\}$ peaked at ω_c, the propagation factor $\beta(\omega)$ can be expanded in a Taylor Series about ω_c as

$$\beta(\omega) = \beta(\omega_c) + \beta'(\omega_c)(\omega-\omega_c) + \frac{1}{2}\beta''(\omega_c)(\omega-\omega_c)^2 + \ldots \tag{2.56}$$

One can make use of the first-order approximation to directly obtain an expression for the group velocity. To first-order, $\beta(\omega)$ and $\alpha(\omega)$ may be approximated as

$$\beta(\omega) \approx \beta(\omega_c) + \beta'(\omega_c)(\omega-\omega_c)$$

and

$$\alpha(\omega) \approx \alpha(\omega_c).$$

Within this approximation, the propagated voltage pulse, in Eq. (2.55), in the forward direction becomes

$$V^+(z,t) \approx V_0^+ e^{-\alpha(\omega_c)z} \frac{1}{2\pi} \int_{-\infty}^{\infty} \tilde{f}(\omega) e^{j(\omega t \beta(\omega_c)z - \beta'(\omega_c)(\omega-\omega_c)z)} d\omega, \tag{2.57}$$

which may be evaluated as

$$V^+(z,t) \approx V_0^+ f(t - \beta'(\omega_c)z)e^{-(\alpha(\omega_c)-j\beta(\omega_c)z)}e^{-j\omega_c(t-\beta'(\omega_c)z)}. \tag{2.58}$$

In this linear approximation, the pulse propagates with an undistorted shape, though uniformly attenuated in amplitude with propagation distance z and is uniformly phase-shifted with z, and travels with the group velocity given by $dt - \beta'(\omega_c)dz = 0$ or

$$\frac{dz}{dt} = \frac{1}{\beta'(\omega_c)} = \frac{1}{(\partial\beta/\partial\omega)_{\omega_c}} \tag{2.59}$$

which is evaluated at the input carrier frequency ω_c. Here, we have the well-known first-order expression for the group velocity [67].

The approximation can be extended to the second-order where

$$\beta(\omega) \approx \beta(\omega_c) + \beta'(\omega_c)(\omega - \omega_c) + \frac{1}{2}\beta''(\omega_c)(\omega - \omega_c)^2. \tag{2.60}$$

With this quadratic approximation, the propagated voltage pulse in the forward direction in Eq. (2.57) becomes

$$V^+(z,t) \approx V_0^+ e^{-\alpha(\omega_c)z}\frac{1}{2\pi}\int_{-\infty}^{\infty}\tilde{f}(\omega)e^{j(\omega t\beta(\omega_c)z-\beta'(\omega_c)(\omega-\omega_c)z-\frac{1}{2}\beta''(\omega_c)(\omega-\omega_c)^2 z)}d\omega, \tag{2.61}$$

which simplifies to

$$V^+(z,t) \approx V_0^+ e^{-\alpha(\omega_c)z}e^{j(\omega_c t-\beta(\omega_c)z)}\frac{1}{2\pi}\int_{-\infty}^{\infty}\tilde{f}(\omega)e^{-j\frac{1}{2}\beta''(\omega_c)(\omega-\omega_c)^2}e^{j(t-\beta'(\omega_c)z)(\omega-\omega_c)}d\omega \tag{2.62}$$

and can then be evaluated by completing the square in the exponent of the integrand,

where $\zeta = \omega - \omega_c$,

$$\begin{aligned}\frac{1}{2}\beta''\zeta^2 - (t-\beta' z)\zeta =& \frac{1}{2}\beta''\left(\zeta^2 - \frac{t-\beta' z}{\beta''/2}\zeta + \frac{(t-\beta'\zeta)^2}{\beta''^2}\right) - \frac{1}{2}\beta''\frac{(t-\beta' z)^2}{\beta''^2} \\ =& \frac{1}{2}\beta''\left(\zeta - \frac{t-\beta' z}{\beta''}\right)^2 - \frac{(t-\beta' z)^2}{2\beta''}\end{aligned} \tag{2.63}$$

so that, with the change of variable $\zeta = \omega - \omega_c$ in the integrand, one obtains

$$V^+(z,t) \approx V_0^+ e^{-\alpha(\omega_c)z} e^{j(\omega_c t - \beta(\omega_c)z)} e^{j\frac{(t-\beta'(\omega_c)z)^2}{2\beta''(\omega_c)}} \int_{-\infty}^{\infty} \tilde{f}(\zeta+\omega_c) e^{j\frac{1}{2}\beta''(\zeta - \frac{t-\beta' z}{\beta''})^2} d\zeta. \tag{2.64}$$

Let $\Omega = \zeta - \frac{t-\beta' z}{\beta''}$ so that

$$\begin{aligned}V^+(z,t) \approx & V_0^+ e^{-\alpha(\omega_c)z} e^{j(\omega_c t - \beta(\omega_c)z)} e^{j\frac{(t-\beta'(\omega_c)z)^2}{2\beta''(\omega_c)}} \\ & \cdot \int_{-\infty}^{\infty} \tilde{f}\left(\Omega + \omega_c + \frac{t-\beta'(\omega_c)z}{\beta''}\right) e^{j\frac{1}{2}\beta''(\omega_c)\Omega^2} d\Omega.\end{aligned} \tag{2.65}$$

This is the Fresnel transform of $\tilde{f}$, which can be used to describe the propagation of an optical pulse in a waveguide. This second-order term shows that the pulse travels at the group velocity $v_g = 1/\beta'(\omega_c)$ while the shape is distorted by an amount dependent upon $\beta''(\omega_c)$, called the group velocity dispersion (GVD) [66].

2.3.3 The Energy Centrovelocity

The average energy centrovelocity of the pulse is defined by the quantity [62, 66]

$$v_{cv} = \frac{z}{\langle t_z \rangle - \langle t_0 \rangle} \tag{2.66}$$

where

$$\langle t_z \rangle = \frac{\int_{-\infty}^{\infty} tS(z,t)dt}{\int_{-\infty}^{\infty} S(z,t)dt} \tag{2.67}$$

is the arrival time of the temporal centroid of the pulse energy at the position $z \geq 0$ along the transmission line, and

$$\langle t_0 \rangle = \frac{\int_{-\infty}^{\infty} tS(0,t)dt}{\int_{-\infty}^{\infty} S(0,t)dt} \tag{2.68}$$

is the temporal centroid of the input pulse energy. Here,

$$S(z,t) = V(z,t)I(z,t) \tag{2.69}$$

describes the instantaneous pulse energy at the position $z \geq 0$ along the transmission line. With the voltage $V(z,t)$ and current $I(z,t)$ calculated at any position $z \geq 0$ along the transmission line, both $\langle t_z \rangle$ and $\langle t_0 \rangle$ may be numerically determined and the average centrovelocity v_{cv} computed at an input pulse carrier frequency ω where $\tilde{I}(z,\omega) = \tilde{V}(z,\omega)/Z(\omega)$ and $Z(\omega)$ is the characteristic impedance of the line at that point.

Notice that the instantaneous energy centrovelocity of the pulse is given by the limit

$$v_{cv_{inst}}(z) = \lim_{\Delta z \to 0} \frac{\Delta z}{\langle t_{z+\Delta z} \rangle - \langle t_z \rangle} \tag{2.70}$$

where $\langle t_z \rangle$ and $\langle t_{z+\Delta z} \rangle$ are defined in Eq. (2.67). However, the time it takes for a pulse to travel the distance z is determined from the average centrovelocity that is given by Eq. (2.66). If T is the time it takes for the energy centroid of the pulse to travel the distance z, then that propagation distance is given by the traditional

time-of-flight definition using the centrovelocity $z = v_{cv}T$.

These numerical results can then be compared to the group velocity and phase velocity as a function of ω. As an example, consider the Debye model [69] of frequency dispersion in the dielectric permittivity presented in Appendix A. For a single relaxation model, the relative dielectric permittivity is given by

$$\epsilon(\omega)/\epsilon_0 = \epsilon_\infty - \frac{\epsilon_\infty - \epsilon_s}{1 - i\tau\omega} \tag{2.71}$$

where $\epsilon_s = \epsilon(0)/\epsilon_0$ denotes the static zero frequency relative permittivity and where $\epsilon_\infty = \lim_{\omega\to\infty} \epsilon(\omega)/\epsilon_0$ is the high frequency relative permittivity. The constant τ describes the relaxation time for the orientational polarization phenomenon. Values representative of loamy soil with 0% moisture content are given by

$$\epsilon_\infty = 2.44,$$

$$\epsilon_s = 7.51,$$

$$\tau = 1.032 \times 10^{-5}\text{s},$$

and are used in the numerical calculations presented in this dissertation. With $\mu/\mu_0 = 1$, the complex index of refraction of the Debye model dielectric is given by

$$\begin{aligned} n(\omega) &= \left[\frac{\mu\epsilon(\omega)}{\mu_0\epsilon_0}\right]^{1/2} \\ &= \left[\epsilon_\infty - \frac{\epsilon_\infty - \epsilon_s}{1 - i\tau\omega}\right]^{1/2}, \end{aligned} \tag{2.72}$$

with derivative

$$n'(\omega) = -i\tau \frac{\epsilon_\infty - \epsilon_s}{2n(\omega)(1 - i\tau\omega)^2}. \tag{2.73}$$

With the complex wavenumber given by $\tilde{k}(\omega) = (\omega/c)n(\omega)$, the complex group velocity is given by

$$\tilde{v}_g = \frac{1}{\partial\tilde{k}(\omega)/\partial\omega} = \frac{c}{n(\omega) + \omega n'(\omega)} \tag{2.74}$$

with associated complex group delay

$$\tilde{t}_g(\omega)\frac{1}{c}\left(n(\omega) + \omega n'(\omega)\right). \tag{2.75}$$

This is to be compared with the real group velocity

$$v_g(\omega) = \frac{1}{\partial\beta(\omega)/\partial\omega} = \frac{c}{n_r(\omega) + \omega n_r'(\omega)} \tag{2.76}$$

where ω is real and $n_r(\omega) = \Re\{n(\omega)\}$ with $\beta(\omega) = \Re\{\tilde{k}(\omega)\}$. Thus, when ω is real,

$$\Re\{\tilde{t}_g\} = \frac{1}{c}\left(n_r(\omega) + n_r'(\omega)\right) \tag{2.77}$$

which is just the real group delay $t_g(\omega) = v_g^{-1}(\omega)$. Therefore,

$$v_g(\omega) = \Re\{\tilde{v}_g(\omega)\} \tag{2.78}$$

for real-valued ω, and the real group velocity is indeed given by the real part of the complex group velocity when ω is real valued. Notice that this is in general for true for complex ω.

As stated by G.B. Whitham in his now classic text on Linear and Nonlinear

Waves [?], "$|A|^2$ propagates with the group velocity." Here, A refers to the complex amplitude of the wave. Furthermore, $|A|^2$ is an "energy-like quantity." The group velocity is then sen to have a dual characteristic in dispersive wave propagation. First, "different wavenumbers propagate with the group velocity", where different wavenumbers $k(\omega)$ correspond to monochromatic waves that describe the wave group, or pulse. Secondly, $|A|^2$ is related to the average flow of energy in the wave, where

$$\mathcal{F} = v_g(k)\xi.$$

Here, $\mathcal{F}$ is the average "energy flux" in the wave group and ξ is the average "energy density" in that wave group.

Although this energy flow equation is claimed [?] to be completely general, it is not as it only applies to the case where this no dispersive loss. Because this may be the cause of errors in Time Domain Reflectometry (TDR), for example, it is critical to obtain what the pulse velocity measure is most appropriate to use in a dispersive absorptive medium. It is proposed there that this pulse velocity is the energy centrovelocity described by Eqs. (2.66) - (2.69). This is done for the following reasons:

1. it reduces the group velocity in the absence of dispersive loss,

2. like the propagation of information, it is causal,

3. it is measurable,

4. the result is independent of both the initial pulse shape and its duration.

As an example, consider the determination of the average energy centrovelocity v_{cv}

in a dispersive attenuative dielectric medium whose relative permittivity is given by Eq. (2.71) with model parameters representative of loamy soil with 0% moisture content. The initial voltage pulse is a single cycle trapezoidal with equal rise and fall times. This initial pulse structure is illustrated in Fig. 2.5.

The velocity behavior with respect to frequency of this propagated pulse is plotted in Fig. 2.6. The group velocity, the phase velocity, and the energy centrovelocity are all compared.

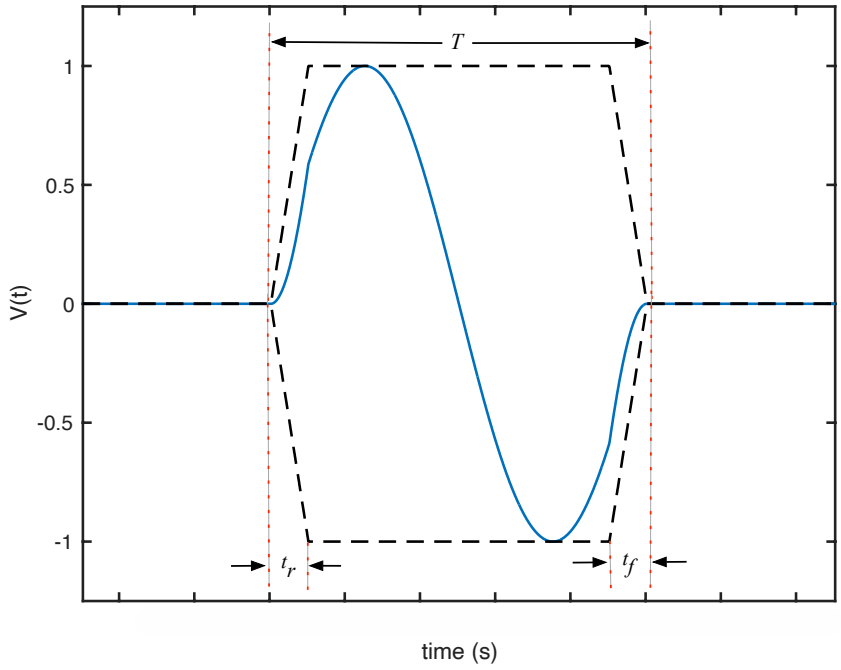

Figure 2.5: Single cycle trapezoidal envelope pulse with equal rise t_r and fall t_f times. The overall initial pulse width is given by the inverse of the applied carrier frequency f_c.

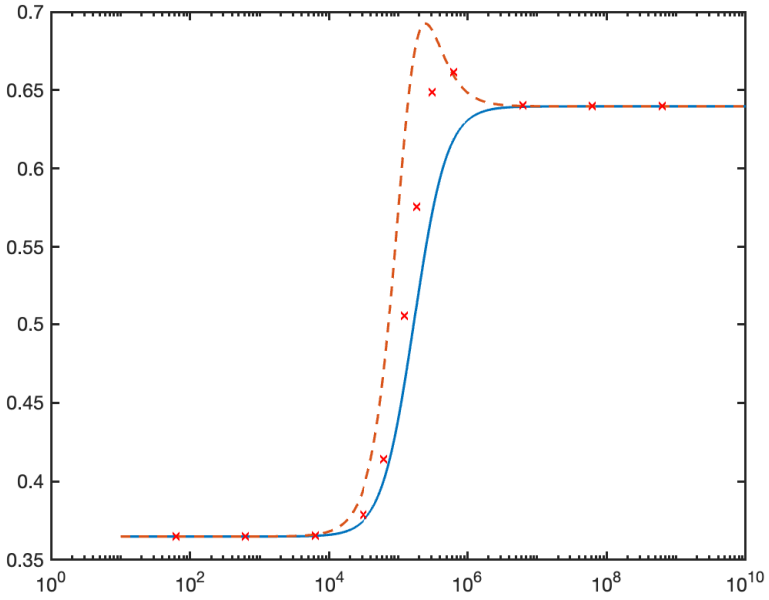

Figure 2.6: Velocity calculations of the trapezoidal envelope pulse through a Debye model of loamy soil with 0% moisture content. The blue line is phase velocity. The dashed orange line is the group velocity. The red 'x' points are centroid velocity.

The behavior of the calculated pulse energy centrovelocity v_{cv} relative to the group velocity $v_g(\omega_c)$ at the input pulse angular frequency $\omega_c = 2\pi f_c$ is presented in Fig. 2.7. as a function of the relative propagation distance z to the absorption depth z_d at that frequency.

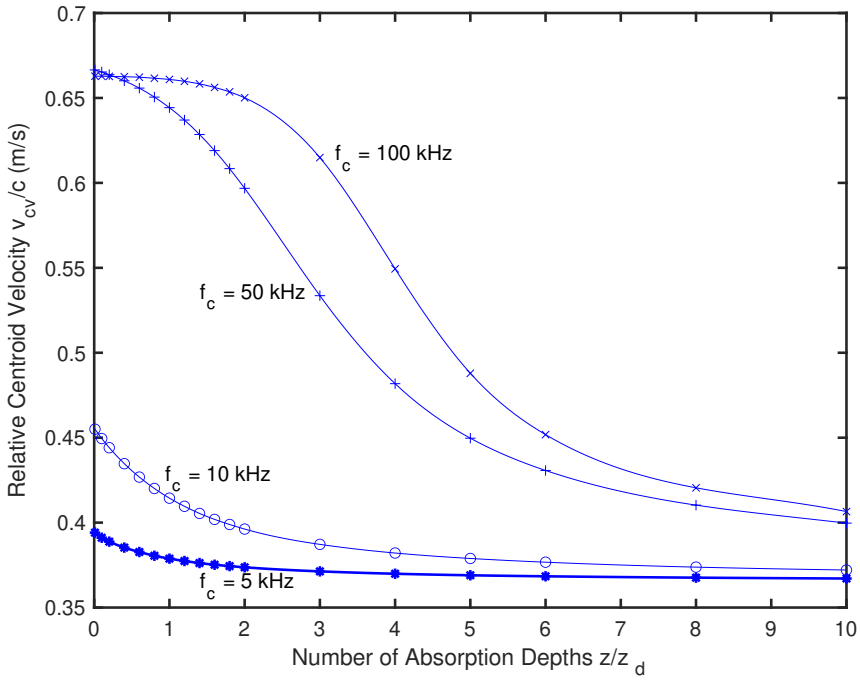

Figure 2.7: Calculated pulse energy centrovelocity v_{cv} relative to the group velocity $v_g(\omega_c)$ at different input pulse angular frequency $\omega_c = 2\pi f_c$ as a function of the relative propagation distance z to the absorption depth z_d at each frequency.

Notice that, with the relaxation time of the medium given by $\tau = 1.032 \times 10^{-5}$ s, the dielectric dispersion is rapidly changing about the frequency $f_\tau \approx 1/\tau = 1 \times 10^5$ Hz. This is also the frequency about which the material absorption is the greatest and changing most rapidly with frequency. See Fig. A.1 in Appendix A for this absorption behavior. This characteristic frequency f_τ then helps explain the behavior of the relative centrovelocity curves in Fig. 2.7. The largest variation in v_{cv}/v_g occurs when the applied pulse carrier frequency f_c is approximately the relaxation time frequency f_τ; that is, when $f_c = 1 \times 10^5$Hz. For smaller frequencies near the "base" of the dispersion curve, illustrated by the $f_c = 5$kHz and $f_c = 10$kHz curves in Fig. 2.7, the dispersion is less than their centrovelocity decreases with propagation distance

z/z_d in a manner that is similar to exponential decay. For larger carrier frequencies near f_τ ($f_c = 50$ kHz), the decrease is characteristic of that for $f_c = f_\tau$. Notice that each curve approaches unity as $z/z_d \to 0^+$; that is, the group velocity is only approximately valid when the propagation distance is very small ($z \ll z_d$), its validity decreasing as z increases.

Because the pulse centrovelocity decreases as z increases, estimates of the distance and the pulse has propagated using "time of flight" measurements will be smaller than the actual distance, the error in measured distance increasing with z. Use of the average pulse energy centrovelocity v_{cv} for this estimate will undoubtedly be very accurate. As can be imagined, this will be of critical importance to Time Domain Reflectometry when the transmission line is dispersive.

Chapter 3

Transmission Line Models

Different transmission line geometries have been developed [41, 59, 70], based upon their effectiveness in a variety of applications. Some of the more common examples include, but are not limited to, coaxial cables, twisted shielded pairs, and microstrip lines. Coaxial cables are perhaps one of the most well know types of transmission lines in existence today. They are ideal for such uses as television cables or precision measurement devices. In communications applications, twisted shielded pairs on utility poles are often the ideal choice because they reduce the effects of noise and cross-talk in the system [41]. Finally, microstrip transmission lines lend themselves well to simple fabrication of printed circuit boards [59].

The understanding of transmission line models is essential for improving the practical uses of transmission lines, such as for those Time Domain Reflectometry (TDR) applications that were described in Chapter 1. For this purpose, three different transmission line geometries are presented and compared in this chapter, these being the coaxial cable, the single microstrip, and the coupled microstrip. A Debye-type dielectric material model (see Appendix A) of the dispersive and attenuative microstrip

substrate is assumed as this causal model is the most appropriate throughout the low frequency domain of interest. The cross-sectional geometry, material properties, and circuit model representations of a coaxial cable, a single microstrip, and a coupled microstrip transmission line are illustrated in Figs. 3.1 through 3.3 and Fig. 3.5, respectively. Each of these geometries are individually considered in the remaining sections of this chapter.

In addition, expressions for the effective dielectric permittivity $\epsilon_{eff}(\omega)$ are developed for both the single and coupled microstrip transmission line models. Both material properties and the cross-sectional geometry of the particular transmission line influence the value of the effective dielectric permittivity, and ultimately impacts the dispersive behavior of the transmission line. For example, microstrip transmission lines make use of the interaction between air and the dielectric substrate material for its guidance properties. It is this interaction that creates the effective dielectric permittivity. Because of the inherent material dispersion, frequency dependent losses will occur along the transmission line that highly influence the dispersion properties of the wave propagation along the line. This waveguide dispersion results in pulse distortion along the transmission line [71]. Such dispersive losses are often neglected in the literature, but they are one of the main areas of focus in this dissertation as their influence on observable pulse propagation effects may be used in practice to determine the material properties.

The dispersion relations for each transmission line model are derived in this chapter and then applied to specific waveguide geometries in order to determine their effect on the distributed circuit parameters and the resultant propagation factor for that geometry. The distributed circuit model for transmission lines and its role in

modeling the pulse propagation analysis is then described in this chapter. The numerical analysis of the propagation for each waveguide geometry considered in this dissertation is then presented in Chapter 4.

3.1 The Coaxial Cable

Coaxial cables are one of the most commonly used transmission lines, ranging in uses from cable television to communications to high precision measurement devices [59], such as the Time Domain Reflectometry (TDR) probe. As is well-known from undergraduate electromagnetics texts, the inner and outer conductors of the coaxial cable are highly effective at containing the electromagnetic field to the enclosed dielectric region [59]. The first patent for the coaxial cable is credited to the mathematician Oliver Heaviside in 1880 [42]. An insulator was placed in between the two wires, which allowed them to act independently of each other. An early model of the coaxial cable was developed by Schelkunoff [72] in 1934. This model used the physical geometry introduced by Heaviside and applied a rigorous analysis of electromagnetic field theory to the coaxial transmission line in an idealized situation when it was perfectly straight and infinite in length. Employing modified Bessel functions, Maxwell's equations were evaluated to describe the impedance of each conductor. More recently, Tesche's model of the coaxial cable [71] successfully simplified Schelkunoff's [72] per-unit parameters of a lossy, non-dispersive cable. In doing so, Tesche developed an equivalent distributed circuit model in the low- and high-frequency ranges.

Because of its simplicity, the coaxial cable geometry and electrical properties given in this chapter follows the model given by Chipman [41]. At its most basic form, a

coaxial cable consists of a cylindrical internal conductor surrounded by a cylindrical, annular insulator contained within an annular conductor. The insulator is typically made of a dielectric material, such as polystyrene or polytetrafluoroethylene (PTFE) [60]. Chipman [41] describes the orientation of the coaxial cable as "solid homogenous wires of circular cross-section" with "tubular conductors of circular periphery." Figure 3.1 illustrates the cross-sectional geometry of the coaxial cable. The cross-section of the inner cable holds a radius of r_1 meters. The inner surface of the surrounding coaxial conductor is defined by a radius of r_2 meters. The insulating material lies between these two surface within the annular region $r_1 < r < r_2$. Both the inner and outer conductors are assumed to be ideal with infinite conductivity.

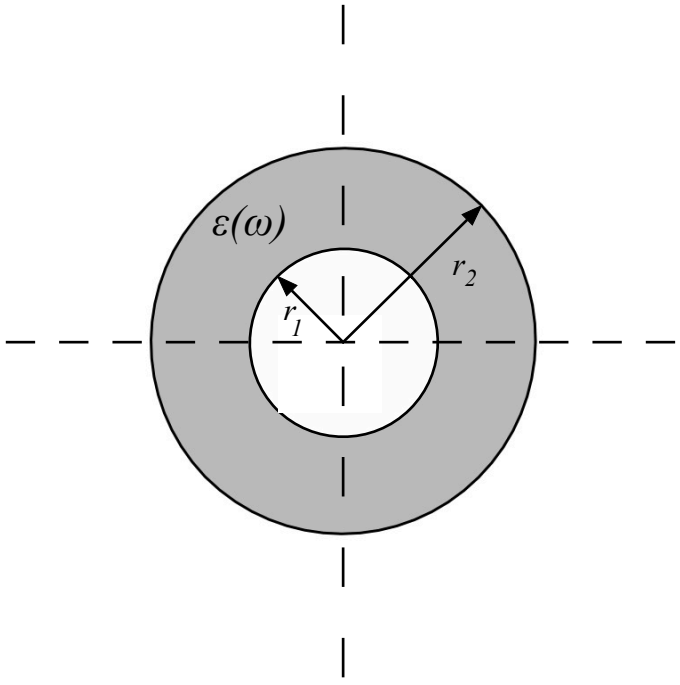

Figure 3.1: Coaxial cable model with inner conductor of radius r_1 and outer conductor of radius r_2. Each conductor is separated by an imperfect dielectric material in the region $r_1 < r < r_2$, with complex dielectric permittivity $\epsilon(\omega)$

As a result of the conductive and insulating properties of the materials, there exists

an internal resistance and conductance distributed along the length of the cable. The inner conductor gives rise to the resistance R and inductance L. The separation of the outer from the inner conductor provides a capacitance C and conductance G. As provided by Miner [60], a visual representation of the distributed circuit model of the coaxial cable is shown in Fig. 3.2.

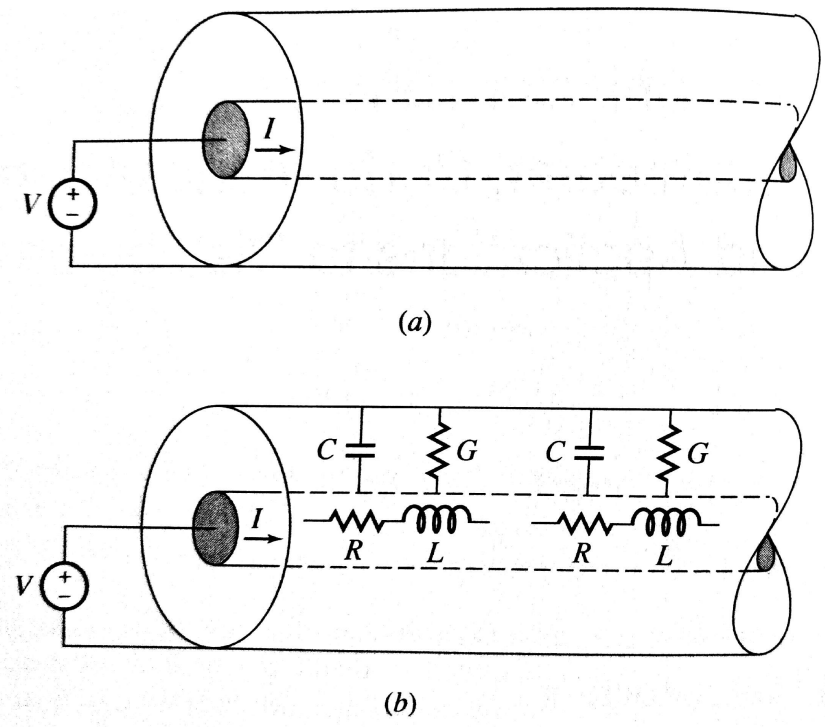

Figure 3.2: Coaxial cable geometry and corresponding distributed parameter circuit model as defined by Miner [60].

Miner [60] provides a detailed description of how the material properties and geometry of the coaxial cable determines the values of the circuit parameters. Because the overall length of the cable impacts the resistance, inductance, capacitance, and conductance, these parameters are represented in per unit length units so that they are independent of the total length of the transmission line. Current flow through

the coaxial cable gives rise to the formation of the circuit parameters [60] along with the dimensions and material properties of the inner and outer conductors. The various relationships between the circuit parameters and the physical properties of the conductors are given in Chapter 9 of Cheng's text [59], where r_1 is the radius of the center conductor, and r_2 is the inner radius of the outer conductor, as depicted in Fig. 3.1. These are the following:

The resistive properties of the inner and outer conductors create a series resistance R per unit length that may be expressed as [59]

$$R = \frac{1}{\pi a}\sqrt{\frac{\pi f \mu_c}{\sigma_c}}, \tag{3.1}$$

where σ_c and μ_c are the inherent electric conductivity and magnetic permeability of the conductor, respectively. A magnetic flux is produced in and around the wire when current flows through the wire. As a result, an inductance L arises and is given by the ratio of that magnetic flux to the current flow. When written in terms of the permeability and dimensions of the coaxial cable this inductance per unit length is given by [59]

$$L = \frac{\mu}{2\pi}\ln\frac{r_2}{r_1}. \tag{3.2}$$

The capacitance C arises from the electric potential between the two conductors, and when written in terms of the geometry is [59]

$$C = \frac{2\pi\epsilon}{\ln(r_2/r_1)}, \tag{3.3}$$

where ϵ is the dielectric permittivity of the insulating dielectric between the inner and outer conductors. As the current flows between the inner and outer conductors, an

effective resistance arises between them due to the lossy dielectric. Because this resistance is in parallel with the resistance in the wire, it is represented as a conductance G per unit length [59], given by

$$G = \frac{2\pi\sigma}{\ln(r_2/r_1)}. \tag{3.4}$$

3.2 The Single Microstrip Line

Microstrip transmission lines, as found in microwave circuits, can appear in applications of digital communications, computers, and radar. They are fabricated on printed circuit boards with a conductive strip of copper or gold, a dielectric substrate made of silicon or similar material, and a ground plane. A visual representation of the cross section of a single microstrip line is given in Fig. 3.3. The relative dielectric constant of the air surrounding the microstrip line is, to a very good approximation, equal to unity. The conductive segment of the microstrip line has a width w. Finally, b is the thickness of the imperfect nonmagnetic dielectric substrate that has a complex dielectric permittivity of $\epsilon_s(\omega)$, which is frequency dependent

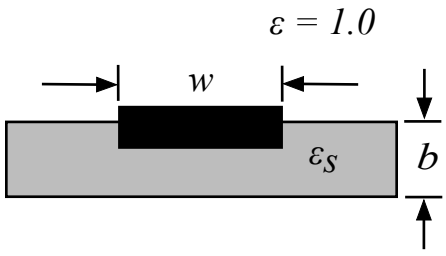

Figure 3.3: Cross-section of a single microstrip geometry as defined by Getsinger [26]. The conductive segment holds width w, the substrate thickness is b, and the substrate dielectric permittivity of $\epsilon_s(\omega)$. The relative dielectric constant of the air surrounding the microstrip line is taken as $\epsilon = 1.0$.

One unique characteristic of the microstrip line is the relative influence between the air above and the dielectric substrate below and on the sides of the conductive strip. This interaction results in an effective dielectric permittivity that leads to impactful dispersion effects. As a result, the phase constant, which describes the phase angle evolution of a propagating sinusoidal voltage pulse, becomes a complicated function of the carrier frequency, which by itself will then result in the pulse being dispersed as if it propagates. Because of this, the single microstrip transmission line can only be a pure-TEM mode waveguide at zero frequency. At higher frequencies, the frequency-dependence of the microstrip line gives rise to a slight longitudinal component associated with the propagation of the electric and magnetic fields relative to the propagation direction. This results in the microstrip line behaving as a quasi-TEM waveguide. The effective dielectric permittivity $\epsilon_{eff}(\omega)$ introduced here captures the dispersive behavior of the microstrip transmission line.

Much of the previously published work [2, 26, 73, 74] has attempted to develop an expression for the dispersion effects caused by the air-substrate combination surrounding the microstrip line. The effective dielectric permittivity $\epsilon_{eff}(\omega)$ is the primary parameter that describes this dispersive effect. The quantity $\epsilon_{eff}(\omega)$ varies with frequency and impacts the propagation factor of the pulse, which then leads to dispersive distortion of the pulsed waveform as it propagates along the transmission line.

The per unit length inductance L' and capacitance C' of the microstrip transmission line can be found in terms of the effective dielectric permittivity at zero frequency ϵ_{e0} by making use of the physical properties of the transmission line in the air region and the substrate-region. These solutions for L' and C' will ultimately influence $\epsilon_{eff}(\omega)$.

The air-region of the microstrip transmission line is considered first in this analysis. The phase velocity in the air $v_{p,a}$ is given by

$$v_{p,a} = \frac{1}{C'_a L'} \approx c. \tag{3.5}$$

and is approximately equal to the speed of light c in vacuum. As has been described previously, the dielectric permittivity differs between the air region and the substrate, so that the per unit capacitance of the air region alone, denoted by C'_a, is different from that for a transmission line surrounded by vacuum (air). However, the magnetic permeability is not impacted by either medium and is approximately equal to unity in both the air and the substrate. Because the inductance is a result of the magnetic flux, it is also minimally impacted and a separate term that describes the per unit inductance of the air is not required [75].

In order to determine L' and C', each material region needs to be analyzed separately. From Eq. (3.5), the inductance per unit length is seen to be given by,

$$L' = \frac{1}{c^2 C_a}. \tag{3.6}$$

By definition [60], the per unit length characteristic impedance of a transmission line is given by the square root of the ratio of the inductance per unit length to the capacitance per unit length, i.e.

$$Z_0 = \sqrt{\frac{L'}{C'}}. \tag{3.7}$$

With Eq. (3.6), this expression becomes

$$Z_0 = \frac{1}{c}\sqrt{\frac{1}{C'C'_a}}. \tag{3.8}$$

Since L' is unaffected by either the air or substrate medium, it follows that the relation $\epsilon_{e0} = C'/C'_a$ is established to describe the permittivity between the air and dielectric regions at zero frequency [75]. The characteristic impedance can then be written in terms of ϵ_{e0} as

$$Z_0 = \frac{\sqrt{\epsilon_{e0}}}{cC'}, \tag{3.9}$$

so that

$$C' = \frac{\sqrt{\epsilon_{e0}}}{cZ_0}. \tag{3.10}$$

With the expression $\eta_0 = 1/(\epsilon_0 c)$ for the intrinsic impedance, the speed of light in air may be expressed as $c = 1/\epsilon_0\eta_0$, so that, Eq. (3.10) becomes

$$\frac{C'}{\epsilon_0} = \frac{\sqrt{\epsilon_{e0}}\eta_0}{Z_0}, \tag{3.11}$$

which is that given in Eq. (1b) by Getsinger [26].

Consider next obtaining an expression for the per unit length inductance L' of the microstrip line with Eq. (3.11). The expression $Z_0 = \sqrt{L'/C'}$ for the characteristic impedance becomes

$$Z_0 = \sqrt{\frac{L'Z_0}{\sqrt{\epsilon_{e0}}\epsilon_0\eta_0}}, \tag{3.12}$$

so that

$$L' = Z_0\sqrt{\epsilon_{e0}}\epsilon_0\eta_0. \tag{3.13}$$

Because $\eta_0 = \sqrt{\mu_0/\epsilon_0}$, this equation yields the relation

$$L' = Z_0\sqrt{\epsilon_{e0}\epsilon_0\mu_0}. \tag{3.14}$$

Upon multiplying this equation through by η_0 in order to remove the ϵ_0 term, one obtains the expression

$$L'\eta_0 = Z_0\sqrt{\epsilon_{e0}\epsilon_0\mu_0}\sqrt{\frac{\mu_0}{\epsilon_0}}, \tag{3.15}$$

which finally yields the relation

$$\frac{L'}{\mu_0} = \frac{Z_0}{\eta_0}\sqrt{\epsilon_{e0}}. \tag{3.16}$$

This expression is found to be in agreement with Eq. (1a) of Getsinger [26]. Equations (3.11) and (3.16) are next used to develop relations between the geometries of the standard microstrip model and the Longitudinal Section Electric (LSE) model that is now described.

LSE Model of the Single Microstrip Transmission Line

A single microstrip transmission line is a quasi-TEM mode waveguide due to the influence of the air surrounding the conductive segment of the stripline [2]. Quasi-TEM waveguides cannot be easily analyzed because they do not have an exact solution like that for a pure TEM waveguide. Consequently, Getsinger [26] simplifies the quasi-TEM problem by treating the single microstrip as a Longitudinal Section Electric (LSE) mode waveguide due to its ability to be analyzed more directly. The LSE model makes use of the linear superposition of the TE and TM modes of the waveguide.

The single microstrip is then approximated as a series of parallel plate transmission lines. Getsinger's [26] LSE model of the microstrip transmission line is depicted in Fig. 3.4.

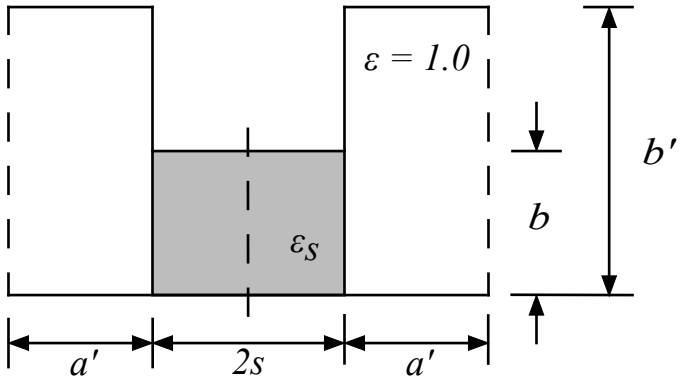

Figure 3.4: Longitudinal Section Electric (LSE) model of the single microstrip, with substrate length $2s$, substrate thickness b, and substrate dielectric constant ϵ_s. The quantities b' and a' are the dimensions of the region of air surrounding the substrate. The dielectric permittivity of the air is taken as $\epsilon = 1.0$. This model follows the description given by Getsinger in [26].

The LSE model is described as one parallel plate transmission line with a dielectric permittivity ϵ_s, width $2s$, and height b, indicated by the shaded section in Fig. 3.4. Two additional parallel plate transmission lines are connected to either side of the dielectric filled parallel plate transmission line. These sections are air-filled with a dielectric permittivity of $\epsilon = 1.0$, with width a', and height b', as illustrated.

In order to determine the per unit inductance L'_{LSE} and capacitance C'_{LSE} of the LSE model, the definition of the inductance L and capacitance C of the parallel plate transmission line are first considered, where

$$L = \mu_0 \frac{\mu_r H}{W}, \tag{3.17a}$$

$$C = \epsilon_0 \frac{\epsilon_r W}{H}. \tag{3.17b}$$

Here ϵ_r and μ_r are, respectively, the relative dielectric permittivity and magnetic permeability of the media in a parallel plate transmission line, where W is the width, and H is the height. When applied to the case of the LSE model shown in Fig. 3.4, the previous equations are replaced by a summation of the geometric properties of each region,

$$L'_{LSE} = \mu_0 \left[\frac{b}{2s} + \frac{b'}{2a} \right] \tag{3.18a}$$

$$C'_{LSE} = \epsilon_0 \left[\frac{\epsilon_s (2s)}{b} + \frac{2a'}{b'} \right]. \tag{3.18b}$$

After some algebraic rearrangement, these relations may be cast into a form that is in agreement with Getsinger's definitions of the inductance and capacitance [26], where

$$\frac{L'}{\mu_0} = \frac{1}{2[(s/b) + (a'/b')]}, \tag{3.19a}$$

$$\frac{C'}{\epsilon_0} = 2 \left[\epsilon_s \frac{s}{b} + \frac{a'}{b'} \right]. \tag{3.19b}$$

The transverse resonance method [70, 76] allows one to use circuit theory methods to set up algebraic equations describing the properties of a microstrip transmission line. This method is typically used to determine the modes of a waveguide and it's cutoff frequency. The transverse resonance method is used here to define equations for the propagation factor, which may ultimately be used to determine the dielectric permittivity of the surrounding material. From the definition of transverse resonance, the sum of the impedances on either side of the air-dielectric interface are set equal

to zero. Therefore, the sum of the impedance on the air-side of the interface is

$$Z_a + Z_{as} + \epsilon_a Z_0 = 0, \tag{3.20}$$

where Z_a is the the impedance of the air-side, Z_{as} is the impedance at the interface of the air and the substrate, Z_0 is the impedance of free space, and $\epsilon_a = 1$ is taken as the dielectric permittivity of the air. On the substrate-side of the air-dielectric interface, the sum of the impedance is

$$Z_s + Z_{as} + \epsilon_s Z_0 = 0. \tag{3.21}$$

Here, Z_s is the impedance of the substrate and ϵ_s is the dielectric permittivity of the substrate. At the magnetic walls, which are open circuits that are represented by the dashed lines in Fig. 3.4, the sum of the impedances is

$$Z_{in_a} + Z_{in_s} = 0, \tag{3.22}$$

where Z_{in_a} is the input impedance on the air-side of the magnetic wall, and Z_{in_s} is the input impedance on the dielectric-side of the magnetic wall.

In a lossless transmission line, the impedance is given by the ratio of the capacitance to the inductance, $Z = C/L$, so that application of this identification to Eqs. (3.20) and (3.21) in order to bring each expression into terms that appropriate for the propagation factor of the transmission line, there results in the following expression on the air-side

$$\frac{C_a}{L_a} + \frac{C_{as}}{L_{as}} + \frac{C_0}{L_0} = 0 \tag{3.23}$$

where C_a and L_a are the capacitance and inductance of the air, C_{as} and L_{as} are the capacitance and inductance between the interface of the air and the substrate, and C_0 and L_0 are the capacitance and inductance of free-space, respectively. Consequently, on the substrate side of the transmission line,

$$\frac{C_s}{L_s} + \frac{C_{as}}{L_{as}} + \frac{C_0}{L_0} = 0, \tag{3.24}$$

where C_S and L_s are the capacitance and inductance of the dielectric substrate. Since $\gamma^2 = \omega^2 LC$ for a lossless line, Eqs. (3.23) and (3.24) are accordingly multiplied through by $\omega^2 L^2$, yielding

$$\omega^2 C_a L_a + \omega^2 C_{as} L_{as} + \omega^2 C_0 L_0 = 0, \tag{3.25}$$

and

$$\omega^2 C_s L_s + \omega^2 C_{as} L_{as} + \omega^2 C_0 L_0 = 0, \tag{3.26}$$

which are the desired forms appropriate for the lossless propagation factor $\gamma^2 = \omega^2 LC$.

Application of this definition of the propagation factor on a lossless line results in an expressions for the sum of the propagation factors on the air-side, given by

$$\gamma_a^2 + \gamma_{as}^2 + k_0^2 = 0, \tag{3.27}$$

and the sum of propagation factors on the substrate-side

$$\gamma_s^2 + \gamma_{as}^2 + \epsilon_s k_0^2 = 0. \tag{3.28}$$

Here γ_a is the propagation factor in air, γ_s is the propagation factor in the substrate, γ_{as} is the propagation factor at the air-dielectric interface, and $k_0 = \omega/c$ is the wavenumber in free space.

The generic form of the input impedance of a transmission line, which may be found in many undergraduate texts [60], may be written as

$$Z_{in} = Z_0 \frac{Z_L + Z_0 \tanh(\gamma l)}{Z_0 + Z_L \tanh(\gamma l)}. \tag{3.29}$$

For a lossless transmission line, the load impedance vanishes ($Z_L = 0$), and the input impedance of a lossless line becomes

$$Z_{in} = Z_0 \tanh(\gamma l). \tag{3.30}$$

Substitution of this expression for the input impedance of a lossless transmission line into Eq. (3.22) yields the result

$$Z_a \tanh(\gamma_a a') + Z_s \tanh(\gamma_s s) = 0. \tag{3.31}$$

In the LSE model, the characteristic impedances Z_a and Z_s are directly proportional to the propagation factor and inversely proportional to the heights of each line. Therefore $Z_a = \gamma_a/b'$ and $Z_s = \gamma_s/b$, and Eq. (3.31) becomes

$$\frac{\gamma_a}{b'} \tanh \gamma_a a' + \frac{\gamma_s}{b} \tanh \gamma_s s = 0, \tag{3.32}$$

where γ_a and γ_s are the propagation factors of the air-filled and substrate regions respectively. The quantities b, b', and s are geometrical parameters associated with

the single microstrip LSE model, as indicated in Fig. 3.4.

The MacLauren Series approximation of the hyperbolic tangent function [77] is now used in order to simplify the analysis, where

$$\tanh x \approx \frac{1}{1/x + x/3}, \quad |x| < \frac{\pi}{2} \tag{3.33}$$

With this substitution, Eq. (3.32) becomes

$$\frac{\gamma_a}{b'}\left(\frac{1}{1/\gamma_a a' + \gamma_a a'/3}\right) + \frac{\gamma_s}{b}\left(\frac{1}{1/\gamma_s s + \gamma_s s/3}\right) = 0, \tag{3.34}$$

which may be simplified to

$$\frac{\gamma_a}{b'}\left(\frac{3\gamma_a a'}{3 + \gamma_a^2 a'^2}\right) + \frac{\gamma_s}{b}\left(\frac{3\gamma_s s}{3 + \gamma_s^2 s^2}\right) = 0. \tag{3.35}$$

and on to the expression

$$\gamma_a^2 a'(3b + b\gamma_s^2 s^2) + \gamma_s^2 s(3b' + b'\gamma_a^2 a'^2) = 0. \tag{3.36}$$

which may be rearranged into the form

$$3(\gamma_a^2 a' b + \gamma_s^2 s b') + \gamma_a^2 \gamma_s^2 a' s(bs + b'a') = 0. \tag{3.37}$$

The second term of the above expression is next moved to the right-hand side of the equation, and with a common denominator established, this expression finally becomes

$$\frac{b/s}{\gamma_s^2} + \frac{b'/a'}{\gamma_a^2} = -\frac{sb + b'a'}{3}, \tag{3.38}$$

in agreement with Eq. (10) of Getsinger's original derivation [26].

Next, Getsinger [26] establishes a relationship between the propagation factor and effective dielectric constant of the microstrip transmission line. For a generic transmission line, the complex propagation factor is expressed as $\gamma = \alpha + j\beta$, where α is the attenuation factor and β is the dispersive term of the propagation factor. In the case of a lossless dispersive transmission line, $\alpha = 0$ so that $\gamma = j\beta$ and consequently

$$\gamma^2 = -\beta^2. \tag{3.39}$$

The dispersive propagation factor of the microstrip transmission line is directly proportional both to the free-space wavenumber $k_0 = \omega/c$ and the effective dielectric permittivity of the microstrip transmission line, as given by the expression $\beta^2 = k_0^2\epsilon_e$, so that

$$\gamma^2 = -k_0^2\epsilon_e. \tag{3.40}$$

Per Gestinger [26], the longitudinal propagation factor appearing in Eq. (3.40) is defined by both guided wave propagation in the air-filled region

$$\gamma_a^2 + \gamma^2 + k_0^2 = 0 \tag{3.41}$$

and in the dielectric substrate

$$\gamma_s^2 + \gamma^2 + \epsilon_s k_0^2 = 0, \tag{3.42}$$

where ϵ_s is the dielectric permittivity of the substrate.

With Eq. (3.40), this pair of equations becomes

$$\gamma_a^2 = k_0^2(\epsilon_e - 1) \tag{3.43}$$

for the longitudinal propagation factor in terms of the effective dielectric permittivity for the air-filled and

$$\gamma_s^2 = -k_0^2(\epsilon_s - \epsilon_e). \tag{3.44}$$

dielectric substrate regions, respectively. Finally, substitution of Eqs. (3.43) and (3.44) into Eq. (3.38) results in Getsinger's [26] expression for the basic dispersion relationship, given by

$$-\frac{b'/a'}{\epsilon_e - 1} + \frac{b/s}{\epsilon_s - \epsilon_e} = \frac{a'b' + sb}{3} k_0^2. \tag{3.45}$$

The relationship between the actual microstrip width parameters a and b and the parameters a' and b' appearing Getsinger's LSE model is simply

$$b'/a' = b/a. \tag{3.46}$$

With this substitution, one obtains the final expression for the basic dispersion relationship as

$$\frac{-1/a}{\epsilon_e - 1} + \frac{1/s}{\epsilon_s - \epsilon_e} = \left(\frac{a(b'/b)^2 + s}{3}\right) k_0^2. \tag{3.47}$$

Based upon the basic dispersion relationship given in Eq. (3.47), an expression for ϵ_e can noe be derived. Upon following Getsinger's approach [26] Eq. (3.47) may be expressed as a quadratic equation with the difference $(\epsilon_s - \epsilon_e)$ as the dependent

variable, given by

$$(\epsilon_s - \epsilon_e)^2 + \left[(\epsilon_s - 1) + \frac{(a+s)/as}{Ak_0^2}\right](\epsilon_s - \epsilon_e) + \frac{(\epsilon_s - 1)/s}{Ak_0^2} = 0, \tag{3.48}$$

with $A = [a(b'/b)^2 + s]/3$. This quadratic equation in admits the solution

$$\epsilon_s - \epsilon_e = \frac{B}{2}\left[1 - \sqrt{1 - \frac{(\epsilon_s - 1)/s}{B^2 Ak_0^2}}\right], \tag{3.49}$$

where $B = (\epsilon_s - 1) + (a+s)/asAk_0^2$. Upon substituting the first two terms of a Taylor Series expansion of the square root quantity appearing in this equation, there results

$$\epsilon_s - \epsilon_e \simeq \frac{(\epsilon_s - 1)/s}{BAk_0^2}, \tag{3.50}$$

which provides a good approximation when $\epsilon_0 - 1 \ll B^2 Ask_0^2$. Finally, upon substitution of the expressions for A and B into this equation, one finally obtains, Getsinger's [26] expression for the effective dielectric constant ϵ_e as

$$\epsilon_e = \epsilon_s - \frac{[(\epsilon_s - 1)a]/(a+s)}{1 + k_0^2 as\{[a(b'/b)^2 + s]/3\}(\epsilon_s - 1)/(a+s)}. \tag{3.51}$$

However, there still remains the unknown quantities a and s in Eq. (3.51) that arise from the geometry used in the LSE model. These can be determined by equating Eqs. (3.11) and (3.16) to Eq. (3.19). First, upon equating the equations for the per unit inductance,

$$\frac{Z_0\sqrt{\epsilon_{e0}}}{\eta_0} = \frac{1}{2\left[(a'/b') + (s/b)\right]}, \tag{3.52}$$

so that

$$\frac{\eta_0}{Z_0\sqrt{\epsilon_{e0}}} = 2\left[(a'/b') + (s/b)\right]. \tag{3.53}$$

This equation may then be rearranged to give an expression for a'/b', where

$$\frac{a'}{b'} = \frac{\eta_0}{2Z_0\epsilon e0} - \frac{s}{b}. \tag{3.54}$$

An expression for s/b must now be determined in order to fully determine the ratio a'/b'. This is found by equating Eq. (3.11) to Eq. (3.19), whence,

$$\frac{\eta_0\sqrt{\epsilon_{e0}}}{Z_0} = 2\left(\frac{a'}{b'} + \epsilon_s\frac{s}{b}\right). \tag{3.55}$$

Consequently,

$$\frac{s}{b} = \frac{\eta_0\sqrt{\epsilon_{e0}}}{2\epsilon_s Z_0} - \frac{a'}{\epsilon_s b'}. \tag{3.56}$$

With this result, Eq. (3.56) gives

$$\frac{a'}{b'} = \frac{\eta_0}{2Z_0\sqrt{\epsilon_{e0}}} - \frac{\eta_0\sqrt{\epsilon + e0}}{2\epsilon_s Z_0} + \frac{a'}{\epsilon_s b'}. \tag{3.57}$$

so that

$$\frac{a'}{b'}\left(\frac{\epsilon_s - 1}{\epsilon_s}\right) = \frac{\eta_0}{2Z_0\sqrt{\epsilon_{e0}}} - \frac{\eta_0\sqrt{\epsilon + e0}}{2\epsilon_s Z_0}. \tag{3.58}$$

which may be rewritten as

$$\frac{a'}{b'}\left(\frac{\epsilon_s - 1}{\epsilon_s}\right) = \frac{\eta_0}{2Z_0\sqrt{\epsilon_{e0}}}\left(\frac{\epsilon_s - \epsilon_{e0}}{\epsilon_s}\right). \tag{3.59}$$

This then gives an expression for a'/b' that is in agreement with Eq. (4a) of Getsinger [26];

viz.

$$\frac{a'}{b'} = \left(\frac{\eta_0}{2Z_0\sqrt{\epsilon_{e0}}}\right)\left(\frac{\epsilon_s - \epsilon_{e0}}{\epsilon_s - 1}\right). \tag{3.60}$$

This solution for a'/b' can now be used to determine an expression for s/b. Upon returning to Eq. (3.52), an expression for s/b in terms of a'/b' results, where

$$\frac{s}{b} = \frac{\eta_0}{2Z_0\sqrt{\epsilon_{e0}}} - \frac{a'}{b'}. \tag{3.61}$$

Upon substitution of the expression for a'/b' given in Eq. (3.60), there results

$$\frac{s}{b} = \frac{\eta_0}{2Z_0\sqrt{\epsilon_{e0}}} - \left[\left(\frac{\eta_0}{2Z_0\sqrt{\epsilon_{e0}}}\right)\left(\frac{\epsilon_s - \epsilon_{e0}}{\epsilon_s - 1}\right)\right], \tag{3.62}$$

which may be simplified to read

$$\frac{s}{b} = \frac{\eta_0}{2Z_0\sqrt{\epsilon_{e0}}}\left(1 - \frac{\epsilon_s - \epsilon_{e0}}{\epsilon_s - 1}\right). \tag{3.63}$$

This then provides an expression for s/b that is in agreement with Eq. (4b) of Getsinger [26], namely,

$$\frac{s}{b} = \frac{\eta_0}{2Z_0\sqrt{\epsilon_{e0}}}\left(\frac{\epsilon_{e0} - 1}{\epsilon_s - 1}\right) \tag{3.64}$$

Equations (3.60) and (3.64) are then substituted into Eq. (3.51), in order to yield an expression for the the effective dielectric constant in terms of known quantities. First

$$a + s = \frac{b\eta_0}{2Z_0\sqrt{\epsilon_{e0}}}\frac{\epsilon_s - \epsilon_{e0}}{\epsilon_s - 1} + \frac{b\eta_0}{2Z_0\sqrt{\epsilon_{e0}}}\frac{\epsilon_{e0} - 1}{\epsilon_s - 1}, \tag{3.65}$$

and

$$as = \frac{b\eta_0[(\epsilon_s - \epsilon_{e0}) + (\epsilon_{e0} - 1)]}{2Z_0\sqrt{\epsilon_{e0}}(\epsilon_s - 1)}. \tag{3.66}$$

Upon substitution of these two relations in Eq. (3.51), there results

$$\epsilon_s = \frac{\epsilon_s - \epsilon_{e0}}{1 + C[(k_0^2 b^2 \eta_0^2)/(12 Z_0)]} \tag{3.67}$$

where C is a an expression defined both by the dielectric permittivites and the waveguide geometry as,

$$C = \frac{(\epsilon_s - \epsilon_{e0})(\epsilon_{e0} - 1)[(\epsilon_s - \epsilon_{e0})(b'/b)^2 + (\epsilon_{e0} - 1)]}{\epsilon_{e0}(\epsilon_s - 1)^2}, \tag{3.68}$$

The expressions $k_0 = \omega/c$ for the wavenumber in free space, $\eta_0 = \sqrt{\mu_0/\epsilon_0}$ for the intrinsic impedance of free space, and $c = 1/\sqrt{\epsilon_0 \mu_0}$ for the speed of light in a vacuum are substituted into Eq. (3.67) along with a term Getsinger [26] defines as the frequency parameter of the dispersion function

$$f_p = \frac{Z_0}{2\mu b}, \tag{3.69}$$

where $\mu = 31.92$ nH/in is the magnetic permeability of the non-magnetic substrate. This then yields dispersion of the single microstrip transmission line, taken here as

$$\epsilon_e = \frac{\epsilon_s - \epsilon_{e0}}{1 + G(f/f_p)^2}. \tag{3.70}$$

Here G is defined as an "empirical parameter that is introduced in order to simplify the microstrip dispersion function" [26], where

$$G = \frac{\pi^2}{12} \frac{(\epsilon_s - \epsilon_{e0})(\epsilon_{e0} - 1)[(\epsilon_s - \epsilon_{e0})(b'/b)^2 + (\epsilon_{e0} - 1)]}{\epsilon_{e0}(\epsilon_s - 1)^2}. \tag{3.71}$$

Equations (3.70) and (3.71) provide the desired relationship between the parameters b'/b, ϵ_s, ϵ_{e0} and the empirical parameter G and these ultimately lead to a determination of the effective dielectric constant ϵ_e of the substrate material.

As an example, illustrating the use of these relations, consider comparing two different microstrip models in order to observe the influence of the material parameters and geometry on G and ϵ_e. The first model is cited by Getsinger [26] and makes use of measurements obtained by Zysman and Varon [78]. The second model considered here was developed by Veghte and Balanis [2]. Both models use a common substrate material of alumina, for which $\epsilon_s \approx 10$. Table 3.1 provides a comparison of the substrate dielectric constant ϵ_s, effective dielectric constant at zero frequency ϵ_{e0}, the characteristic impedance Z_0, and the dispersive frequency parameter f_p using each model.

Model	ϵ_s	ϵ_{e0}	Z_0	f_p
Zysman & Varon [78]	9.7	6.5	50 Ω	15.56 GHz
Vehgte & Balanis [2]	10.2	7.51	28.6 Ω	8.96 GHz

Table 3.1: Comparison of material parameters of two different microstrip transmission line models containing alumina substrates.

As can be seen from Eq. (3.71), G is also dependent on the geometric parameter b'/b, which is the ratio of the height of the dielectric to that of the waveguide in Figure 3.4. Getsinger [26] provides a detailed analysis determining that $b'/b \approx 3$ and $G \approx 1$.

In order to observe the effects of the effective dielectric permittivity on the real part of the complex propagation factor, Equation (3.70) is applied to Veghte and Balanis's [2] expression for this frequency dependent variable. Equation (6) of Veghte and Balanis's published analysis [2], states that the frequnecy-dependent propaga-

tion factor is related to the effective dielectric permittivity according to the familiar relation

$$\beta(\omega) = \frac{\omega}{c}\sqrt{\epsilon_e(\omega)} \tag{3.72}$$

where c is the wave speed in a vacuum. Substitution of Eq. (3.70) into Eq. (3.72) then gives

$$\beta(\omega) = \frac{\omega}{c}\sqrt{\frac{\epsilon_s - \epsilon_{e0}}{1 + G(f/f_p)^2}}. \tag{3.73}$$

Consider next the complex propagation factor, defined as

$$\gamma(\omega) = \alpha(\omega) + j\beta(\omega) \tag{3.74}$$

where $\alpha(\omega)$ is the attenuation factor. Veghte and Balanis [2] assume a lossless transmission line in their analysis, in which case $\alpha(\omega) \approx 0$. Substitution of Eq. (3.73) into the expression for the lossless propagation factor, there results

$$\gamma(\omega) = j\left[\frac{\omega}{c}\sqrt{\frac{\epsilon_s - \epsilon_{e0}}{1 + G(f/f_p)^2}}\right]. \tag{3.75}$$

3.3 The Coupled Microstrip Line

Coupled microstrip models are similar to single microstrip models in their method of fabrication where, for the single microstrip, a conductive strip lies above a dielectric substrate. Instead of a single conductive element, in the couple microstrip case, there are two or more conductive elements that are in close proximity on the substrate. Current and voltage coupling will then occur between the conductive elements. Similar to the single microstrip, the effective dielectric permittivity ϵ_e is influenced by the

interaction of the air and substrate dielectric. In addition, the coupling effects of the multiple conductive elements also play a role by contributing an additional self- and mutual- capacitance to the effective circuit properties.

Garg and Bahl [14] consider a symmetrical coupled microstrip line with two conductive elements, as illustrated in Figure 3.5. The conductive elements hold a normalized width to height ratio W/h and are separated by a distance s. They sit upon a dielectric substrate of thickness b with a relative dielectric permittivity ϵ_r. Similar to the single microstrip line, the coupled microstrip is surrounded by air with a relative dielectric constant of taken here as being close to unity.

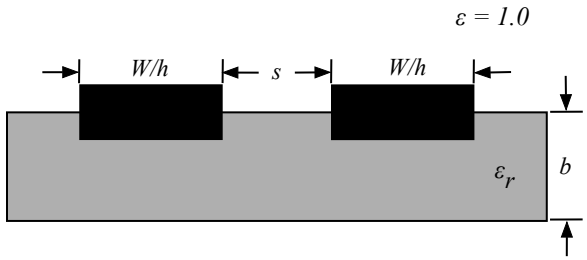

Figure 3.5: Cross-section of a coupled microstrip with two conductive strip lines with normalized width W/h, separation distance s between the two conductive strips, substrate thickness b, and substrate dielectric permittivity ϵ_r. The relative dielectric constant of the air surrounding the microstrip line is taken as $\epsilon = 1.0$.

In order to model the effects of the additional capacitance terms introduced by the coupling of the conductive strips, Garg and Bahl [14] apply the classical definition of the dielectric permittivity of a capacitor as given by $\epsilon = C/C_0$. Here C is the capacitance and C_0 is the capacitance of an ideal capacitor in vacuum.For this coupled microstrip geometry,

$$\epsilon_{re}^{i} = C_i/C_i^a. \tag{3.76}$$

Here, the subscript i indicates the even (e) or odd mode (o) and the superscript

a indicates that it is the capacitance of air as the dielectric material that is being referenced. In a symmetrical coupled microstrip line, the capacitance influences the inductance. Because of this, the capacitance is used to describe the coupling between the conductive strip lines.

Garg and Bahl [14] explain that two capacitance terms will arise in this configuration. One is the parallel plate capacitance that arises between the two lines and the other is the fringing capacitance of each line. The capacitance will differ for the even and odd modes of the microstrip lines, which act as waveguides. The total even-mode capacitance C_e, and odd-mode capacitance C_o, of a coupled microstrip line may be expressed as

$$C_e = C_p + C_f + C'_f, \tag{3.77}$$

$$C_o = C_p + C_f + C_{ga} + C_{gd}, \tag{3.78}$$

respectively. Here C_{ga} is the capacitance for the odd-mode for fringing across the gap in vacuum and C_{gd} is the capacitance across the gap in the dielectric substrate. In addition, C_p is the capacitance of a single microstrip of relative width to ground ratio W/h without fringing effects, and is given by the expression for a parallel plate capacitor as

$$C_p = \epsilon_0 \epsilon_r \frac{W}{h}, \tag{3.79}$$

where ϵ_0 is the dielectric permittivity of free space, and ϵ_r is the relative dielectric permittivity of the substrate. The quantity C_f is the fringing capacitance of a microstrip line of relative width to ground ratio W/h and free-space impedance Z_0, given by [14]

$$C_f = \frac{\sqrt{\epsilon_{re}}}{2cZ_0} - \frac{C_p}{2}, \tag{3.80}$$

where c is the speed of light in a vacuum. Finally, C'_f is the fringing capacitance of the coupled microstrip line with separation s between the microstrip lines, given by Garg and Bahl [14]

$$C'_f = \frac{C_f}{1 + A(h/s)\tanh(8s/h)}, \tag{3.81}$$

where A is an empirical factor that is based on the geometry and given as [14]

$$A = \exp\left[-0.1\exp\left(2.33 - 2.53W/h\right)\right]. \tag{3.82}$$

With these results, consider the expression for the even-mode capacitance C_e given in Equation (3.77). With the above expressions for C_p, C_f, C'_f substituted into that equation for C_e, one obtains

$$C_e = \frac{1}{2}\epsilon_0\epsilon_{re}\left[\frac{1}{\epsilon_0\sqrt{\epsilon_{re}}cZ_0} + \frac{W}{h} + \frac{1/\epsilon_0\sqrt{\epsilon_{re}}cZ_0 - W/h}{1 + A(h/s)\tanh 8s/h}\right]. \tag{3.83}$$

Because

$$\epsilon_0 cZ_0 = \sqrt{\frac{\epsilon_0}{\mu_0}}Z = \frac{Z}{Z_0}, \tag{3.84}$$

the expression for C_e becomes

$$C_e = \frac{1}{2}\epsilon_0\epsilon_{re}\left[\frac{Z_0/Z}{\sqrt{\epsilon_{re}}} + \frac{W}{h} + \frac{(Z_0/Z)\sqrt{\epsilon_{re}} - W/h}{1 + A(h/s)\tanh 8s/h}\right]. \tag{3.85}$$

In order to incorporate the effects of dispersion, Garg and Bahl [14] make use of Getsinger's [26] expression of the effective dielectric permittivity as given in Eq. (3.70)

for the even and odd mode as

$$\epsilon_{re}^{i}(f) = \epsilon_r - \frac{\epsilon_r - \epsilon_{re}^{i}}{1 + G(f/f)^2}, \tag{3.86}$$

where the superscript i denotes the even ($i = e$) or odd ($i = o$) mode, and the quantity G is related to the vacuum impedance Z_0 for the coupled microstrip.

Chapter 4

Numerical Analysis

4.1 Initial Voltage Pulse

The initial voltage pulse $v(t)$ on the transmission line considered here is taken as a single-cycle trapezoidal envelope modulated sine wave

$$v(t) = u(t)\sin(\omega_c t) \tag{4.1}$$

where $u(t)$ is the envelope of the pulse, and where ω_c is the fixed carrier frequency of the envelope modulated wave, which may differ depending upon the area of application of interest. Here, the carrier frequency can range from tens of Hz to GHz, where 50 - 60 Hz is typical for power systems, while the GHz range is more commonly used in communication networks or computer circuitry. Trapezoidal pulses are a more accurate model of digital clock pulses, which are often approximated as square pulses. Gaussian pulses are often chosen because they are infinitely smooth, thereby avoiding any singularities in their analysis; however, trapezoidal envelope pulses are considered

because of their general use in practical applications.

Fig. 4.1 illustrates an example of the temporal pulse behavior for a single cycle initial pulse with a fixed carrier frequency $f_c = 50$ Hz. At this carrier frequency, the period of the carrier wave is $T = 20$ms, and the rise t_r and fall t_f times are chosen to be equal as $t_r = t_f = 2$ms, making the pulse symmetrical. The amplitude over the main body of the envelope is unity. Although the trapezoidal envelope is continuous, their first derivative is discontinuous at both the leading and trailing edges.

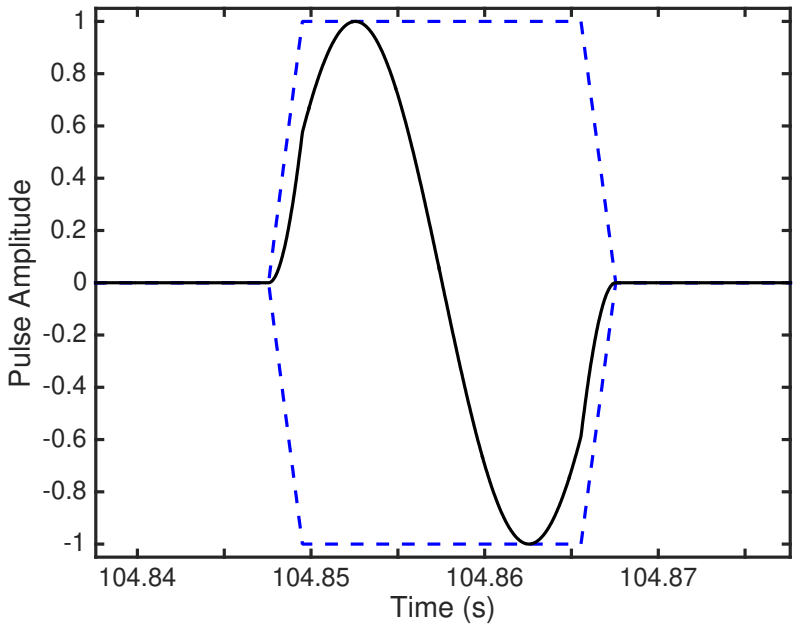

Figure 4.1: Single-cycle sine wave at $f_c = 50$ Hz with a trapezoidal pulse envelope with equal rise and fall times $t_r = t_f = 2ms$.

4.2 Temporal Spectrum of the Initial Voltage Pulse

The temporal spectrum representation of pulse propagation provides a straightforward method of analysis through the frequency characteristics of the initial pulse.With this in mind, the temporal spectrum representation of the trapezoidal envelope pulse is now considered.

The temporal spectrum is evaluated using the usual Fourier Transformation is taken here as

$$\tilde{F}(\omega) = \int_{-\infty}^{\infty} f(t) e^{j\omega t} dt \tag{4.2}$$

with the inverse Fourier Transform

$$f(t) = \frac{1}{2\pi} \int_{-\infty}^{\infty} \tilde{F}(\omega) e^{-j\omega t} d\omega. \tag{4.3}$$

With the initial voltage pulse given by $v(t) = u(t) \sin(\omega_c t)$, its Fourier Spectrum is given by

$$\tilde{V}(\omega) = \int_{-\infty}^{\infty} u(t) \sin(\omega_c t) e^{j\omega t} dt, \tag{4.4}$$

which may be rewritten as

$$\tilde{V}(\omega) = \frac{1}{2i} \int_{-\infty}^{\infty} u(t) \left(e^{j\omega_c t} - e^{-j\omega_c t} \right) e^{j\omega t} dt \tag{4.5}$$

using Euler's Identity. This then results in two separate transform integrals

$$\tilde{V}(\omega) = \frac{1}{2j}\int_{-\infty}^{\infty} u(t)e^{j(\omega+\omega_c)t}dt - \frac{1}{2j}\int_{-\infty}^{\infty} u(t)e^{j(\omega-\omega_c)t}dt. \tag{4.6}$$

From the frequency shift property of the Fourier Transform, one then obtains

$$\tilde{V}(\omega) = \frac{1}{2j}\left(\tilde{u}(\omega+\omega_c) - \tilde{u}(\omega-\omega_c)\right), \tag{4.7}$$

where

$$\tilde{u}(\omega) = \int_{-\infty}^{\infty} u(t)e^{j\omega t}d\omega \tag{4.8}$$

is the Fourier Transform of the pulse envelope function.

Consider next determining the Fourier Transform of the trapezoidal function envelope function $u(t)$. The analysis begins by defining the trapezoidal envelope as the difference between the initial rise-half of the signal envelope $u_r(t)$ and the fall-half of the signal $u_f(t)$. The rise-half is described by

$$u_r(t) = \begin{cases} (t-t_1)/t_r & t_1 \le t \le t_2 \\ 1 & t \ge t_2 \\ 0 & t \le t_1 \end{cases} \tag{4.9}$$

where $t_r = t_2 - t_1$ is the rise time of the leading edge envelope and is assumed to be

less than the period of the signal. The fall-half is described by

$$u_f(t) = \begin{cases} (t_4 - t)/t_f & t_3 \leq t \leq t_4 \\ 1 & t \leq t_3 \\ 0 & t \geq t_4 \end{cases} \tag{4.10}$$

where $t_f = t_4 - t_3$ is the fall time of the trailing edge of the envelope. For a symmetric pulse, the rise and the fall times are equal. The complete signal envelope function is then given by the difference $u(t) = u_r(t) - u_f(t)$.

The Fourier Transform of this envelope function is then given by the difference between the transforms of the rise and fall envelope function as

$$\tilde{U}(\omega) = \int_{-\infty}^{\infty} u(t) e^{j\omega t} dt = \int_{-\infty}^{\infty} u_r(t) e^{j\omega t} dt - \int_{-\infty}^{\infty} u_f(t) e^{j\omega t} dt, \tag{4.11}$$

where the individual Fourier Transforms of the rise and fall functions can be evaluated separately.

Consider first the rise-half with Eq. (4.9) is substituted into expression for the Fourier Transform, one obtains

$$\begin{aligned} \tilde{U}_r(\omega) =& \int_{-t_1}^{t_2} \frac{t - t_1}{t_r} e^{j\omega t} dt + \int_{t_2}^{\infty} e^{i\omega t} dt \\ =& \frac{1}{t_r} \int_{t_1}^{t_2} t e^{j\omega t} dt - \frac{t_1}{t_r} \int_{t_1}^{t_2} e^{j\omega t} dt + \int_{t_2}^{\infty} e^{j\omega t} dt \end{aligned} \tag{4.12}$$

Each of the three remaining integrals appearing in Eq. (4.12) are now evaluated

separately. The first integral is evaluated using integration by parts, as

$$\begin{aligned}\int_{t_1}^{t^2} te^{j\omega t}dt =& \frac{1}{j\omega}te^{j\omega t}|_{t_1}^{t_2} - \int_{t_1}^{t_2}\frac{1}{j\omega}e^{j\omega t}dt \\ =& \frac{1}{j\omega}\left(t_2e^{j\omega t_2} - t_1e^{j\omega t_1}\right) + \frac{1}{\omega^2}\left(e^{j\omega t_2} - e^{j\omega t_1}\right) \end{aligned} \tag{4.13}$$

With the substitution, $t_2 = t_1 + t_r$, this integral becomes

$$\int_{t_1}^{t_2} te^{i\omega t}dt = \frac{1}{j\omega}\left\{(t_1 + t_r)e^{j\omega(t_1+t_r)} - t_1e^{j\omega t_1}\right\} + \frac{1}{\omega^2}\left(e^{j\omega(t_1+t_r)} - e^{j\omega t_1}\right). \tag{4.14}$$

which, when rewritten using Euler's Identity, may be simplified to read

$$\int_{t_1}^{t_2} te^{j\omega t}dt = e^{j\omega(t_1+t_r/2)}\left\{\frac{1}{\omega}\left(2t_1\sin(\omega t_r/2) - it_re^{j\omega t_r/2}\right) + \frac{2j}{\omega^2}\sin(\omega t_r/2)\right\}. \tag{4.15}$$

For the second term in Eq. (4.12), one obtains

$$\begin{aligned}\int_{t_1}^{t_2} e^{j\omega t}dt &= \frac{1}{j\omega}\left(e^{j\omega t_2} - e^{j\omega t_1}\right) \\ &= \frac{1}{j\omega}\left(e^{j\omega(t_1+t_r)} - e^{j\omega t_1}\right) \\ &= \frac{1}{j\omega}e^{j\omega t_1}\left(e^{j\omega t_r} - 1\right) \end{aligned} \tag{4.16}$$

with the substitution $t_2 = t_1 + t_r$. One then has that

$$\begin{aligned}\int_{t_1}^{t_2} e^{j\omega t}dt &= \frac{1}{j\omega}e^{j\omega t_1}e^{j\omega t_r/2}\left(e^{j\omega t_r/2} - e^{-j\omega t_r/2}\right) \\ &= \frac{2}{\omega}\sin(\omega t_r/2)e^{j\omega(t_1+t_r/2)}. \end{aligned} \tag{4.17}$$

Finally, the third term in Eq. (4.12) is evaluated as

$$\begin{aligned}\int_{t_2}^{\infty} e^{j\omega t}dt &= \frac{j}{\omega}e^{j\omega t_2} \\ &= \frac{j}{\omega}e^{j\omega(t_1+t_r)}\end{aligned} \tag{4.18}$$

where $t_2 = t_1 + t_r$.

The temporal spectrum representation of the rise-half of the trapezoidal pulse is then given by the sum of each previously integrated term as

$$\begin{aligned}\tilde{U}_r(\omega) = \frac{1}{t_r}e^{j\omega(t_1+t_r/2)}\left\{\frac{1}{\omega}\left(2t_1\sin(\omega t_r/2) - jt_r e^{j\omega t_r/2}\right) + \frac{2j}{\omega^2}\sin(\omega t_r/2)\right\} \\ - \frac{t_1}{t_r}\frac{2}{\omega}\sin(\omega t_r/2)e^{j\omega(t_1+t_r/2)} + \frac{j}{\omega}e^{j\omega(t_1+t_r)},\end{aligned} \tag{4.19}$$

which may be simplified to the expression

$$\tilde{U}_r(\omega) = \frac{2j}{\omega^2 t_r}\sin(\omega t_r/2)e^{j\omega(t_1+t_r/2)}. \tag{4.20}$$

Notice that in the limit as t_r goes to zero and the trapezoidal front becomes a Heaviside step function, $\sin(\omega t_r/2)$ approaches $\omega t_r/2$, and $\lim_{t_r\to 0}\tilde{U}_r(\omega) = \frac{j}{\omega}e^{j\omega t_1}$, which is precisely the well-known expression for the Fourier Transform of the Heaviside step-function at $t = t_1$ [79]. Thus, the envelope spectrum given in Eq. (4.20) has the appropriate limiting behavior as the rise-time t_r approaches zero and the trapezoidal envelope function takes on the limiting form of a Heaviside unit-step function at $t = t_1$.

In a similar manner, the temporal spectrum of the fall-half of the envelope function

defined in Eq. (4.10), is given by

$$\begin{aligned}\tilde{U}_f(\omega) &= \int_{t_3}^{t_4} \frac{t_4 - t}{t_f} e^{j\omega t} dt + \int_{t_3}^{\infty} e^{j\omega t} dt \\ &= \frac{t_4}{t_f} \int_{t_3}^{t_4} e^{i\omega t} dt - \frac{1}{t_f} \int_{t_3}^{t_4} t e^{j\omega t} dt + \int_{t_3}^{\infty} e^{j\omega t} dt \end{aligned} \tag{4.21}$$

For the first term the first term appearing in Eq. (4.21), one obtains

$$\int_{t_3}^{t_4} e^{j\omega t} dt = \frac{1}{j\omega} \left(e^{j\omega t_4} - e^{j\omega t_3} \right), \tag{4.22}$$

which may be rewritten in terms of $t_f = t_4 - t_3$ as

$$\begin{aligned}\int_{t_3}^{t_4} e^{j\omega t} dt &= \frac{1}{j\omega} \left(e^{j\omega (t_f + t_3)} - e^{j\omega t_3} \right) \\ &= \frac{2}{\omega} e^{j\omega (t_3 + t_f/2)} \sin(\omega t_f/2). \end{aligned} \tag{4.23}$$

The Fourier transform integral appearing in the second term appearing in Eq. (4.21) may be evaluated using integration by parts as,

$$\begin{aligned}\int_{t_3}^{t_4} t e^{j\omega t} dt &= \left(\frac{t_4}{j\omega} e^{j\omega t_4} - \frac{t_3}{j\omega} e^{j\omega t_3} \right) + \frac{1}{\omega^2} \left(e^{j\omega t_4} - e^{j\omega t_3} \right) \\ &= \frac{1}{j\omega} \left[t_f e^{j\omega t_f} + t_3 \left(e^{j\omega t_f} - 1 \right) \right] + \frac{1}{\omega^2} e^{j\omega t_3} \left(e^{j\omega t_f} - 1 \right), \end{aligned} \tag{4.24}$$

where $t_4 = t_f + t_3$ has been substituted. Application of Euler's Identity then results in

$$\int_{t_3}^{t_4} t e^{j\omega t} dt = e^{j\omega (t_3 + t_f/2)} \left\{ \frac{1}{\omega} \left(2t_3 \sin(\omega t_f/2) - j t_f e^{j\omega t_f/2} \right) + \frac{2j}{\omega^2} \sin(\omega t_f/2) \right\}. \tag{4.25}$$

in a similar manner as was used in the derivation of Eq. (4.15).

Finally, the integral appearing in the third term is evaluated as

$$\begin{aligned}\int_{t_3}^{\infty} e^{j\omega t}dt &= \frac{j}{\omega}e^{j\omega t_3} \\ &= \frac{j}{\omega}e^{j\omega(t_f+t_3)}\end{aligned} \tag{4.26}$$

because $t_f = t_4 - t_3$.

The temporal spectrum for the fall-side of the trapezoidal envelope pulse is then given by the summation of these three terms as

$$\begin{aligned}\tilde{U}_f(\omega) = \frac{2t_4}{\omega t_f}e^{j\omega(t_3+t_f/2)}\sin(\omega t_f/2) \\ - \frac{1}{t_f}e^{i\omega(t_3+t_f/2)}\left\{\frac{1}{\omega}\left(2t_3\sin(\omega t_f/2) - it_f e^{j\omega t_f/2}\right)\right. \\ \left. + \frac{2j}{\omega^2}\sin(\omega t_f/2)\right\} + \frac{j}{\omega}e^{j\omega(t_f+t_3)}\end{aligned} \tag{4.27}$$

which may be simplified to read

$$\tilde{U}_f(\omega) = -\frac{2j}{\omega^2 t_f}\sin(\omega t_f/2)e^{j\omega(t_3+t_f/2)}, \tag{4.28}$$

a result that is very similar to that of the rise-half of the signal. Upon combining these results for the rise and fall time spectra for the complete trapezoidal pulse, one obtains

$$\tilde{U}(\omega) = \frac{2j}{\omega^2 t_r}\sin(\omega t_r/2)e^{j\omega(t_1+t_r/2)} - \frac{2j}{\omega^2 t_f}\sin(\omega t_f/2)e^{j\omega(t_3+t_f/2)}, \tag{4.29}$$

which simplifies to

$$\tilde{U}(\omega) = \frac{2j}{\omega^2}\left(\frac{1}{t_r}\sin(\omega t_r/2)e^{j\omega(t_1+t_r/2)} - \frac{1}{t_f}\sin(\omega t_f/2)e^{j\omega(T+t_1-t_f/2)}\right), \tag{4.30}$$

where $T = t_3 - t_2$ is the time period of the pulse. This result holds for either an asymmetric or symmetric pulse, depending on the rise and fall time values.

For the special case when the pulse is symmetric (i.e. when $t_r = t_f$) the envelope spectrum in Eq. (4.30) simplifies to

$$\tilde{U}(\omega) = \frac{4j}{\omega^2 t_r}\sin(\omega t_r/2)\sin(\omega(T-t_r)/2)e^{j\omega(t_1+T/2)}. \tag{4.31}$$

With this result, Eq (4.7) for the single-cycle trapezoidal envelope voltage pulse spectrum becomes

$$\begin{aligned}\tilde{V}(\omega) = &\frac{4j}{(\omega+\omega_c)^2 t_r}\sin((\omega+\omega_c)t_r/2)\sin((\omega+\omega_c)(T-t_r)/2)e^{j(\omega+\omega_c)(t_1+T/2)} \\ &-\frac{4j}{(\omega-\omega_c)^2 t_r}\sin((\omega-\omega_c)t_r/2)\sin((\omega-\omega_c)(T-t_r)/2)e^{j(\omega-\omega_c)(t_1+T/2)}.\end{aligned} \tag{4.32}$$

This analytical solution of the Fourier spectrum of the initial voltage pulse is compared with a numerical FFT result as illustrated in Fig. 4.2. The green curve in the figure illustrates the results of the numerical calculation of the specturm for the voltage pulse using the FFT algorithm. The dashed blue curve is the analytical Fourier spectrum of the initial voltage pulse in Eq. (4.33). It can be seen that the error between the analytical and numerical solutions is negligible, over the frequency domain of practical interest.

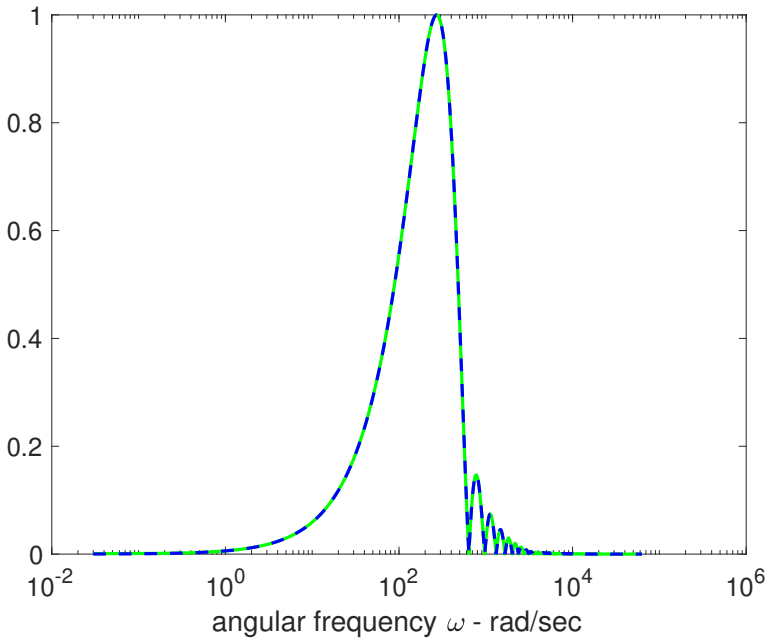

Figure 4.2: Fourier spectrum of single-cycle sine wave at $\omega_c = 50$ Hz with a trapezoidal envelope. The green line is the FFT of the pulse. The blue dashed line is analytical solution.

To further verify the accuracy of the FFT, the ratio of the rise and fall time of the envelope to period of the pulse t_r/T was varied and the Root-Mean-Square (RMS) error was calculated for each ratio value. The RMS error was again found to be negligible across the range of t_r/T values. Table 4.1 shows the change in RMS error across each chosen value of t_r/T.

		$\lvert\tilde{U}(0)\rvert$		$\lvert\tilde{U}(\omega_c)\rvert$	
t_r/T	RMS Error	Analytical	Numerical	Analytical	Numerical
0.0001	2.66e-15	0	5.44e-16	0.96	0.96
0.001	5.67e-09	0	5.44e-16	0.96	0.96
0.01	5.46e-11	0	5.49e-16	0.96	0.96
0.1	8.75e-11	0	9.80e-04	0.97	0.97
0.2	2.12e-08	0	-8.82e-14	0.92	0.92
0.3	1.17e-10	0	-1.36e-13	0.99	0.99
0.4	7.23e-11	0	3.33e-03	1.00	1.00
0.5	1.20e-10	0	-1.91e-13	1.00	1.00

Table 4.1: Analytical and numerical calculations of the pulse spectra for increasing values of t_r/T.

4.2.1 Low Frequency Effects

A more detailed analysis of the low frequency content of a pulse with a low frequency carrier wave is in order. When the carrier frequency of the pulse is sufficiently high such that the negative and positive frequency components of the pulse spectrum, $\tilde{u}(\omega - \omega_c)$ and $\tilde{u}(\omega + \omega_c)$, respectively, have negligible amplitudes in the opposite frequency domain (the negative frequency domain for the positive frequency component and vice-versa), one needs to account for these opposite frequency components in a numerical FFT calculation of the spectrum. However, when the signal frequency is sufficiently small, as would be for a 50 Hz voltage pulse, allowance for the opposite frequency components must be made in any numerical FFT calculation. Fig. 4.3 illustrates the overlap of the positive and negative frequency components for the case

of 50 Hz pulse.

From Fig. 4.3, it is clear that there is an impact on the overall pulse behavior because there is an overlap with the negative half of the frequency spectrum. The goal is to quantify that impact. Because the carrier frequency is low, at 50 Hz, there is going to be more of influence of the low frequency content than if the carrier frequency were higher. Another piece to be investigated is to determine at what frequency does the low frequency content become negligible.

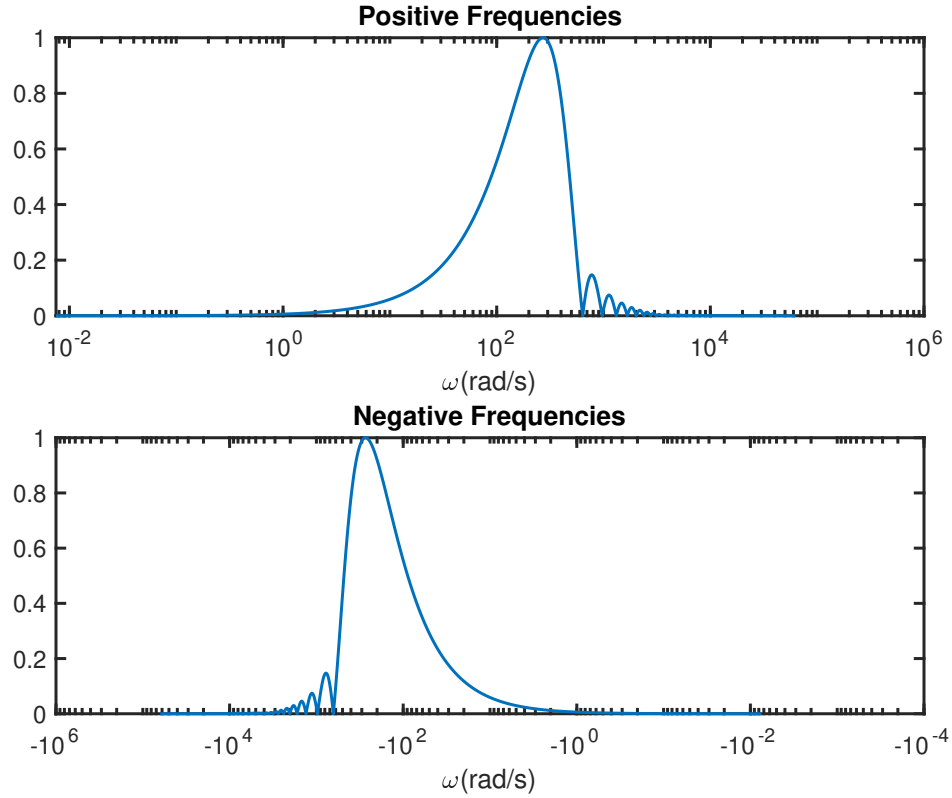

Figure 4.3: Fourier Spectrum of the single-cycle sine wave at f_c=50 Hz with a trapezoidal pulse over positive and negative frequencies. The top plot shows the positive-half of the pulse. The bottom plot shows the negative-half of the pulse. Note the overlap of the two halves of the pulse when $\omega \approx 0$.

4.3 Transmission Line Parameters

Recall the complex propagation factor in Eq. (2.9), $\gamma(\omega) = \alpha(\omega)+j\beta(\omega)$. As described in Section 2.2.1, the complex propagation factor $\gamma(\omega)$ is comprised of the attenuation factor $\alpha(\omega)$ and propagation factor $\beta(\omega)$ and describes the loss and phase behavior of the wave traveling along the transmission line. The attenuation and propagation factors are frequency dependent. Their frequency characteristics will impact the shape and time delay of the pulse propagation as frequency varies. An analysis of the attenuation and propagation factors with respect to frequency is performed for the coaxial cable and microstrip transmission line models described in Chapter **??**.

4.3.1 Coaxial Cable Parameters

Two coaxial cable examples are considered: (1) a high loss line and (2) a low loss line. Fig. 4.4 shows the dependence of frequency for the attenuation and propagation factors for both high and low loss coaxial cable transmission lines. The solid lines represent the high loss case, where $R_{high} = 100L$. The dashed lines are the low loss case, where

$$R_{low} = \frac{\sqrt{\omega_c \mu / 2\sigma_c}}{2\pi b(1 + b/a)}. \tag{4.33}$$

Table 4.2 shows the per unit circuit parameter values for the high and low loss cases. From this comparison, one can observe that the attenuation $\alpha(\omega)$ and propagation $\beta(\omega)$ constants on the high line is highly dependent on frequency. In particular, the lower frequency region shows much more variation in the behavior of $\alpha(\omega)$ and $\beta(\omega)$. This means that a wave propagating on a highly lossy transmission line will be more

	Low Loss	High Loss
R (Ω/m)	2.1651e-07	2.0794e-05
L (H/m)	2.0794e-07	2.0794e-07
G (S/m)	0.5439	0.5439
C (F/m)	1.6854e-10	1.6854e-10

Table 4.2: Per unit circuit parameter values of the high loss and low loss coaxial cable transmission lines.

susceptible to attenuation and dispersion in the lower frequency region. It can be seen in Fig. 4.4 there are some frequency regions that overlap where the line will behave as lossless or have extremely low loss. In this case, with the chosen per unit circuit parameters, the red "x" in Fig. 4.4 indicates the behavior of the attenuation and propagation factors at the carrier frequency of 50 Hz. At this frequency, Fig. 4.4 indicates that the pulse on the high loss line will propagate slightly slower and decay in amplitude in contrast to the pulse propagation on the low loss transmission line. In the kHz range and above, the attenuation and dispersion of both the high loss and low loss cases follow a linear behavior, which indicates that the high loss line will behave similarly to the the low loss line in the higher frequency regime.

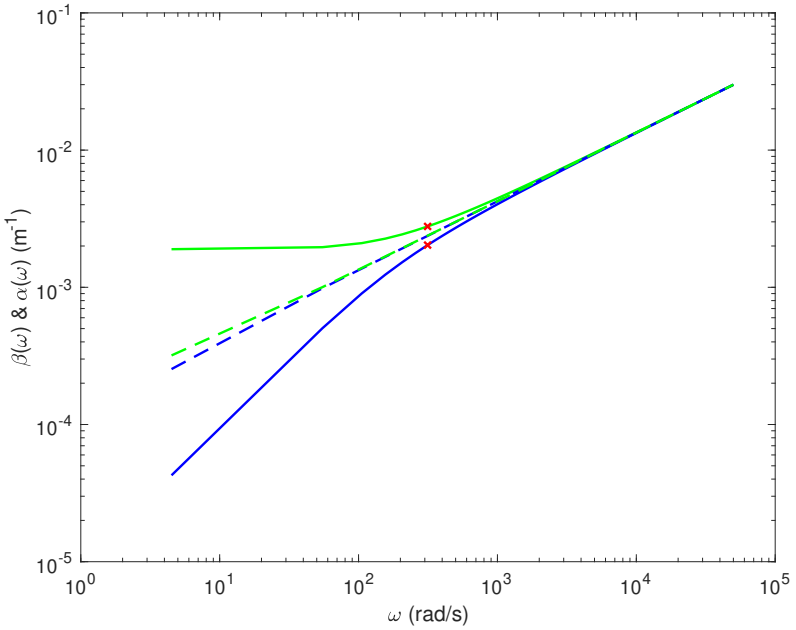

Figure 4.4: $\alpha(\omega)$ and $\beta(\omega)$ vs. ω for the high loss and low loss coaxial cable transmission line. The green lines are the attenuation constant $\alpha(\omega)$ and the blue lines are the propagation factor $\beta(\omega)$. The solid lines represent the high loss case and the dashed lines represent the low loss case. The red 'x' denotes the carrier frequency at $\omega_c = 314$ rad/s.

4.3.2 Microstrip Transmission Line Parameters

Two types of microstrip transmission lines models are compared in this section. One is the Getsinger model with a constant substrate permittivity ϵ_s, as described in Section 3.2. The other case is the dispersive, Debye-type substrate that is described in Appendix A. Fig. 4.6 illustrates the differences in the attenuation and dispersion between each model.

The complex propagation factor for a microstrip transmission line $\gamma_\mu(\omega)$ is written in terms of the relative effective dielectric permittivity $\epsilon_{reff}(\omega)$ of the transmission

line, as defined in Chapter 3, where

$$\gamma_\mu(\omega) = \alpha_\mu(\omega) + j\beta_\mu(\omega) = \frac{\omega}{c}\sqrt{\epsilon_{reff}(\omega)}. \tag{4.34}$$

Recall Eq. (3.70), which defines $\epsilon_{reff}(\omega)$ in terms of the dielectric permittivity of the substrate ϵ_s. Fig. A.1 illustrates the real and imaginary parts of ϵ_s for the case of a Debye-type substrate consisting of loamy soil with 0% moisture content. Note that both the real and imaginary parts of ϵ_s for this case are heavily dependent on frequency, which will result in the substrate attenuation factor $\alpha_s(\omega)$ and the substrate dispersion factor $\beta_s(\omega)$ to be dependent upon frequency as well. Such a behavior is illustrated in Fig. A.3. It can be seen from both Figs. A.1 and A.3 that for the case of the loamy soil with 0% moisture content, there will be a strong impact on the behavior of the pulse in the frequency range of 10^4 Hz to 10^6 Hz. When the carrier frequency of the pulse is within this range, it will be attenuated significantly and disperse slightly.

The effective dielectric permittivity $\epsilon_{reff}(\omega)$ for the Getsinger microstrip transmission line with a Debye-type substrate material exhibits the combined behavior of both the Getsinger model and Debye-type substrate. This behavior is illustrated in Fig. 4.5 where it can be seen that there are two regions of significant change in the dielectric permittivity. The first region from 10^4 Hz to 10^6 Hz is due to the Debye-type substrate and is identical to Fig. A.1 in that frequency range. The second region from 10^8 Hz to 10^{11} Hz is due to the resonance of the microstrip transmission line. This leads to the dispersive and attenuative behavior in Fig. 4.6.

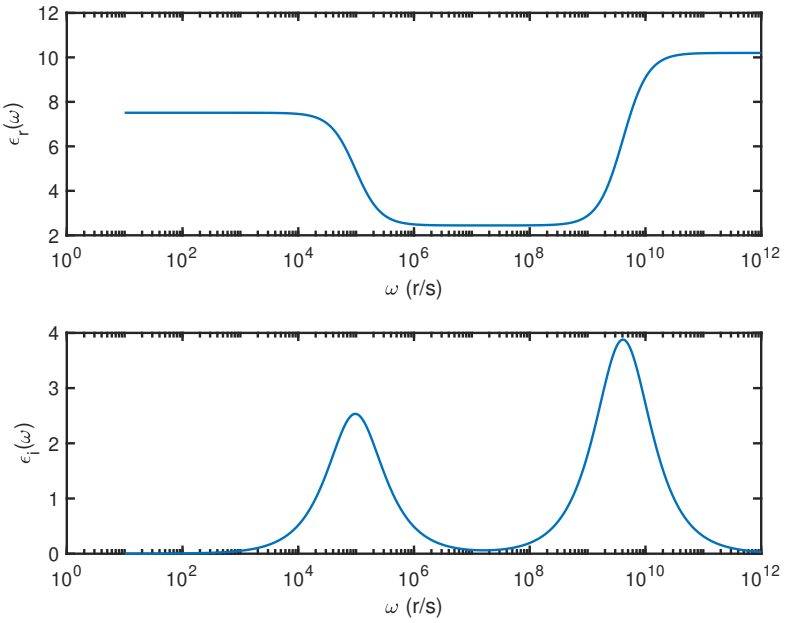

Figure 4.5: Real and Imaginary parts of the relative dielectric permittivity of the microstrip transmission line with a Debye-type dielectric substrate.

A strong dependence on frequency can be seen in the case of the microstrip with a Debye-type substrate, illustrated by the solid lines in Fig. 4.6. The constant substrate case behaves similarly to the low loss coaxial cable where $\alpha_\mu(\omega)$ and $\beta_\mu(\omega)$ are primarily linear with frequency. However, one noticeable difference from the coaxial cable is that $\gamma_\mu(\omega)$ is a function of $\epsilon_{reff}(\omega)$, which is limited by the maximum value of the substrate dielectric that is chosen with respect to infinite frequency, where $\epsilon_\infty = \epsilon(\omega_{max}) = 10.2$ is the value established in the Getsigner model. This limitation can be seen in Fig. 4.6 when $\alpha_\mu(\omega)$, illustrated by the dashed green line, reaches a constant value in the higher frequency range.

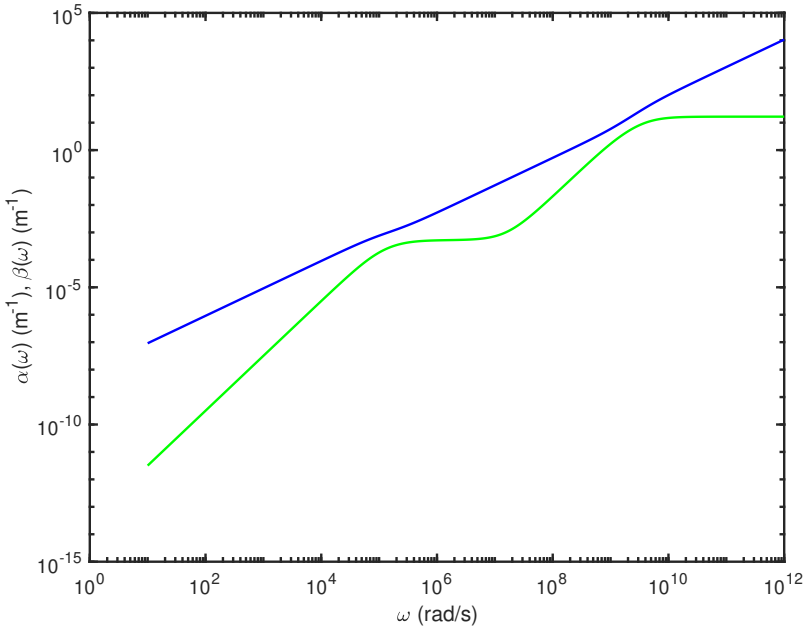

Figure 4.6: $\alpha(\omega)$ and $\beta(\omega)$ vs. ω for the microstrip transmission line model with a Debye-type substrate. The green line represents the attenuation constant $\alpha(\omega)$ and the blue line represents the propagation factor $\beta(\omega)$.

4.4 Numerical Pulse Propagation

The single-cycle sine wave with a trapezoidal envelope described in Eq. (4.1) was propagated numerically along the various types of transmission lines described in the previous section. The forward problem is considered here. First, the pulse was first propagated along lines of an infinite length. Reflection and transmission behavior of the voltage pulse across multiple interfaces or discontinuities is calculated here is as well.

As explained in Section 2.2.1, the initial voltage pulse is brought into phasor form in order to decouple the voltage from the current and concert the Kirchoff's Equation

to the Telegrapher's Equations. This is performed numerically through the use of Fast Fourier Transform (FFT) function. The green line in Fig. 4.2 shows the numerical spectrum of the initial voltage pulse, which was calculated by the FFT.

Calculation of Eq. (2.8a) reveals the pulse spectra at the end of the calculated propagation length. The pulse is calculated along the positive and negative frequency ranges to ensure symmetry. The propagated pulse was found by multiplying the initial pulse by the propagation factor over the specified distance. For this case, the specified distance is based upon the absorption depth, which is defined as the inverse of the attenuation factor, that is $z_d = 1/\alpha$ [41]. This calculation was performed for the low loss coaxial cable, the high loss coaxial cable, the Getsinger model microstrip transmission line with a constant dielectric substrate, and the microstrip transmission line with a Debye-type substrate.

4.4.1 Pulse Propagation on Coaxial Cable

The single-cycle sinusoidal voltage pulse with a trapezoidal envelope was propagated along a coaxial cable transmission line of infinite length. Two types of coaxial cables are considered. One is the high loss case and the other is the low loss case. Physical properties of each case are described in in Section 4.3.1. The goal here is to compare the pulse propagation behavior under high loss and low loss conditions.

The numerical sampling parameters for the coaxial cable models were taken at the Nyquist Rate with $N = 2^{22}$ samples, a maximum frequency of $f_{max} = 1 \times 10^4$ Hz and a sampling interval of $\Delta t = 1/(2f_{max})$. The size of the initial pulse envelope was determined by finding the limits of the time array, which were established by the numerical sampling parameters. The initial voltage pulse in the frequency domain

was then applied to the numerical Hemlholtz equations to propagate the pulse down the line. The length of the coaxial cable was set to one absorption depth of the line. Further absorption depth lengths could be considered.

Figs. 4.7a and 4.7b show the temporal frequency spectrum of the voltage pulse at the source and after propagation down the coaxial cable at 50 Hz and 5 Hz, respectively. Figs. 4.8a and 4.8b shows the pulse propagation in the time domain, through the application of the Inverse Fast Fourier Transform (IFFT) of the data in Figs. 4.7a and 4.7b. In both Figures, the green line is the initial pulse for both the high and low loss cables, the blue line shows the propagation on the low loss line, and the red line shows the propagation on the high loss line, propagated over a distance of one absorption depth.

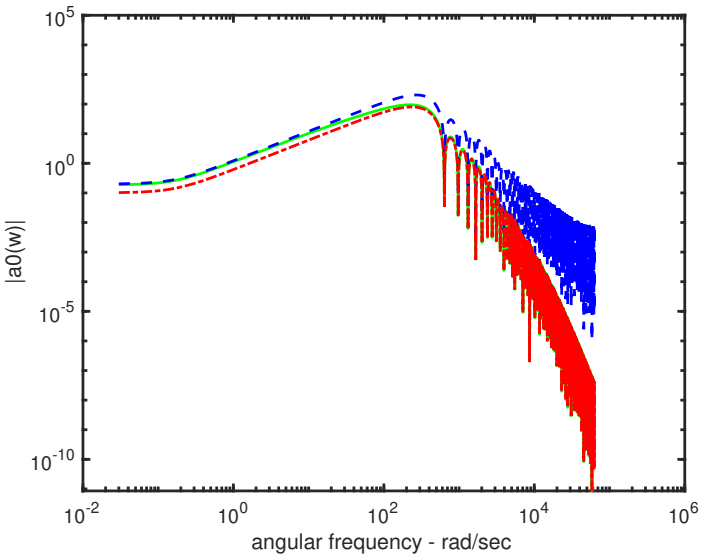

(a) Frequency Spectrum of the voltage pulse propagation on a coaxial cable of infinite length with a carrier frequency of 50 Hz.

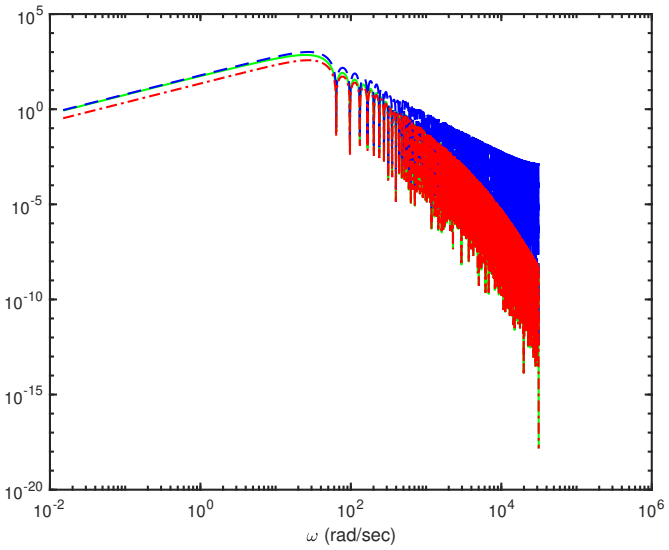

(b) Frequency Spectrum of the voltage pulse propagation on a coaxial cable of infinite length with a carrier frequency of 5 Hz.

Figure 4.7: Comparison of the frequency spectra of voltage pulse propagated on a coaxial cable with carrier frequencies of 50 Hz and 5 Hz. The green line is the spectrum of the initial voltage pulse. The blue represents the propagation of the pulse on a low loss line. The red line represents the propagation of the pulse on a high loss line.

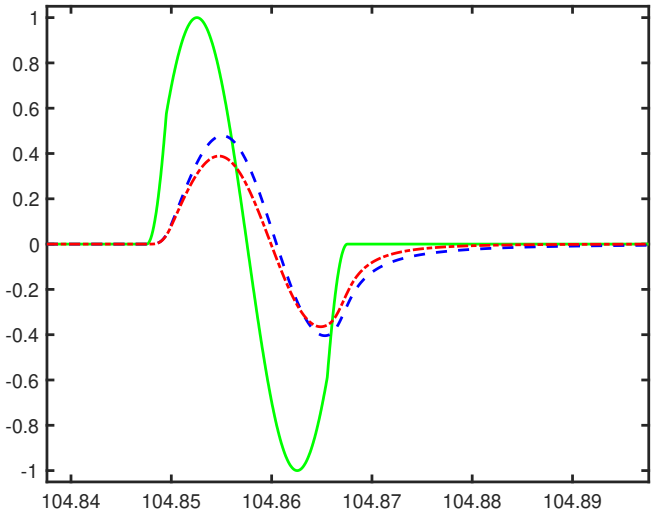

(a) Time domain representation of the voltage pulse propagation on a coaxial cable of infinite length with a carrier frequency of 50 Hz.

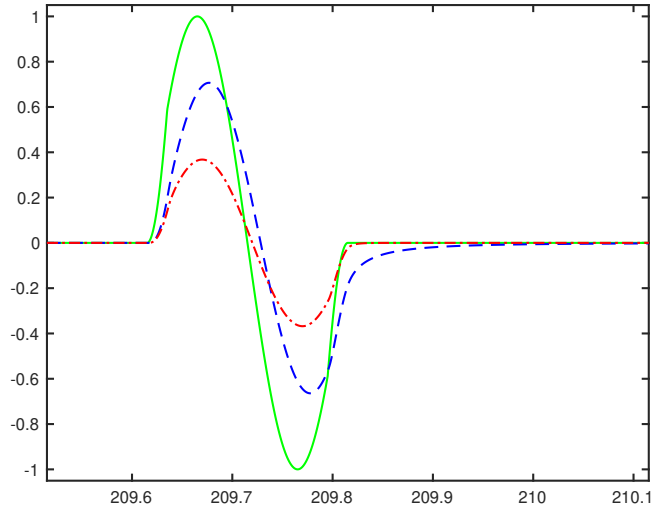

(b) Angular Spectrum of the voltage pulse propagation on a coaxial cable of infinite length with a carrier frequency of 5 Hz.

Figure 4.8: Time domain representation of the voltage pulse propagation on a coaxial cable of infinite length. The green line is the initial voltage pulse. The blue represents the propagation of the pulse on a low loss line. The red line represents the propagation of the pulse on a high loss line.

In both sets of figures of the frequency spectrum and the time domain representation, the effects of losses on the the coaxial cable are evident. There is a clear difference between initial pulse and the propagated pulses of each case. The effects of time delay, dispersion, and amplitude reduction are also shown. Such effects are more pronounced on the high loss case. Both cases show an over 50% decrease in time-domain amplitude from the initial voltage pulse. Therefore, it can be concluded that the losses and dispersion are contributing to the pulse behavior on the transmission line. Per Fig. 4.4, it is expected to have a minimal difference in the high and low loss at 50 Hz. It can be seen that even lower frequencies, such as 5 Hz, will be more impacted on the coaxial cables with the chosen parameters listed in Table 4.2.

Fig. 4.9 illustrates the different velocity calculations of the high and low loss coaxial cables. The behavior of the velocity follows what is described in Fig. 4.4. At the lower frequencies, there is a slight difference between the high and low loss cables, as indicated by the red 'x' and red 'o' points representing the the centrovelocity. As the frequency increases, the centrovelocity values are nearly identical. Additionally, the behavior of the velocity shown is consistent with the velocity discussion in Chapter 2. The group velocity, indicated by the dashed lines, departs significantly from the phase velocity in the higher frequency range. The centrovelocity values track closely to the group velocity, but remains in between the group and phase velocity. This is similar to the behavior described in Chapter 2 and further shows that the centrovelocity is an acceptable measure of velocity.

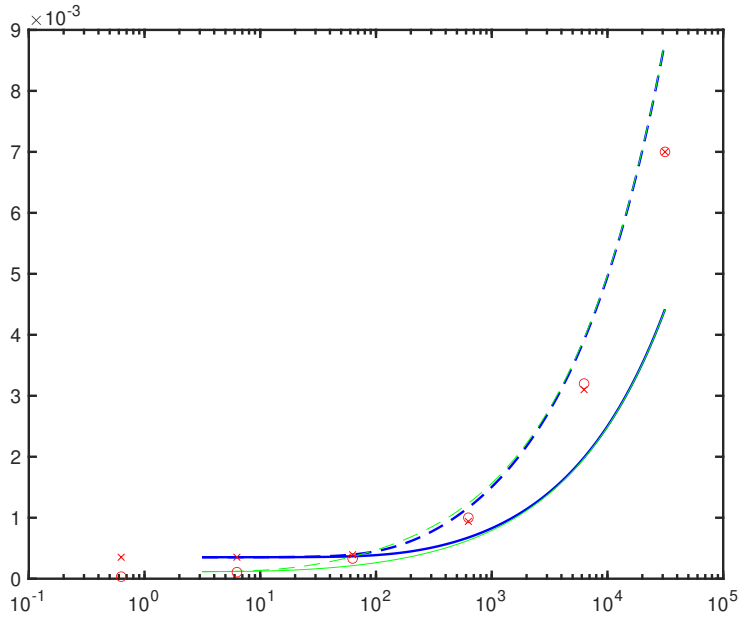

Figure 4.9: Phase Velocity (solid lines), group velocity (dashed lines), and centrovelocity (red points) for the high loss (blue lines and red 'x') and low loss (green lines and red 'o') coaxial cable.

4.4.2 Pulse Propagation on Lossless Microstrip Transmission Line

This initial analysis verifies that dispersive and lossy transmission lines do have a significant impact on the propagation of a voltage pulse. Hence, it is of interest to further investigate the effects of these losses for other transmission line geometries. In particular, two types of microstrip transmission lines are considered here: (1) the Getsinger model microstrip with a constant valued dielectric substrate and (2) the microstrip with a Debye-type dielectric substrate. The physical properties of each type of microstrip transmission line are described in Section 4.3.2.

First, the performance of the Getsigner model is verified through an attempt to recreate the results presented by Veghte and Balanis [2]. In order to do so, the numerical sampling parameters were taken at the Nyquist rate with $N = 2^{28}$, a maximum frequency of $f_{max} = 1 \times 10^{19}$ Hz and a sampling interval of $1/(2f_{max})$. The carrier frequency follows Veghte and Balanis's choice of a 10ps pulse [2]. Therefore, f_c =1 THz. The time array is defined by period T_c of the voltage pulse. However, in this case, the carrier is not included in the generation of the initial voltage pulse in order to observe the behavior of the envelope and easily compare results to Veghte and Balanis [2].

The size of the initial voltage pulse envelope was determined but finding the limits time array. From there, the Fast Fourier Transform (FFT) of the initial voltage pulse was taken to bring the initial pulse into the frequency domain. The temporal spectrum of the initial voltage pulse are then applied to the numerical Hemlholtz equations in order to propagate the pulse down the line.

For the Getsigner transmission line model, the length of the transmission line follows Veghte and Balanis's defined length of 0.354 inches [2]. The results for the propagated voltage pulse on the Getsinger transmission line model in the frequency domain and the time time domain are shown in Figs. 4.10 and 4.11 respectively. In both figures, the green line represents the initial pulse and the dashed blue line is the propagated pulse. Fig. 4.11 closely mirrors the results of Fig. 4 in the Vegthe and Balanis paper [2]. The role of dispersion is evident in the propagated pulse. As expected, there is no strong presence of losses because the transmission line is lossless. The sharp peaks the the leading and trailing edges Fig. 4.11 are also present in the results of Veghte and Balanis [2]. These peaks indicate the presence of the

Gibbs phenomenon and can occur as numerical artifact of the FFT. Ultimately, these results give confidence to the accuracy of the numerical propagation of the initial voltage pulse.

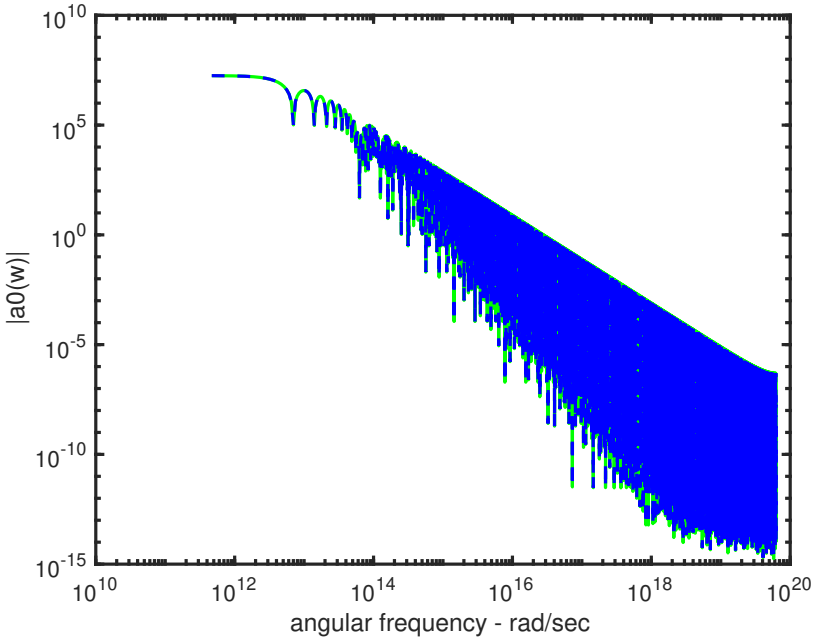

Figure 4.10: Temporal frequency spectrum of the Getsinger transmission line model. The green line is the spectrum of the initial pulse envelope with the carrier wave omitted. The blue is the spectrum of the propagated pulse envelope.

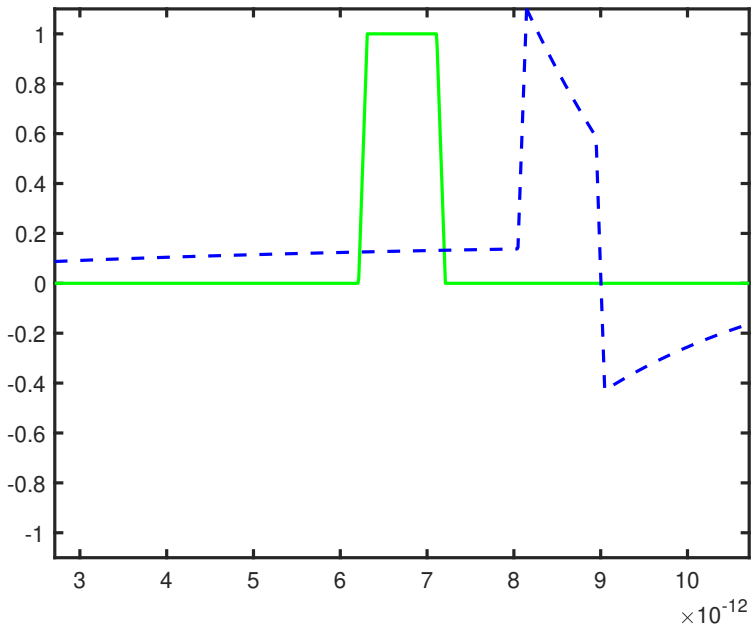

Figure 4.11: Time domain trapezoidal envelope pulse propagation of the Getsinger transmission line model. The green line is the spectrum of the initial envelope. The carrier wave is omitted. The blue line is the propagated pulse envelope. Results are similar to Fig. 4 of Veghte and Balanis [2].

The pulse velocity, group velocity, and centroid velocity of the trapezoidal envelope on the Getsinger transmission line model are illustrated in Fig. 4.12. Note that the centroid velocity values are close to the phase velocity values. This differs from what occurs with centroid velocity when the carrier wave is included in the pulse, which typically has values that are close to the group velocity. This is not surprising, however, as there is no underlying carrier. In such as case, the pulse velocity provides a more accurate representation of the velocity of the envelope propagation.

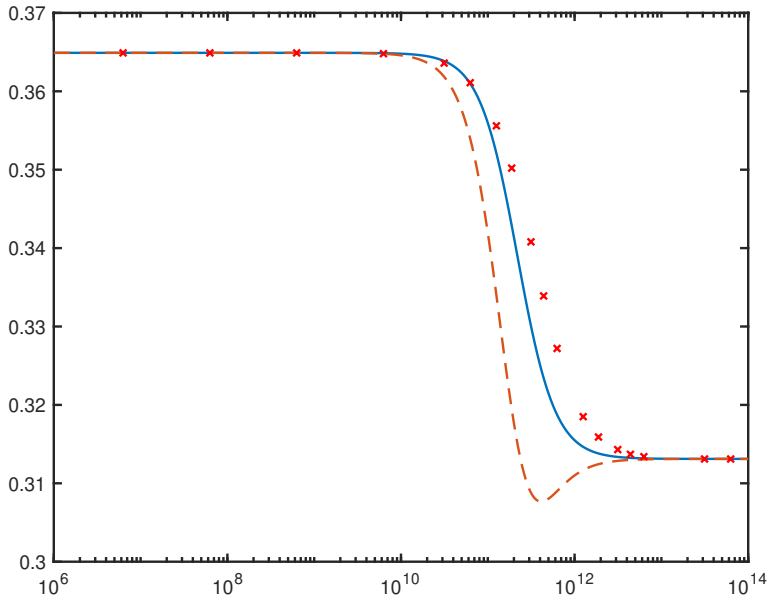

Figure 4.12: Velocity calculations of the trapezoidal envelope on the Getsigner transmission line mode. The blue line is phase velocity. The dashed orange line is the group velocity. The red 'x' points are centroid velocity.

Next, the carrier frequency of f_c =1 THz, as defined by Veghte and Balanis [2], is added back into the initial voltage pulse and the propagation is again performed on the Getsigner transmission line model. All numerical parameters remain the same as the propagation calculations without the carrier wave. The results for the propagated spectrum and time domain pulse with the carrier included are shown in Figs. 4.13 and 4.14 respectively. Similar to the previous figures, the green line is the initial pulse and the dashed blue line is the propagated. Although minimal, the evidence is dispersion can be seen on the trailing edge of the propagated pulse in Fig. 4.14. Loss is negligible, as expected, because the Gestinger transmission line model is lossless.

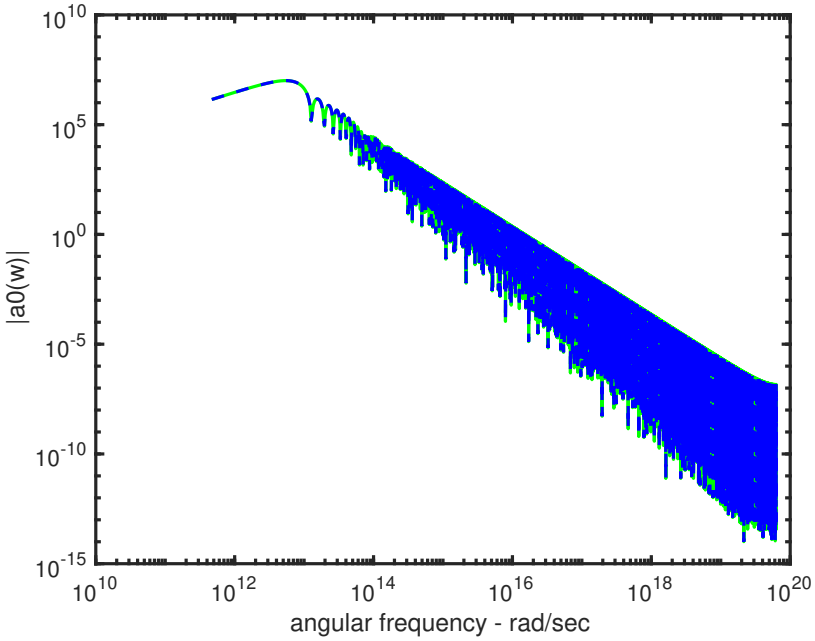

Figure 4.13: Temporal spectrum of the Getsinger transmission line model. The green line is the spectrum of the initial pulse envelope with carrier frequency of f_c =1 THz. The blue is the spectrum of the propagated pulse envelope.

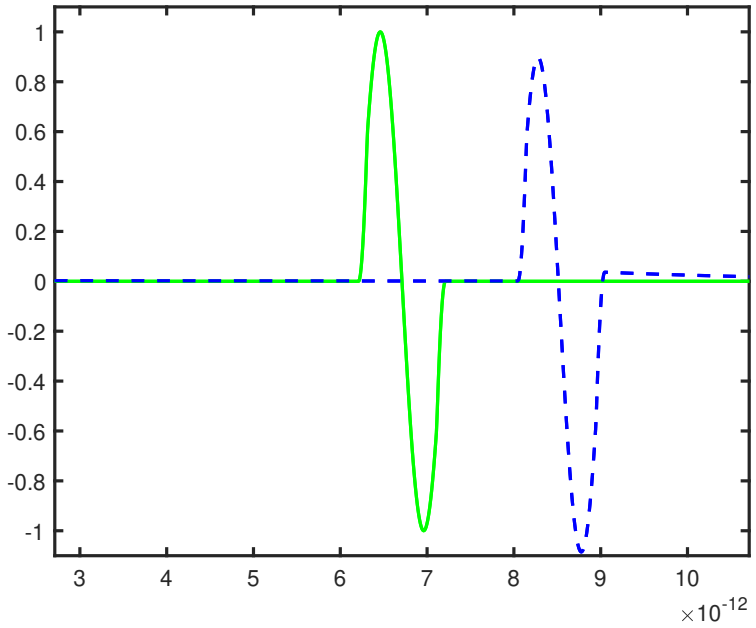

Figure 4.14: Time domain pulse of the Getsinger transmission line model. The green line is the initial pulse envelope with the carrier frequency of f_c =1 THz. The blue the propagated pulse envelope.

Fig. 4.15 illustrates the pulse velocity, group velocity, and centroid velocity of the trapezoidal envelope pulse on the Getsinger transmission line model. In this case, the centroid velocity values are close to the group velocity values. This is in contrast to Fig. 4.12, where the centroid velocity of the pulse without the carrier aligns more closely with the phase velocity.

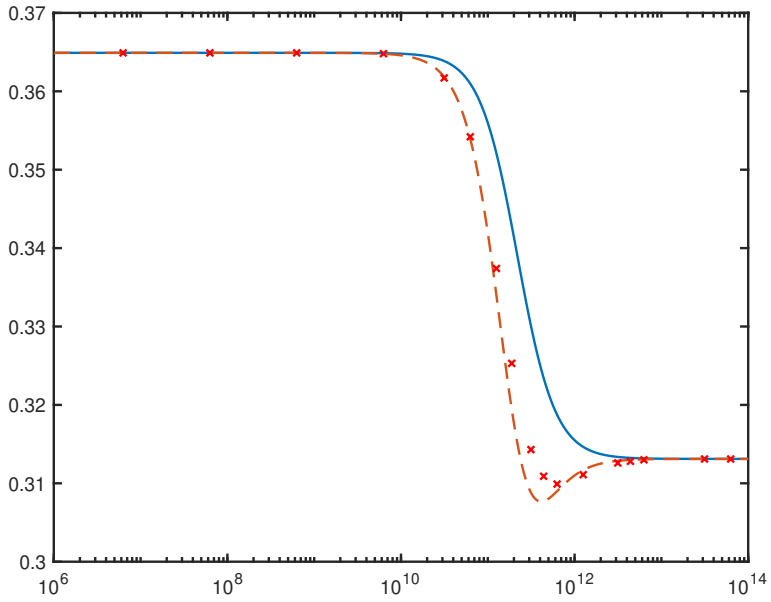

Figure 4.15: Velocity calculations of the trapezoidal envelope pulse with a 1 THz carrier wave on the Getsigner transmission line model. The blue line is phase velocity. The dashed orange line is the group velocity. The red 'x' points are centroid velocity.

4.4.3 Pulse Propagation on a Debye Microstrip Transmission Line

Finally, the microstrip transmission line with a Debye-type substrate is considered. Physical properties of this type of transmission line are described in Appendix A. Two different carrier frequencies were considered in order to observe the attenuative and dispersive effects in the frequency regions shown in Fig. 4.5. Figs. 4.16 - 4.19 show the propagated pulse spectrum and propagated time domain pulse, respectively, on the microstrip transmission line with the Debye-type dielectric substrate, with carrier frequencies of 2×10^4 Hz and 1×10^{11} Hz. The lossy nature of the transmission line

is particularly noticeable in Figs. 4.17 and 4.19, as there is nearly a 20% reduction from the initial pulse to the propagated pulse. Dispersion can also be seen through the smoothing or spreading effects at the leading and trailing edges of the propagated pulse. This behavior confirms what would be expected for propagation through a lossy and dispersive Debye-type medium.

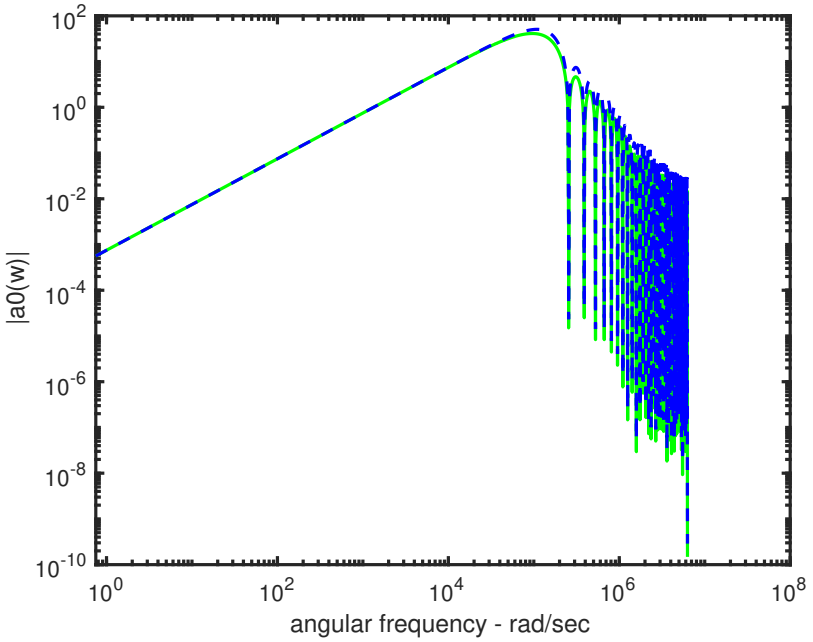

Figure 4.16: Temporal frequency spectrum of the Debye-type transmission line model. The green line is the spectrum of the initial pulse envelope with carrier frequency of f_c =20 kHz. The blue is the spectrum of the propagated pulse envelope.

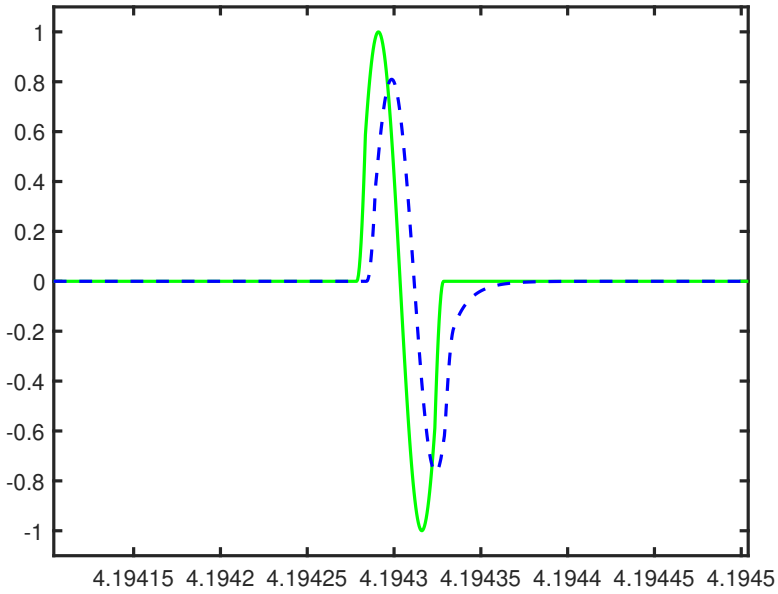

Figure 4.17: Time domain pulse of the Debye-type transmission line model. The solid green line is the initial pulse envelope with the carrier frequency of f_c =20 kHz. The dashed blue line is the propagated pulse envelope.

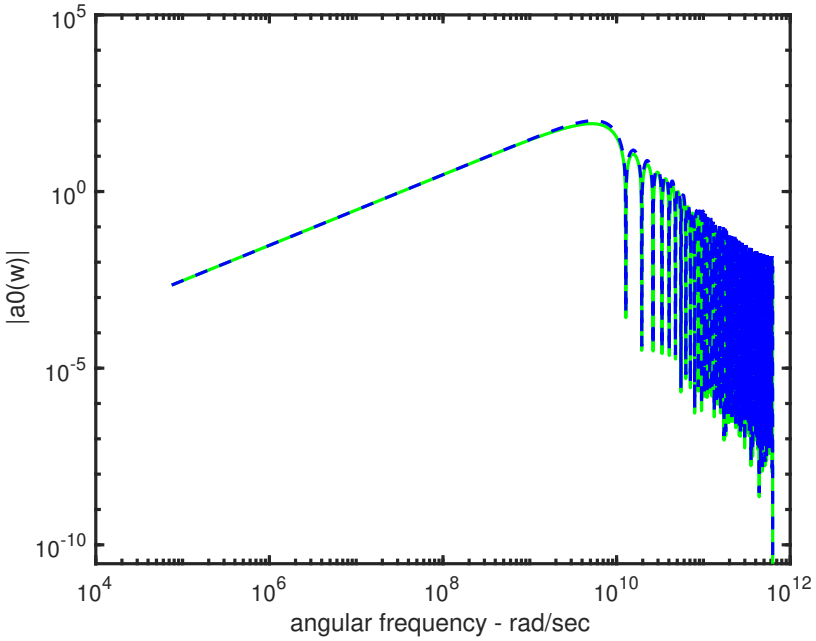

Figure 4.18: Temporal frequency spectrum of the Debye-type transmission line model. The solid green line is the spectrum of the initial pulse envelope with carrier frequency of f_c =1 GHz. The dashed blue line is the spectrum of the propagated pulse envelope.

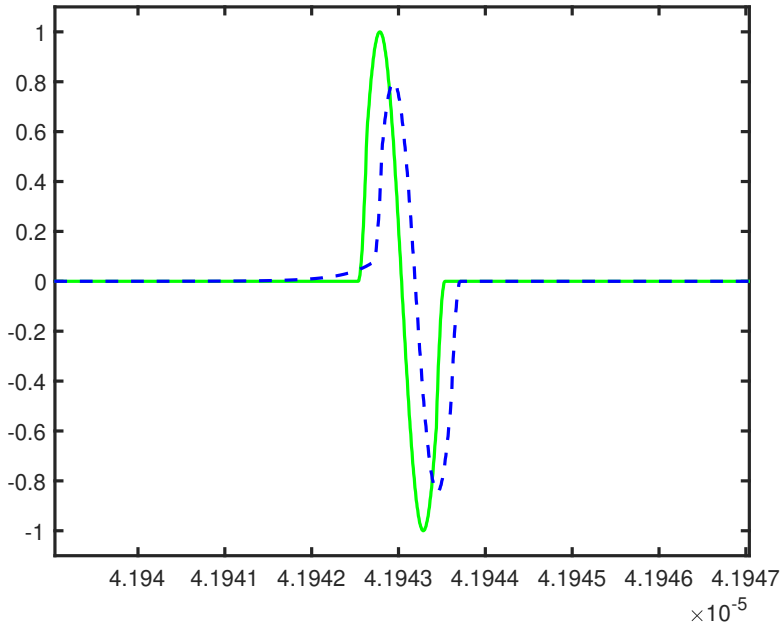

Figure 4.19: Time domain pulse of the Debye-type transmission line model. The sold green line is the initial pulse envelope with the carrier frequency of f_c =1 GHz. The dashed blue line is the propagated pulse envelope.

The velocity calculations for the pulse propagating on the microstrip transmission line containing a Debye-type substrate are found in Fig. 4.20. The pulse velocity, group velocity, and centroid velocity of the trapezoidal envelope pulse are illustrated. In this case, the centroid velocity lies between the pulse and group velocity values, which is similar to the case of the loamy soil material described in Appendix A. Notice the increasing behavior in the low-frequency range, which is similar to the velocity curve of the Debye material shown in Fig. 2.6. There is also a decrease in slope within the higher frequency range, which mimics the behavior in Fig. 4.12. This confirms the influence of both the Debye substrate material and entire microstrip transmission line.

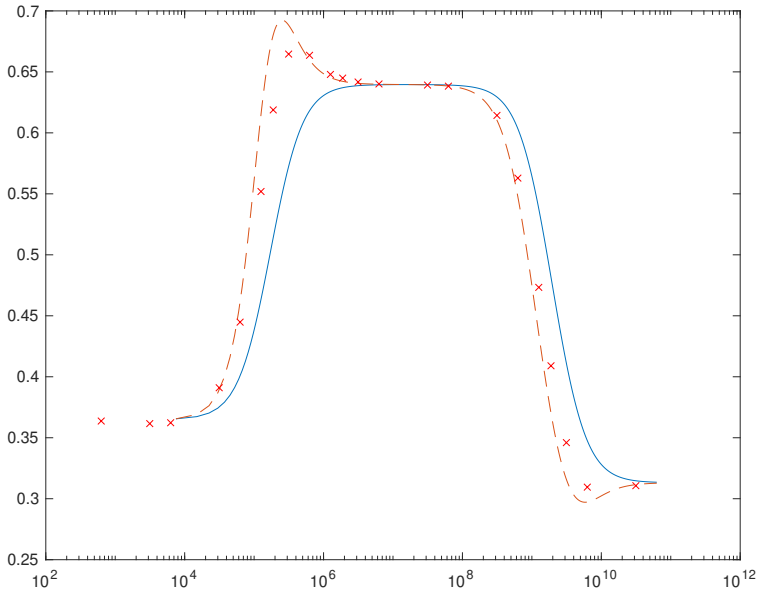

Figure 4.20: Velocity calculations of the trapezoidal envelope pulse on a microstrip transmission line containing a Debye-type substrate. The blue line is phase velocity. The dashed orange line is the group velocity. The red 'x' points are centroid velocity.

4.5 Summary

The results presented in this chapter show the voltage pulse propagation behavior of several different types of transmission lines, namely, the high and low loss coaxial cable, the lossless microstrip transmission line, and the lossy and dispersive transmission line. It is important to note that despite the various behaviors, all of these transmission line models are built upon the same distributive circuit model.

Now that the forward problem has been examined for several different cases, the inverse problem may be introduced in future research. Such an interface added to each transmission line represents changes in the media surrounding the transmission line.

Practical examples include stratified layers of moisture content in soil or a damage on a PCB trace. The propagated pulse will reflect back to the where the pulse was generated upon reaching the interface. From this reflected pulse, one can determine the location of the interface and the material changes that are present. The centroid velocity calculations are critical to accurately determine the location of any material changes that may occur around the transmission line.

Chapter 5

Conclusion and Future Work

5.1 Summary

Voltage pulse propagation on a variety of transmission lines was studied in this dissertation. Despite the long history of transmission line modeling and experimentation, as described in Chapter 1, the question of accuracy still remains. The work presented here attempted to improve the accuracy constraints of the literature in this area.

Three transmission line models were studied: (i) the coaxial cable, (ii) the single microstrip transmission line, and (iii) the coupled microstrip transmission line. The coaxial cable was first studied to provide confidence in the analysis and computation. The single microstrip was the main focus of this work and was chosen for its common use in a variety of applications, such as Time Domain Reflectometry (TDR). The coupled microstrip was also chosen for it common usage and was introduced analytically in Chapter 3. An extensive analytical description of each model was taken and the analysis of voltage pulse propagation on a generic transmission line was performed.

Following the analytical foundation, a numerical computation was performed to

observe the behavior of the pulse propagation on each transmission line in Chapter 4. The dispersive and attentuative properties of each transmission line was studied with respect to frequency. For the case of the microstrip transmission line, a lossless transmission line and a lossy, dispersive transmission line with a Debye-type substrate material were compared. The influnce of the Debye material can be seen in the results presented in Chatper 4.

As described in the literature presented in Chapters 1 and 2, the method of measurement considered for the pulse velocity has a significant impact upon accurately determining the distance of propagation and changes in surrounding material. The group velocity had been traditionally used when calculating distance of pulse propagation via time-of-flight methods. However, a different velocity measurement, which takes into account the energy centroid of the pulse and more accurately reflects how the pulse moves through a dispersive and attenuative medium. While the group velocity is a constant value of the wave packet velocity and does not change as the pulse moves further into the medium, the energy centrovelocity contradicts the notion that the pulse is propagating at a constant speed thought the medium. The energy centrovelocity indicates that pulse is actually slowing down as it propagates over increasing distance. Therefore there is a significant error between the group velcoity measurement and the energy centrovelocity measurement.

5.2 Conclusion

- Electromagnetic transients have been utilized to study propagation behavior through different media.

- A Debye-type dielectric material displays lossy and attenuative properties
- The energy centrovelocity provides promising results in regards to Time Domain Reflectometry (TDR) applications.
- The centrovelocity shows that the pulse decreases in speed as propagates through the medium.
- The use of the group velocity will be inaccurate if performing TDR in dispersive and attenuative materials and the centrovelocity may improve the accuracy.

5.3 Future Work

- The numerical analysis of the coupled microstrip should be performed and compared against the single microstrip to determine if the coupling effects of the conductors improve or reduce the accuracy TDR calculations in a dispersive and lossy media.
- The segmented transmission line analysis described in Chapter 2 can be extended for more layers. Complications lie in the unraveling of all the successive transmitted and reflected pulses.
- Following the analytical solution, numerical analysis of the pulse propagation in the multilayered media could be performed.
- Since the centrovelocity is directly measurable, an experiment can be performed to verify the numerical results obtained in this dissertation. There experiment could be performed in a few steps:

1. First, conduct measurements in a known material for a known distance and use the Debye-model to characterize the dielectric permittivity of that material. From there, a time-of-flight calculation can be used to calculate the velocity of the pulse if the distance and time of pulse propagation are measured.

2. This measurement with a known material and known distance can be repeated in different types of material. Debye models of the dielectric permittivity exist in the literature for a variety of materials. Examples for detecting moisture content could include sand, dry soil, or loamy soil.

3. Once data is gathered in known materials for a single distance, the process can be repeated again at different distances deeper in the material. If the numerical results hold, one should see a similar behavior in the slowing of the pulse velocity. Ideally, this should verify the use of the centrovelocity in contrast to the group velocity.

4. The experiment can then be performed again in different materials layered upon each other. More work on the numerical analysis should be done in order to predict the expected behavior in such layered media.

Bibliography

[1] M. Brown and R. Sedano, "Electricity transmission: A primer," tech. rep., National Council on Electricity Policy, 2004.

[2] R. Veghte and C. Balanis, "Dispersion of transient signals in microstrip transmission lines," *MTT-S International Microwave Symposium Digest*, vol. 34, no. 10, pp. 1427–1436, 1986.

[3] F. Chang, "Transient analysis of lossless coupled transmission lines in a nonhomogeneous dielectric medium," *IEEE Transactions on Microwave Theory and Techniques*, vol. 18, no. 9, pp. 616–626, 1970.

[4] K. Wong and W. Humpage, "Electromagnetic transient analysis in ehv power networks," *Proceedings of the IEEE*, vol. 70, no. 4, pp. 379–402, 1982.

[5] "C63.14-2014 - American National Standard Dictionary of Electromagnetic Compatibility (EMC) including Electromagnetic Environmental Effects (E3)," standard, IEEE Standards Association, Dec. 2014.

[6] H. Dommel and W. Meyer, "Computation of electromagnetic transients," *Proceedings of the IEEE*, vol. 62, no. 7, pp. 983–993, 1974.

[7] J. Davis and A. Annan, "Electromagnetic detection of soil moisture: Progress report imicrostrip dispersion model," *Canadian Journal of Remote Sensing*, vol. 3, no. 1, pp. 76–86, 1977.

[8] G. Topp, J. Davis, and A. Annan, "Electromagnetic determination of soil water content: Measurements in coaxial transmission lines," *Water Resources Research*, vol. 16, no. 3, pp. 547–582, 1980.

[9] S. He and S. Strom, "The electromagnetic inverse problem in the time domain for a dissipative slab and a point source using invariant imbedding: reconstruction of the permittivity and conductivity," *Journal of Computational and Applied Mathematics*, vol. 42, no. 1, pp. 137–155, 1992.

[10] T. Heimovaara, W. Bouten, and J. Verstraten, "Frequency domain analysis of time domain reflectometry waveforms, 2. a four-component complex dielectric mixing model for soils," *Water Resources Research*, vol. 30, no. 2, pp. 201–209, 1994.

[11] M. Smail, L. Pichon, M. Olivas, F. Auzanneau, and M. Lambert, "Detection of defects in wiring networks using time domain reflectometry," *IEEE Transactions on Magnetics*, vol. 46, no. 8, pp. 2998–3001, 2010.

[12] C. on Analytical Research Foundations for the Next-Generation Electric Grid; Board on Mathematical Sciences, T. A. D. on Engineering, and P. Sciences, *Analytical Research Foundations for the Next-Generation Electrical Grid*. 500 Fifth Street NW, Washington, DC 20001: National Academy of Sciences, 2016.

[13] "Transient protection of the smart grid: An ac power perspective." https://www.smartgrid.gov/document/transient_protection_smart_grid_ac_power_perspective. Accessed: 12-May-2017.

[14] R. Garg and I. Bahl, "Characteristics of coupled microstriplines," *IEEE Transactions on Microwave Theory and Techniques*, vol. 27, no. 7, pp. 700–705, 1979.

[15] C. Balanis, *Antenna Theory Analysis and Design, Third Edition*. Hoboken, New Jersey: John Wiley and Sons, Inc., 2005.

[16] W. Getsinger, "An introduction to microwave transmission lines," in *Proceedings of the 35th Midwest Symposium on Circuits and Systems*, 1992.

[17] M. Sondhi, "Model for wave propagation in a lossy vocal tract," *The Journal of the Acoustical Society of America*, vol. 55, pp. 1070–1075, 1974.

[18] D. Rasetshwane, S. T. Neely, J. Allen, and C. Shera, "Reflectance of acoustic horn and the solution of the inverse problem," *The Journal of the Acoustical Society of America*, vol. 131, no. 3, pp. 1863–1873, 2012.

[19] Q. Shi and O. Kanoun, "New algorithm for wire fault location using time-domain reflectometry," *IEEE Sensors Journal*, vol. 14, no. 4, pp. 1171–1178, 2014.

[20] L. Huakang, L. Kehong, J. Qiu, and G. Liu, "Analysis of time domain relfectometry crack intermittency crack detection in circuit board," in *2017 Prognostics and System Health Management Conference (PHM-Harbin)*, 2017.

[21] R. Cole, "Time domain reflectometry," *Annual Review of Physical Chemistry*, vol. 28, no. 1, pp. 283–300, 1977.

[22] Y. Shin, E. Powers, T. Choe, C. Hong, E. Song, J. Yook, and J. Park, "Application of time-frequency domain reflectometry for detection and localization of a fault on a coaxial cable," *IEEE Transactions on Instrumentation and Measurement*, vol. 54, no. 6, pp. 2493–2500, 2005.

[23] K. O'Connor and C. Dowding, *GeoMeasurements by Pulsing TDR Cables and Probes*. Boca Raton: CRC Press, 1999.

[24] F. Branin, "Transient analysis of lossless transmission lines," *Proceedings of the IEEE*, vol. 55, no. 11, pp. 2012–2013, 1967.

[25] L. Bewley, "Traveling waves on transmission systems," *Transactions of the American Institute of Electrical Engineers*, vol. 50, no. 2, pp. 532–550, 1931.

[26] W. Getsinger, "Microstrip dispersion model," *IEEE Transactions on Microwave Theory and Techniques*, vol. 21, no. 1, pp. 34–39, 1973.

[27] R. Greco, "Soil water content inverse profiling from single tdr waveforms," *Journal of Hydrology*, vol. 317, no. 3-4, pp. 325–339, 2006.

[28] A. Wood, "The cathode-ray oscillograph," *Journal of the Institution of Electrical Engineers*, vol. 63, no. 347, pp. 1046–1055, 1924.

[29] F. Bedell and H. Reich, "The oscilloscope: A stabilized cathode-ray: Oscillograph with linear time-axis," *Journal of the A.I.E.E.*, vol. 46, no. 6, pp. 563–567, 1927.

[30] L. Bergeron, *Du Coup de Belier en Hydraulique au Coup de Foundre en Electricité*. Paris: Dound, 1949.

[31] H. Dommel, "Digital computer solution of electromagnetic transients in single- and multiphase networks," *IEEE Transactions on Power Apparatus and Systems*, vol. 88, no. 4, pp. 388–399, 1969.

[32] E. Zachmanoglou and D. W. Thoe, *Introduction to partial differential equations with applications*. New York: Dover Publications, Inc., 1986.

[33] S. Grivet-Talocia, H. Huang, A. Ruehli, F. Canavero, and I. Elfadel, "Transient analysis of lossy transmission lines: An efficient approach based on the method of characteristics," *IEEE Transactions on Advanced Packaging*, vol. 27, no. 1, pp. 45–56, 2004.

[34] F. Chang, "Waveform relaxation analysis of rlcg transmission lines," *IEEE Transactions on Circuits and Systems*, vol. 37, no. 11, pp. 1397–1415, 1990.

[35] J. Mahseredjian, V. Dinavahi, and J. Martinez, "Simulation tools for electromagnetic transients in power systems: Overview and challenges," *IEEE Transactions on Power Delivery*, vol. 24, no. 3, pp. 1657–1669, 2009.

[36] H. Hazen, O. Schurig, and M. Gardner, "The m.i.t. network analyzer design and applications to power systems problems," *Transactions of the American Institute of Electrical Engineers*, vol. 49, no. 3, pp. 1102–1113, 1930.

[37] M. Hirakami and W. Neugebauer, "Transient network analyzer operation with digitial computer control and analysis," *IEEE Transactions on Power Apparatus and Systems*, vol. PAS-100, no. 4, pp. 1597–1607, 1981.

[38] R. Podmore, *Digital Computer Analysis of Power System Networks*. PhD thesis, University of Canterbury, Christchurch, New Zealand, 1972.

[39] J. Cooley and J. Tukey, "An algorithm for the machine calculation of complex fourier series," *Mathematics of Computation*, vol. 19, no. 90, pp. 297–297, 1965.

[40] S. Welaratna, "Thirty years of fft analyzers...," *Sound and Vibration Magazine: 30th Anniversary issue*, 1997.

[41] R. Chipman, *Schaum's outline of theory and problems of transmission lines*. New York: McGraw-Hill, 1968.

[42] O. Heaviside, "Improvements in electrical conductors, and in the arrangement and manner of using conductors for telephonic and telegraphic purposes." United Kingdom Patent No. 1407, 6 April 1880.

[43] W. Shockley, "The theory of p-n junctions in semiconductors and p-n junction transistors," *The Bell System Technical Journal*, vol. 28, no. 3, pp. 435–489, 1949.

[44] R. Mardiana and C. Q. Su, "Partial discharge location in power cables using a phase difference method," *IEEE Transactions on Dielectrics and Electrical Insulations*, vol. 17, no. 6, pp. 1731–1746, 2010.

[45] J. P. Steiner, P. H. Reynolds, and W. L. Weeks, "Estimating the location of partial discharges in cables," *IEEE Transactions on Electrical Insulation*, vol. 27, no. 1, pp. 44–59, 1992.

[46] F. H. Kreuger, M. G. Wezelenburg, A. G. Wiemer, and W. A. Sonneveld, "Partial discharge part xviii: Errors in the location of partial discharges in high voltage solid dielectrics cables," *IEEE Electrical Insulation Magazine*, vol. 9, no. 6, pp. 15–24, 1993.

[47] M. S. Mashikian, F. Palmeiri, R. Bansal, and R. B. Northrop, "Location of partial discharges in shielded cables in the presence of high noise," *IEEE Transactions on Electrical Insulation*, vol. 27, no. 1, pp. 37–43, 1992.

[48] T. A. Papadopoulos, Z. G. Datsios, A. I. Chrysochos, P. N. Mikropoulos, and G. K. Papagiannis, "Wave propagation characteristics and electromagnetic transient analysis of underground cable systems considering frequency-dependent soil properties," *IEEE Transactions on Electromagnetic Compatibility*, 2020.

[49] M. Wild, S. Tenbohlen, E. Gulski, R. Jongen, and F. de Vries, "Practical aspects of pd localization for long length power cables," in *2013 IEEE Electrical Insulation Conference (EIC)*, 02-05 June 2013.

[50] A. Rodrigo Mor, P. H. F. Morshuis, P. Llovera, V. Fuster, and A. Quijano, "Localization techniques of partial discharges at cable ends in off-line single-sided partial discharge cable measurements," *IEEE Transactions on Dielectrics and Electrical Insulation*, vol. 23, no. 1, pp. 428–434, 2016.

[51] I. Farhat, L. Farrugia, R. Persico, S. D'Amico, and C. Summat, "Preliminary experimental measurements of the dielectric and magnetic properties of a material with a coaxial tdr probe in reflection mode," *Progress In Electromagnetics Research M*, vol. 91, no. 1, pp. 111–121, 2020.

[52] G. Topp, M. Yanuka, W. Zebchuk, and S. Zegelin, "Determination of electrical conductivity using time domain reflectometry: Soil and water experiments in coaxial lines," *Water Resources Research*, vol. 24, no. 7, pp. 945–952, 1988.

[53] F. Dalton, W. Herkelrath, D. Rawlins, and J.D.Rhoades, "Time-domain reflectometry: Simultaneous measurement of soil water content and electrical conductivity with a single probe," *Science*, vol. 224, no. 4652, pp. 989–990, 1984.

[54] S. Zegelin, I. White, and D. Jenkins, "Improved field probes for soil water content and electrical conductivity measurements using time domain reflectometry," *Water Resources Research*, vol. 25, no. 11, pp. 2367–2376, 1989.

[55] W. Skierucha, "Accuracy of soil measurement by tdr technique," *International Agrophysics*, vol. 14, no. 4, pp. 417–426, 2000.

[56] A. Meriem, S. Achour, and G. Chafik, "Diagnostics and experiments on dielectric properties using time domain reflectometry (tdr)," in *2010 10th IEEE International Conference on Solid Dielectrics*, 04-09 July 2010.

[57] P. Neveux and A. Chambarel, "Debye modelisation for the soil moisture measurement in tdr," in *2006 IEEE Instrumentation and Measurement Technology Conference Proceedings*, 24-27 April 2006.

[58] M. Loewer, J. Igel, and N. Wagner, "Spectral decomposition of soil electrical and dielectric losses and prediction of in situ gpr performance," *IEEE Journal of Selected Topics in Applied Earth Observations and Remote Sensing*, vol. 9, no. 1, pp. 212–220, 2016.

[59] D. Cheng, *Field and wave electromagnetics*. Reading, Mass: Addison Wesley, 1985.

[60] G. Miner, *Lines and electromagnetic fields for engineers*. New York: Oxford University Press, 1996.

[61] Y. Ku, *Transient Circuit Analysis*. Princeton, New Jersey: D. Van Nostrand Company, 1961.

[62] R. L. Smith, "The velocities of light," *American Journal of Physics*, vol. 38, no. 8, pp. 978–984, 1970.

[63] D. Anderson, J. Askne, and M. Lisak, "Wave packets in an absorptive and strongly dispersive medium," *Physical Review A*, vol. 12, no. 4, pp. 1546–1552, 1975.

[64] M. Lisak, "Energy expressions and energy velocity for wave packets in an absorptive and dispersive medium," *Journal of Physics A: Mathematical and General*, vol. 9, no. 7, p. 1145, 1976.

[65] G. C. Sherman and K. E. Oughstun, "Energy-velocity description of pulse propagation in absorbing, dispersive dielectrics," *Journal of the Optical Society of America B*, vol. 12, no. 2, pp. 229–247, 1995.

[66] K. E. Oughstun and N. A. Cartwright, "Dispersive pulse dynamics and associated pulse velocity measures," *Journal of Optics A: Pure and Applied Optics*, vol. 4, no. 5, p. S125, 2002.

[67] L. Brillouin, *Wave Propagation and Group Velocity*. New York and London: Academic Press, 1960.

[68] J. W. S. Baron Rayleigh, *The Theory of Sound Volume I*. London: MacMillan and Co., 1877.

[69] P. J. W. Debye, *Polar Mechanics*. Dover Publications, Inc., 1929.

[70] R. E. Collin, *Field Theory of Guided Waves.* Piscataway, NJ: IEEE Press, 1990.

[71] F. M. Tesche, "Simple model for the line parameters of a lossy coaxial cable with a nondispersive dielectric," *IEEE Transactions on Electromagnetic Compatibility*, vol. 49, no. 1, pp. 12–17, 2007.

[72] S. Schelkunoff, "The electromagnetic theory of coaxial transmission lines and cylindrical shields," *The Bell System Technical Journal*, pp. 532–579, 1934.

[73] E. Hammerstad and O. Jensen, "Accurate models for microstrip computer-aided design," *1980 IEEE MTT-S International Microwave symposium Digest*, 1980.

[74] E. Yamashita, K. Atsuki, and T. Ueda, "An approximate dispersion formula of microstrip lines for computer-aided design of integrated circuits," *IEEE Transactions on Microwave Theory and Techniques*, vol. 27, no. 12, pp. 1036–1038, 1979.

[75] M. Steer, *Microwave and RF Design (Third Edition).* Raleigh, NC: NC State University, 2019.

[76] D. M. Pozar, *Microwave Engineering (Fourth Edition).* 111 River Street, Hoboken, NJ: John Wiley & Sons, Inc., 2012.

[77] M. R. Spiegel, S. Lipschutz, and J. Liu, *Schaum's Outlines: Mathematical Handbook of Formulas and Tables (Third Edition).* The McGraw-Hill Companies, Inc., 2009.

[78] G. Zysman and D. Varon, "Wave propagation in microstip transmission lines," *1969 G-MTT International Microwave Symposium*, 1969.

[79] Y. Shmaliy, *Continuous Time Signals.* The Netherlands: Springer, 2006.

[80] K. E. Oughstun, *Electromagnetic and Optical Pulse Propagation 2: Temporal Pulse Dynamics in Dispersive Attenuative Media.* New York, New York: Springer, 2009.

[81] P. Bhartia and P. Pramanick, "A new microstrip dispersion model," *IEEE Transactions on Microwave Theory and Techniques*, vol. 32, no. 10, pp. 1379 – 1384, 1984.

[82] K. Aho and K. E. Oughstun, "Voltage pulse propagation on a dispersive microstrip transmission line," in *2021 United States National Committee of URSI National Radio Science Meeting (USNC-URSI NRSM)*, 04-09 January 2021.

Appendix A

The Debye Model Description of Dielectric Dispersion

The Debye model of dielectric dispersion [69] begins with the relaxation equation

$$\frac{d\underset{\sim}{P}}{dt} + \frac{1}{\tau_m}\underset{\sim}{P}(\underset{\sim}{r}, t) = a\underset{\sim}{E}_{eff}(\underset{\sim}{r}, t) \tag{A.1}$$

where a is a constant in time and where τ_m is the relaxation time of the molecular dipole moment in the absence of an applied electromagnetic field, $\underset{\sim}{P}(\underset{\sim}{r}, t)$ is the molecular dipole moment, and $\underset{\sim}{E}_{eff}(\underset{\sim}{r}, t)$ is the effective electric field strength at the molecular position. The frequency domain solution of this equation followed by a spatial average over molecular sites leads to the expression [80]

$$\epsilon(\omega)/\epsilon_0 = \epsilon_\infty + \frac{\epsilon_s - \epsilon_\infty}{1 + j\omega\tau} \tag{A.2}$$

for the relative dielectric permittivity, where $\epsilon_s = \epsilon(0)/\epsilon_0$ describes the static ($\omega = 0$) relative permittivity, and ϵ_∞ describes the high-frequency limit of the relative per-

mittivity

$$\epsilon_\infty = \lim_{\omega >> 2\pi/\tau} \left(\frac{\epsilon(\omega)}{\epsilon_0} \right). \tag{A.3}$$

Because this model describes the rotational effects of the molecular dipole moment, it is a low-frequency model, valid provided that ω does not greatly exceed $2\pi/\tau$ and the electric effects begin to dominate. Because this typically occurs at infrared frequencies ($\omega \sim 10^{12}$rad/s), the model is entirely appropriate for the transmission line analysis presented in this dissertation.

The analysis presented here explicitly includes the influence of the dielectric material dispersion of the substrate on the effective permittivity of the single and coupled microstrip lines. Most of the published literature [2, 81] of microstrip transmission lines, including that of both Garg and Bahl [14] and Getsinger [26], treats the dielectric permittivity of the substrate as a constant, independent of the frequency content of a given signal. However, a realistic transmission line would be dispersive in both phase and attenuation.

Note that by making the model causal with a Debye-type substrate, the substrate dielectric permittivity becomes complex, with the real and imaginary parts

$$\epsilon_r(\omega)/\epsilon_0 = \Re\{\epsilon(\omega)/\epsilon_0\} = \epsilon_\infty + \frac{\epsilon_s - \epsilon_\infty}{1 + \tau^2\omega^2}, \tag{A.4a}$$

$$\epsilon_i(\omega)/\epsilon_0 = \Im\{\epsilon(\omega)/\epsilon_0\} = (\epsilon_s - \epsilon_\infty)\frac{\tau\omega}{1 + \tau^2\omega^2} \tag{A.4b}$$

forming a Hilbert Transform pair. Typical behavior of the real and imaginary parts of the relative dielectric permittivity are illustrated in Figure A.1 for a material of loamy soil with 0% moisture content.

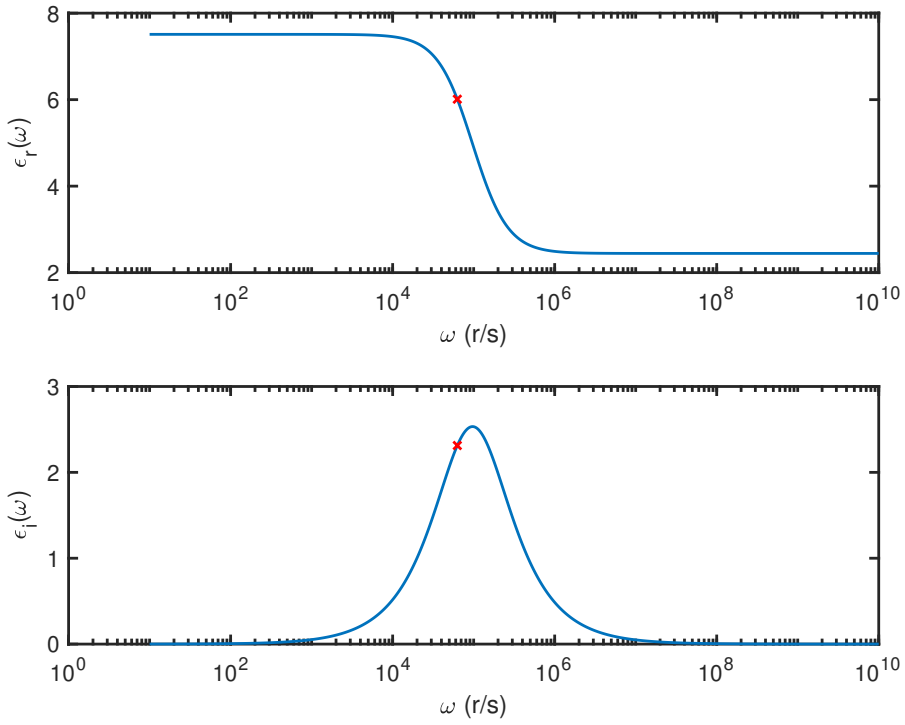

Figure A.1: Real and imaginary parts of the relative dielectric permittivity of the Debye model for loamy soil with 0% moisture content. The red 'x' indicates the carrier frequency $f_c = 10kHz$ of the pulse propagated through the Debye material.

Note that imaginary part $\epsilon_i(\omega)/\epsilon_0$, which is related to the absorption coefficient $\alpha_(\omega)$, nearly vanishes at $\omega = 0$ and also approaches zero as ω increases above $2\pi/\tau$ near where the peak value occurs. Furthermore, the real part ϵ_r/ϵ_0 is approximately constant for small values of ω and decreases rapidly for values of ω in the neighborhood about $2\pi/\tau$. This region is where the effects of frequency dispersion are significant when compared to the behavior either above or below this critical value of $2\pi/\tau$. Estimates of the model parameters $\epsilon_s, \epsilon_\infty$, and τ from observed pulse distortion should be sufficient to identify the substrate material. This is also shown though the complex relative impedance. The real and imaginary parts are plotted in Fig. A.2. Note

that the impedance will have an influence on the current pulse at the chosen carrier frequency.

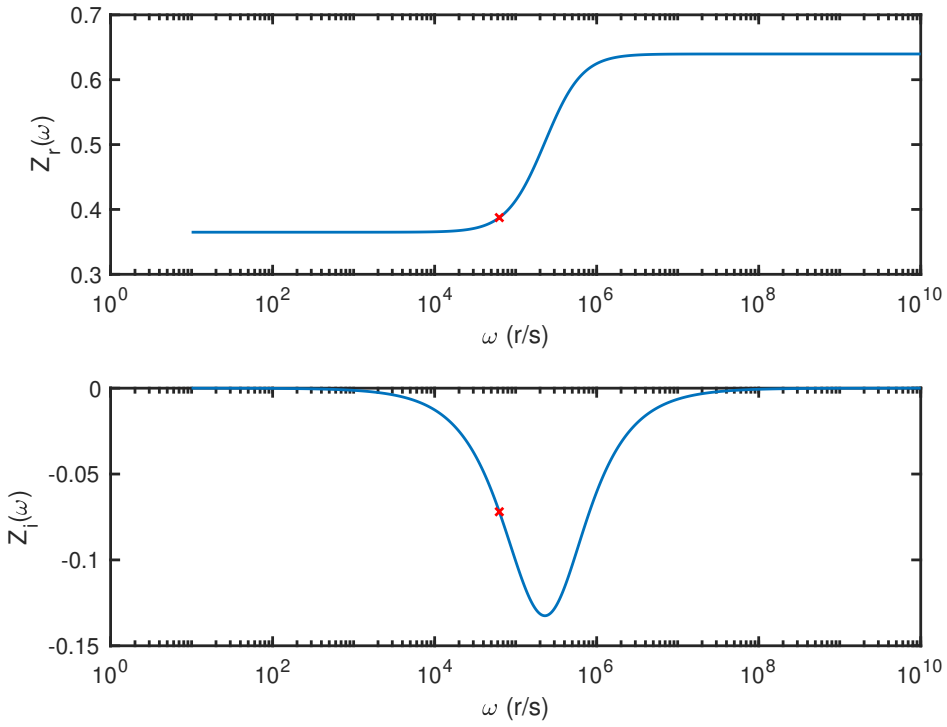

Figure A.2: Real and imaginary parts of the relative impedance of the Debye model for loamy soil with 0% moisture content. The red 'x' indicates the carrier frequency $f_c = 10kHz$ of the pulse propagated through the Debye material.

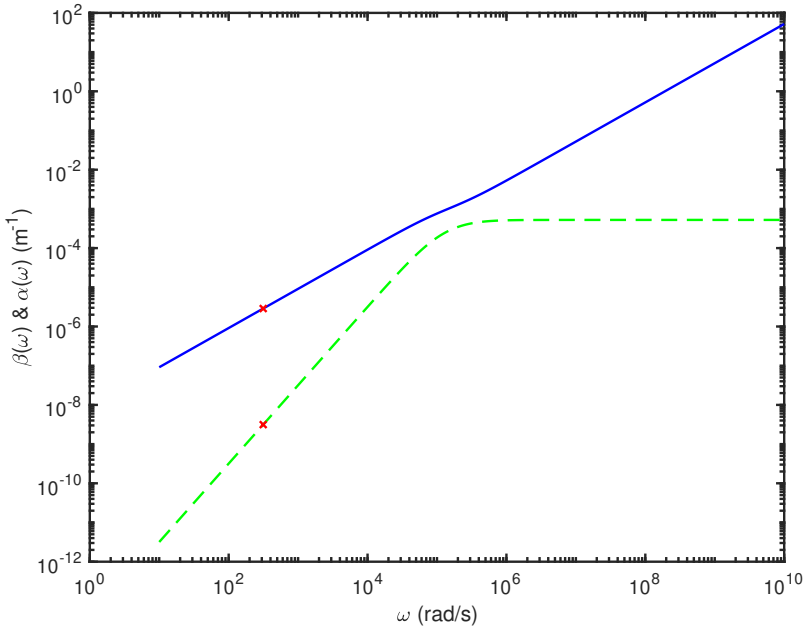

Figure A.3: Attenuation and dispersion of loamy soil with 0% moisture content. The sold blue line is the dispersion factor $\beta_s(\omega)$. The dashed green line is the attenuation factor $\alpha_s(\omega)$.

A single-cycle sine wave voltage pulse with carrier frequency $f_c = 10$ kHz was chosen to propagate through the Debye material. This value was chosen because it lies within the region that is most influences dispersion. Figs. A.4 and A.5 show the propagated voltage and current pulses. Note that due to the high impedance, the amplitude of the current pulse is significantly lower than the amplitude of the voltage pulse.

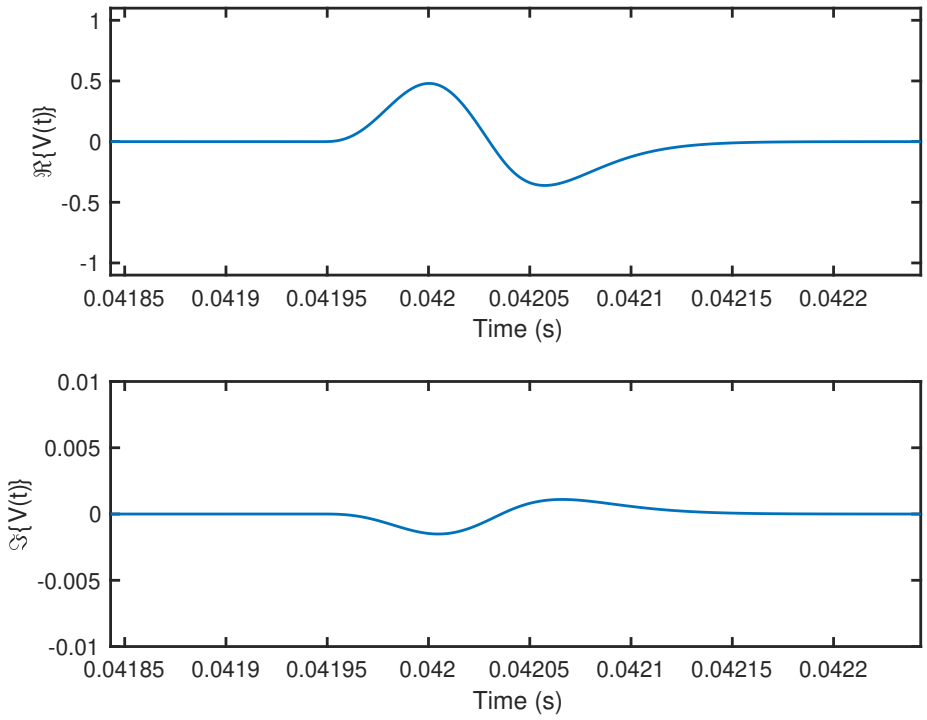

Figure A.4: Real and imaginary parts of the 10 kHz single-cycle sine wave voltage pulse propagated through the Debye model for loamy soil with 0% moisture content.

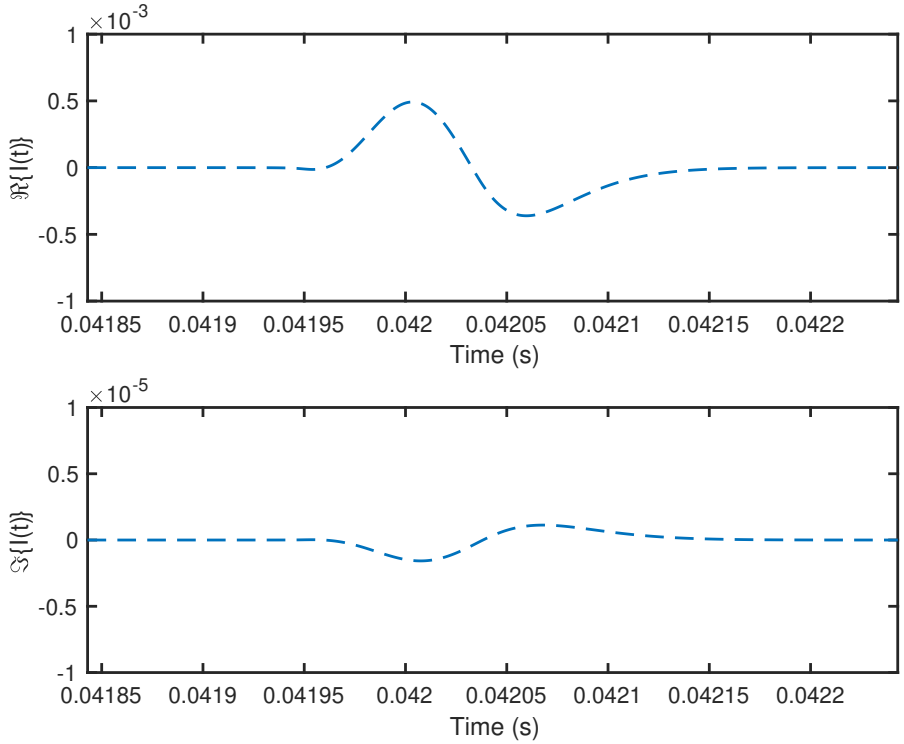

Figure A.5: Real and imaginary parts of the 10 kHz single-cycle sine wave current pulse propagated through the Debye model for loamy soil with 0% moisture content.

In order to better understand the behavior of the pulse propagation as it goes further into the media, the pulse power at increasing propagation distances was plotted for different frequencies in Fig. A.6. From the figure, it can be seen that the power decays across all chosen frequencies. This confirms the previous conjecture that the absorption there is more pulse absorption at the higher frequencies. Higher frequencies are impacted more significantly than lower frequencies, which is shown through the steeper slope of the $f_c = 100$ kHz and $f_c = 50$ kHz curves.

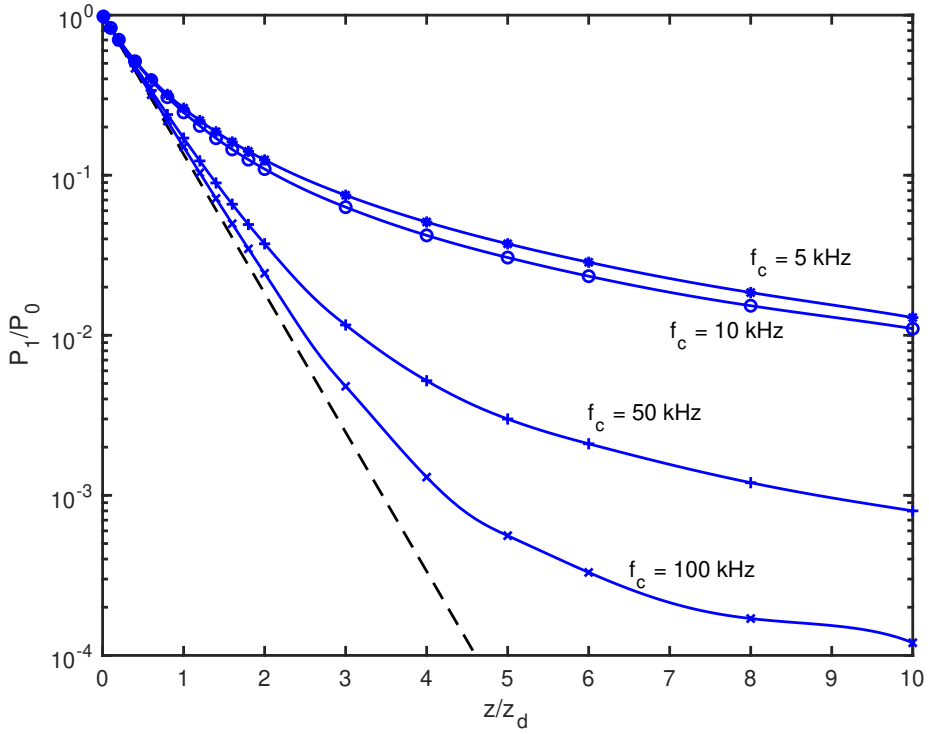

Figure A.6: Power of the single-cycle sine wave pulse at different frequencies for increasing propagation distances. The blue lines is the normalized pulse power at each frequency. The dashed black line is a reference for constant decay.

Appendix B

Voltage Pulse Propagation on a Dispersive Microstrip Line

This appendix is a conference paper [82], based on the work in Chapters 3, 4, and Appendix A, as it appears in 2021 United States National Committee of URSI National Radio Science Meeting (USNC-URSI NRSM).

Voltage Pulse Propagation on a Dispersive Microstrip Transmission Line

Katherine Aho and Kurt E. Oughstun
Department of Electrical & Biomedical Engineering
College of Engineering & Mathematical Sciences
University of Vermont
Burlington, Vermont 05401
e-mail kaho@uvm.edu

***Abstract*—The influence of Debye model material dispersion on transmission line dispersion using the Getsinger model is described with regard to voltage pulse propagation along the line as well as the inverse problem of the determination of the medium properties from the propagated pulse behavior.**

I. Introduction

The propagation of a voltage pulse along a dispersive attenuative transmission line is a problem of fundamental interest in electrical engineering [1] with application to both remote sensing for material identification, such as in time-domain reflectometry (TDR), and environmental vulnerability, such as that found in power lines [2]. The focus of the analysis presented in this paper is on the influence of the dielectric material properties of the substrate on the effective permittivity of a single microstrip transmission line as here described by the so called Getsinger model [3].

II. Transmission Line Analysis

With reference to the geometry and notation of Fig. 2 of Getsinger [3] and following the analysis given there, consider a single microstrip transmission line of width W on a nonmagnetic dielectric substrate of thickness b with relative permittivity ϵ_s. Above the microstrip line is air (vacuum) with $\epsilon = 1$. Microstrip propagation is considered here as a single longitudinal-section electric (LSE) mode approximated as that in a parallel plate transmission line with dielectric permittivity $\epsilon_s = \epsilon_s(\omega)$, width $2s$, and height b, connected to other parallel-plate transmission lines with unit relative permittivity, width a' and height b' with $a'/a = b'/b$.

Within this approximation, the effective relative dielectric permittivity of the microstrip line is found to be given by [3]

$$\epsilon_e(\omega) = \epsilon_s(\omega) - \frac{\epsilon_s(\omega) - \epsilon_{e0}}{1 + G(\omega^2/\omega_p^2)} \tag{1}$$

with $\epsilon_{e0} = \epsilon_e(0)$ the zero-frequency microstrip relative effective permittivity, where

$$\omega_p = \pi \frac{Z_0}{\mu_0 b} \tag{2}$$

with Z_0 the zero-frequency characteristic impedance of the microstrip, μ_0 the magnetic permeability of vacuum, and

$$G = \frac{\pi^2}{12} \frac{\left[(\epsilon_{e0} - 1) + (b'/b)^2(\epsilon_s - \epsilon_{e0}\right] (\epsilon_{e0} - 1)(\epsilon_s - \epsilon_{e0})}{\epsilon_{e0}(\epsilon_s - 1)^2}. \tag{3}$$

Notice that $G = G(\omega)$ depends upon the frequency through the substrate dispersion $\epsilon_s = \epsilon_s(\omega)$. However, the Getsinger model [3] does not capture the attenuation of the medium.

The Debye model is implemented in order to consider a substrate with attentive properties. At low frequencies, the material dispersion of the substrate is described by the Debye model [4], [5]

$$\epsilon_s(\omega) = \epsilon_\infty + \frac{\epsilon_{s0} - \epsilon_\infty}{1 - j\omega\tau}, \tag{4}$$

where $\epsilon_{s0} = \epsilon_s(0)$ is the static relative permittivity of the substrate material, $\epsilon_\infty \geq 1$ is the high-frequency ($\omega \gg 1/\tau$) limiting value of the relative permittivity, and where τ is the effective relaxation time of the material dispersion. Estimates of the model parameters ϵ_{s0}, ϵ_∞, and τ from observed pulse distortion should be sufficient to identify the substrate material (e.g. the percentage of water present in soil).

III. Numerical Results

Figure 1 illustrates the real and imaginary parts of the material dispersion of the substrate as described by the Debye model (4). These results illustrate the extent to which the relaxation time τ influences both the real and imaginary parts of the Debye model permittivity.

Of central interest here is the behavior of the effective relative dielectric permittivity of the microstrip line when a Debye model of the substrate dispersion is included. Veghte and Balanis [1] present several propagated pulse results, all using a constant value for the substrate dielectric ϵ_s. Of interest in future research is how material dispersion in the substrate will influence these results. Notice that without attenuation, the effective relative dielectric permittivity of the microstrip line increases towards the limit of the value of the substrate.

Figs. 2 and 3 present a comparison of the effective relative dielectric permittivity of the microstrip line with a constant substrate dielectric permittivity with $\epsilon_s = 10.2$ and with that for the Debye model substrate for several values of the

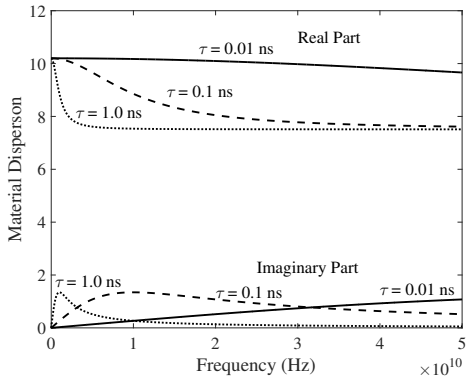

Fig. 1. Real and imaginary parts of the Debye model material dispersion of the substrate with $\epsilon_{s0} = 10.2$ and $\epsilon_\infty = 7.51$ for several values of the relaxation time τ: solid curve ($\tau = 0.01ns$), dashed curve ($\tau = 0.1ns$), dotted curve ($1.0ns$).

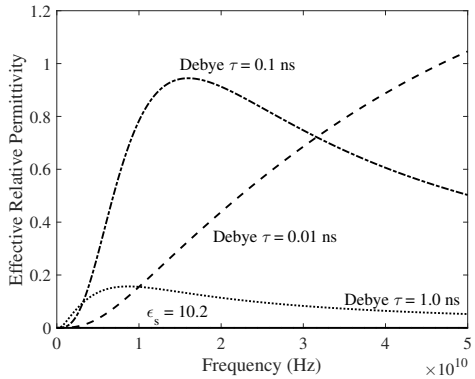

Fig. 3. Comparison of the imaginary part of the effective relative dielectric permittivity of the microstrip line between the constant valued substrate $\epsilon_s = 10.2$ and Debye model substrate $\epsilon_s(\omega)$ for several values of the relaxation time τ: dashed curve ($\tau = 0.01ns$), dot-dashed curve ($\tau = 0.1ns$), dotted curve ($1.0ns$)

relaxation time. The influence of attenuation in the Debye model substrate is prevalent. There is an overall decrease in the magnitude of the real part of the transmission line permittivity as the relaxation time τ increases. Fig. 3 also indicates the extent to which the imaginary part influences the attenuation in the transmission line, noting that there is zero attenuation in the Getsinger model for the case of a constant valued substrate permittivity.

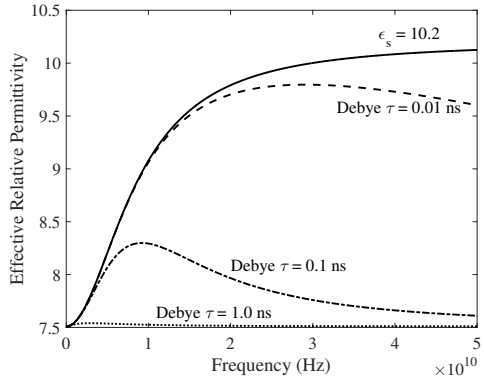

Fig. 2. Comparison of the real part of the effective relative dielectric permittivity of the microstrip line between the constant valued substrate $\epsilon_s = 10.2$ (upper solid curve) and the Debye model substrate $\epsilon_s(\omega)$ for several values of the relaxation time τ: dashed curve ($\tau = 0.01ns$), dot-dashed curve ($\tau = 0.1ns$), dotted curve ($1.0ns$).

IV. Future Work

Future work will investigate both the effects of substrate dispersion on voltage pulse propagation in a coupled microstrip transmission line as well as the inverse problem on estimating the Debye material properties of the substrate from measurements of the propagated pulse behavior along the transmission line.

ACKNOWLEDGEMENT

This work was supported by the National Science Foundation (NSF) IGERT Smart Grid and Complex Systems award (DGE1144388).

References

[1] R. L. Veghte and C. A. Balanis, "Dispersion of Transient Signals in Microstrip Transmission Lines," *IEEE Trans. Microwave Theory & Tech.*, vol. 34, pp. 1427–1436, December 1986.

[2] M. Parashar, J. S. Thorp, and C. E. Seyler, "Continuum Modeling of Electromechanical Dynamics in Large-Scale Power Systems," *IEEE Trans. Circuits & Systems*, vol. 51, pp. 1848–1858, September 2004.

[3] W. J. Getsinger, "Microstrip Dispersion Model," *IEEE Trans. Microwave Theory & Tech.*, vol. MTT-21, pp. 34–39, January 1973.

[4] P. Debye, *Polar Molecules*. New York, Dover, 1929.

[5] K. E. Oughstun, *Electromagnetic and Optical Pulse Propagation, Volume 1: Spectral Representations in Temporally Dispersive Media, 2nd ed.*. Springer, New York, 2019, pp. 217–221.